A NUMERICAL INVESTIGATION OF THE EFFECTS OF CROSSWINDS UPON THE AERODYNAMIC CHARACTERISTICS OF A HIGH-SPEED PASSENGER TRAIN AND ITS SLIPSTREAM

by

JUSTIN ANTHONY MORDEN

A thesis submitted to the University of Birmingham for the degree of DOCTOR OF PHILOSOPHY.

School of Engineering

University of Birmingham

September 2016

Abstract

The main work presented within this thesis is a numerical investigation of the effects of crosswind yaw angles upon the aerodynamic characteristics of a high-speed passenger train.

The applicability of Computational Fluid Dynamic (CFD) approaches to the simulation of external flow around a passenger train were investigated. Results showed the Delayed DES (DDES) approach produced the highest correlation to experimental results.

Ballast heights of 0m, 0.3m and 0.75m were simulated and compared to existing experimental results. Comparisons between cases found that a vortex from the train's underbody follows the ballast profile.

Crosswind simulations were conducted at yaw angles of 0^o, 5^o, 10^o and 15^o. The results obtained showed the formation of a large vortex upon the leeward side at yaw angles of 10^o and above, this caused a region of low pressure which increased the overturning forces acting upon the train. Generally, crosswinds increased pressures upon the windward side of the train and decreased them upon the leeward side. Slipstream velocities on the windward side were seen to decrease whilst leeward side velocities increased.

Results were compared to regulations currently in place for the operation and testing of trains. This enabled comments and suggestions to be made upon existing regulations.

Acknowledgements

I would firstly like to acknowledge my supervisors Dr Hassan Hemida and Prof Chris Baker for their exceptional guidance and shared knowledge over the duration of this PhD and also for their belief in me during the initial interview. I would also like to acknowledge the clear and honest guidance given by Dr Andrew Quinn and Prof John Bridgeman during reviews.

A special thank you goes out to my mother and the rest of my family who provided support and constantly reaffirmed how proud of me they were without ever pressuring me. Without their moral and at times financial support I am certain I would not have finished this thesis.

Additional thanks go out to the following individuals and groups:

- Ashley Hayden who made the office a bearable environment even on the days where I didn't want to be in and made every day a laugh.
- Dominic Flynn who provided advice and guidance when I needed it.
- Martin Gallagher for the provision of experimental data and for the discussions on any strange or unexpected results either of us encountered.
- Chiara Viezzi for making the house share feel like a second home after a day in the office.
- The members of the UoB Wayfarers hiking society for all the great adventures and laughs during my research period.
- Finally for all the friends and colleagues who I am unable to thank individually but either helped or made the PhD the great experience it was.

Contents

List of Figures

List of tables

List of symbols

C_d = Drag Coefficient

C_l = Lift Coefficient

C_{lee} = train reference length

C_m = Coefficient of roll Moment

C_p = Coefficient of Pressure

C_s = Side force Coefficient

d_g = Track gauge

d_w = nodal wall distance

E_{ij} = *component rate of deformation*

f_i = body force (N)

fn = over prediction

fp= under prediction

H = engine car height (m)

k = turbulent kinetic energy

l = train reference length

n_i = number of results

p = pressure (Pa)

p_c = pressure at cell

p_∞ = atmospheric pressure

Pe = Péclet number

t = time (s)

t' = convective time

q = Hit Rate

u_∞ = free stream velocity

u_f = frictional velocity

u_i = velocity component

$\chi_{i=}$ Cartesian coordinate

y = distance from wall

y^+ = Dimensionless wall distance

y_d = DDES wall distance

Greek symbols

∇ = gradient

Δ = maximum mesh spacing, each cell

$\tilde{\Delta}$ - filter cut off width

κ = Karman constant (0.41)

ϵ = turbulent dissipation

ω = specific dissipation

$\bar{\phi}(x,t)$ = *filtered portion*

$\phi(\xi,t')$ = *unfiltered portion*

μ_t = eddy viscosity (k-ε turbulence models)

μ = dynamic viscosity (N s/m^2)

ν_t = eddy viscosity (DDES)

ρ = fluid density (kg/m^3)

ν = kinematic viscosity

ν_t = eddy viscosity

$\tilde{\nu}$ = altered viscosity term

Abbreviations

CAD = Computer Aided Design

CEN = European Committee for Standardization

CFD = Computational Fluid Dynamics

CFL = Courant-Friedrichs-Lewy

CoP = Centre of Pressure

COT = Centre of Track

CPU = Central Processing Unit

CRH2 = China Railways High-speed 2 train

CWG = Cross Wind Generator

DDES = Delayed Detached Eddy Simulation

DES = Detached Eddy Simulation

DNS = Direct Numerical Simulation

EARSM = Explicit Algebraic Reynolds Stress Model

FB = Fractional Bias

FDC = Front Dead Centre

FVM = Finite Volume Method

GIS = Grid Induced Separation

HST = High-speed Train

ICG = Inter-Carriage Gap

ICE = Intercity-Express

IDDES = Improve Delayed Detached Eddy Simulation

KTX = Korea Train eXpress

LES = Large Eddy Simulation

MDF = Medium-density fibreboard

MPH = Miles Per Hour

MSD = Modelled Stress Depletion

NMT = New Measurement Train

OpenFOAM = Open source Field Operation And Manipulation

PISO = Pressure Implicit with Splitting of Operator

PIV = Particle Image Velocimetry

RANS = Reynolds Averaged Navier-Stokes

RNG = Re-Normalisation Group

RWDI = Rowan Williams Davies and Irwin

S-A = Spalart-Allmaras

SD = Standard Deviation

SIMPLE = Semi-Implicit Method for Pressure Linked Equations

SST = Shear Stress Transport

STBR = Single Track Ballasted Rail

TDC = Top Dead Centre

TFI = Turbulent Flow Instrumentation

TOR = Top of Rail

TRAIN = Transient Railway Aerodynamic Investigation

TSI = Technical Standard of Interoperability

TVD = Total Variation Diminishing

Chapter 1: Introduction

1.1. Research background

This thesis forms part of a larger project "The measurement of train aerodynamic phenomena in operational conditions" conducted at the University of Birmingham and funded by the UK Engineering and Physical Sciences Research Council, EPSRC. This project hypothesises that the prediction of aerodynamic characteristics such as velocities and pressures within the slipstream of passenger trains are highly conservative leading to large over predictions when using current methods. The aim of the project is to measure and compare model scale tests and CFD simulations to full scale aerodynamic measurements enabling conclusions to be drawn upon how accurate these approaches replicate real train aerodynamics. Within this research, the author follows the current methods specified for the train industry when conducting CFD simulations. Alternative case setups were investigated where the methods specified leave a gap or could have a potentially detrimental effect upon the accuracy of the results. This enabled the author to make suggestions on potential improvements to the currently recommended methods for industry.

The train chosen for this research was a Class 43 High-speed Train (HST), this train is also commonly referred to as the Intercity 125 in regards to its routes and maximum operational speed of 125 MPH. Constructed between 1975 and 1982 this diesel train still forms a major part of the UK rail passenger infrastructure. In comparison to newer train models that operate around the world the operational speed of the Class 43 is not very high, however the choice to use this train provided a number of distinct advantages for this project. These advantages include access to rail side locations on main lines where Class 43's operate regularly for the

purpose of slipstream measurements and the ability to add sensors to the Network Rails New Measurement Train (NMT) for the purpose of measuring surface pressures, yaw angle and train speed. It should be noted however that full scale data is not used within this research as all case setups replicate the model scale tests.

The slipstream of a moving object is created by a combination of air being accelerated as it is moved out of the way and through viscous and pressure effects drawing the air along with the moving object. The understanding of the slipstream created by high-speed passenger trains is important for two key reasons. Firstly and most importantly it is necessary to develop a thorough understanding of the slipstream around a certain train and trains in general for the safety of the public, trackside workers and trackside structures, all of which can be affected by the pressures and velocities within the slipstream of a train. The most common incidents regarding passengers are for prams to be drawn towards trains, incidents have also occurred where passengers upon the platform have been blown over by a passing train (Temple and Johnson 2008).

Within the United Kingdom mainland between 1972 and 2008 there were twenty four slipstream related incidents recorded of which none led to fatalities, the majority of these incidents are related to slipstream of freight trains RSSB (2007). As crosswinds can cause an increase in the velocities and pressures within the trains slipstream (Baker et al. 2007), these incidents become more likely to occur due to the constantly increasing maximum speeds of passenger trains. Furthermore high crosswinds have been responsible for the derailment of passenger trains, cases include the derailment of a Japanese six car express train in 2005 and a ten passenger car train in 2007 in China.

Secondly, it is important that the slipstream of a train is thoroughly understood to enable the design of a train that reduces the aerodynamic drag to a minimum. By reducing the aerodynamic drag of a train the required power and therefore fuel/energy requirements will reduce. A reduction in energy requirements is more important than ever with the current economic climate and environmental policies in place around the world.

For the slipstream of high-speed passenger trains numerous investigations have been conducted through the years using full scale (Kwon & Park, 2006. Quinn & Hayward, 2008. Baker et al. 2014), model scale (Brockie & Baker, 1990. Sterling et al, 2008. Soper et al, 2014.) and more recently CFD simulations (Muld et al, 2012. Hemida & baker, 2012. Flynn et al, 2014.). A study of current literature shows CFD simulations within train aerodynamics generally rely upon either high detail geometries analysed with numerical approaches dependent upon the modelling of turbulent flows (Johnson, 2006. Jönsson, 2010.), or highly simplified geometries often omitting all geometric details except the basic nose profile, which are analysed with numerical approaches that resolve a large portion of the flow (Wu, 2004. Hemida & Krajnović, 2009.).

In the interests of train design optimisation and safety it is important to continue to move towards the latest methods and keep research in this field to a level that is similar if not ahead of other comparable fields both within industry and research. To achieve this there is a need to use methods which resolve a large portion of the flows turbulence whilst maintaining a high level of geometric detail. Due to the continual advancement in computational power over recent years this is now a feasible proposition.

Additional analysis of current literature identified three key areas in need of additional research, the comparison of different numerical approaches, the effects of ground

configuration and the effects of low ($\leq 15^{o}$) yaw angle crosswinds. The first two were deemed to not be suitable for the basis of an entire thesis but were considered to be key setup variables for the third area of research. The analysis of different numerical methods has been conducted numerous times though for the rather unique geometry of a train it is normally limited to comparing one or two turbulence models. The setup of the ground configuration in this research refers to the effects of ballast heights. Current Technical Standard for Interoperability (TSI, 2008) and European standards (CEN, 2011) regulations state the slipstream measurements should be conducted upon a ballast height of 0.75m. It is important to check the effects of ballast height as if it does cause an effect upon the slipstream of a train there is the potential that its inclusion in the crosswind cases would over complicate and potentially change key flow features.

Research currently published upon the study of crosswinds and their effect upon the flow fields around trains tend to focus on highly simplified geometries experiencing larger yaw angles of 30^{o} or more. Yaw angles this large produce "worst" case scenarios for the train but do not show the more common real world conditions that a train would encounter. Within the UK the annual average wind velocity is only 2-5m/s (RenSMART, 2010), at the maximum speed (55m/s) of the Class 43 HST investigated within this research that results in a yaw angle range of 2.1^{o} to 5.2^{o} assuming the crosswind is perpendicular to the train.

The study of crosswinds at smaller yaw angles is important to ensure the safety of trackside personal and on board passengers. Currently the TSI regulations only state maximum limits for the slipstream velocity and pressures in conditions where the ambient flow velocity is below 2 m/s. Results presented within Baker et al. (2007) shows that crosswinds cause an increase in the velocities within a trains slipstream, it is therefore possible that these limits may be exceeded at even smaller crosswind yaw angles that would normally be safe.

1.2. Aim and Objectives

The aim of the research within this thesis:

To provide an improved understanding of the aerodynamic characteristics of a high-speed passenger train and its slipstream and as to how these characteristics are affected by crosswinds at yaw angles of up to 15^{o}.

In order to achieve this aim the following objectives were developed:

1. Investigate the effect of different steady state RANS turbulence models and DES based approaches cause upon surface pressure predictions upon a high-speed train at a scale of $1/25^{th}$ without cross wind, and to compare the results with wind tunnel data for the equivalent case to determine which approach best describe the flow around trains.

2. By comparing to experimental data, determine the accuracy of the DDES approach for predicting velocity and pressures profiles within the slipstream at varying ballast heights of 0m (flat ground), 0.3m and 0.75m.

3. Determine the effect of ballast shoulder height on the velocities and pressures around a high-speed passenger train using the DDES approach. Comparing the three ballast shoulder heights investigated of 0m (flat ground), 0.3m and 0.75m to each other.

4. By comparing to experimental data, determine the accuracy of the DDES approach at predicting surface pressures at yaw angles ranging from 5^{o} to 15^{o} when compared to experimental results.

5. Investigate the pressure, velocity and flow feature changes that occur within the slipstream of a high-speed passenger train as the yaw angle increases from 0^{o} to 15^{o} in 5^{o} increments.

6. Investigate the surface pressure and aerodynamic force changes that occur upon a high-speed passenger train as the yaw angle increases from 0^o to 15^o in 5^o increments.

7. Make comments and recommendations on TSI and CEN requirements.

1.3. Thesis structure

Chapter 3 contains the methodology of the various CFD simulations conducted within this research. Initially this chapter looks at the numerical fundamentals of the approaches used before looking at the adaptations made to the CAD geometries, the meshing technique, boundary conditions and finally discretisation schemes used.

Chapter 4 presents the evaluation of different CFD approaches and turbulence models via comparison to experimental results gathered in a wind tunnel using a $1/25^{th}$ scale two car train. Comparisons are made using aerodynamic forces and surface pressure coefficients measured from pressure tapping holes over the experimental models surface.

Chapter 5 presents an investigation into the effects of different ballast heights on the trains slipstream. Initially the three different ballast heights are validated against experimental data gathered from moving model tests using a $1/25^{th}$ scale train to determine if ballast height affects the obtainable accuracy of the CFD results. Pressure and velocity results obtained by CFD are then compared for each of the ballast heights to evaluate their effects upon a slipstream before visual comparisons are conducted to further investigate why these differences occur.

Chapter 6 presents the comparison of crosswind CFD results at three different yaw angles to results obtained from the wind tunnel and moving model experimental cases in order to

determine their accuracy. Results are compared for aerodynamic forces and surface pressures upon the first car at each yaw angle.

Chapter 7 presents the effects of varying crosswind yaw angles upon the slipstream of a high-speed passenger train. Initial comparisons are based upon visual analysis of 3D iso-surfaces for the pressures and velocities within the slipstream. Next visual comparisons are conducted using 2D planes through the domain contoured by velocity or pressure with streamlines showing the direction of the flow. Finally, numerical comparisons are conducted using pressures and velocities measured along lines through the domain on both the windward and leeward sides.

Chapter 8 presents the comparison of measured pressure and velocity values to those specified as limits within the TSI regulations.

Chapter 9 presents the effects of varying crosswind yaw angles on the surface pressures and aerodynamic forces experienced by the train. The effects of yaw angle upon the surface pressures are analysed using both measured pressure values and visual comparisons of pressure contours over the trains surface. Results are also compared to values obtained through the study of literature to further the analysis

In chapter 10 current regulations within the CEN and TSI are discussed. Comments are made upon requirements already in place and some recommendations are made for possible amendments. Additional suggestions are also made for additions the crosswind assessment section.

In chapter 11 final conclusions are drawn upon the effectiveness of this research in achieving the objectives and overall aim. Recommendations are also made for any potential future research based upon areas in need of further investigation.

1.4. Research outline

This thesis comprises of results obtained from numerical simulations conducted to investigate the effects of crosswinds upon the slipstream and surface pressures of a high-speed passenger train. Results obtained also look at the effects ballast height and numerical method cause to the accuracy of results in comparison to experimental results measured in parallel by a fellow researcher for their own thesis.

Results for the comparison of different CFD approaches to experimental data were published within the Journal of Fluids Engineering, Morden et al. (2014). An investigation into why differences exist within the previously mentioned publication is currently under review for the Journal of Computers and Fluids. Results from these two papers also formed a portion of a conference paper presented at the International Workshop for Train Aerodynamics at the University of Birmingham.

Results obtained from the ballast height investigations formed part of a conference publication at the Second International Conference on Railway Technology: Research, Development and Maintenance in Corsica. The First international conference in numerical and experimental aerodynamics of road vehicles and trains in France and the Institution of Mechanical Engineers in London.

Chapter 2. Literature review

2.1. Introduction

This chapter studies currently published literature on fields of research relevant to that of this thesis. Firstly in section 2.2 the slipstream around different regions of high-speed passenger trains with no crosswinds is summarised through the use of research conducted using full scale, model scale and/or CFD testing. Section 2.3 reviews how these slipstream features are affected by crosswinds, again relying upon multiple pieces of literature using full scale, model scale and/or CFD testing. Section 2.4.1, reviews the use of different forms of model scale testing within the literature. Though no model scale tests were conducted within this research, literature within this field was studied. This is due to model scale data that was gathered externally is used for the purpose of validation, therefore it is important to understand the strengths and limitations of different approaches. Finally section 2.4.2, reviews the use of CFD in detail to determine the obtainable accuracy and setup parameters used during the study of airflow around a train.

2.2. No crosswind

2.2.1. Train slipstream introduction

The slipstream is any region of fluid around a moving object where a substantial change in velocity, pressure and/or turbulence levels within the fluid is affected by the movement of that object. The slipstream of a train is produced by the same fluid principles as any other vehicle, however due to their considerable length and high-speeds the slipstream of a train is considerably larger. The slipstream of a train generally features highly turbulent flow at high

velocities with large and sudden pressure changes. The slipstream of a train is a broad term and covers the flow regions in front, around and within the wake of the train. The literature for these regions will be investigated independently of each other due to differences that exist within the flow characteristics at each location.

2.2.2. Nose region

Model scale results recorded for an Intercity-Express 2 (ICE 2) train geometry at 1/25th scale within Baker et al. (2001) showed that flow within the nose region can be considered as essentially inviscid, the authors made this statement based on the very high velocities and very low levels of turbulence within the flow around this region.

Measurement of flow variables around the nose region of a high-speed passenger train were conducted by multiple authors using full scale, model scale and CFD methods. Within the results there is a general trend for a rapid increase in pressure as the train nose approaches. This is followed by a sharp drop in pressure in line with the trains nose and for momentarily after it passes. Figure 1 taken from the research of Sanz-Andres & Santiago-Prowald (2002) shows this profile using results obtained from potential flow simulations.

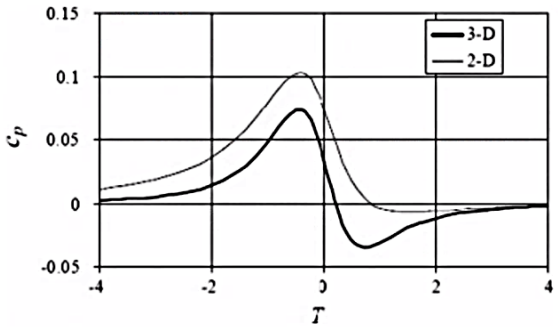

Figure 1: Potential flow calculations for Cp for the passing of a trains nose, T representing the time in relation to the passing of the nose. From Sanz-Andres & Santiago-Prowald (2002)

In Baker (2010), from the analysis of multiple data sources it was found that at full scale the displacement thickness of the initial boundary layer was considerably larger than that of model scale tests. It was concluded this was partly due to scaling effects.

Within the results of Soper (2014) it was found that the blunter shape of freight train promoted flow separation leading to run to run fluctuations around the nose region, This shows that the assumption that flow in the nose region is essentially inviscid is dependent upon the nose shape of the train and if flow separation occurs.

Research published by Baker et al. (2014) as part of a project called AeroTRAIN investigates the slipstreams and wakes around high-speed passenger trains using full scale measurements. Analysis of the recorded data showed that the shape of a trains nose had an effect upon the development of the boundary layer. Pointed noses were found to cause thinner boundary layers near the ground whilst more rounded noses were found to cause more rapid boundary layer growth. The nose velocity peak was found to mainly comprise of flow out from the trains centre with the longitudinal flow momentarily reversing.

2.2.3. Underbody region

The underbody region of the train is a critical area due to the highly turbulent flow created by the complex bogie and other underbody component geometries, such as battery and fuel tanks. Kwon & Park (2006) measured the airflow characteristic within the underbody during five passes of a Korea Train eXpress (KTX), the measurements were recorded using a sensor array mounted between the rails. Results of these measurements showed that the air velocity increased towards the Centre of Track (COT) location, this contradicts the finding of Quinn &

Hayward (2008) who recorded little across track variation of velocity, this implies flow within the region is sensitive to nose and under body shape.

Within the research of Johnson (2006) and Jönsson (2010) transient measurements of the underbody flow were recorded. These measurements showed lateral oscillations occurring at around 1.1Hz, These oscillations initially started small but were seen to grow in magnitude with distance along the train. Results showed these oscillations caused the shedding of vortices from the underbody location, separate to those caused by sudden changes in geometry.

Research conducted in Johnson (2006) investigated the effects of rotating wheels on underbody flows. It was found that they have little influence on the overall flow due to a radius of influence of approximately 0.1m at full scale. Within this small region of influence the inclusion of rotating wheels was found to increase the rate of longitudinal deceleration of the airflow and to encourage the flow to move in a downward direction. The work concludes from the initial simulations that the effect of rotating wheels was minimal enough to omit.

In the research conducted by Quinn & Hayward (2008) the underbody flow characteristics were recorded for class 373 Eurostar high-speed passenger trains for a total number of 42 passes, measurements were conducted using a sensor array placed between the track rails. The results showed high levels of sensitivity to the geometry of the train with clearly definable drops in the velocity coefficient as each of the bogies passed the sensor array. At the tail of the train the results showed peaks in the measured pressure and velocity coefficients. Figure 2 shows results obtained from experiments conducted by Quinn & Hayward (2008), these results show the large magnitude of the initial pressure pulse with smaller pulses after caused by both the Inter Carriage Gaps (ICG's) and bogies, T1 through to T5 represent different measurement locations between the rails.

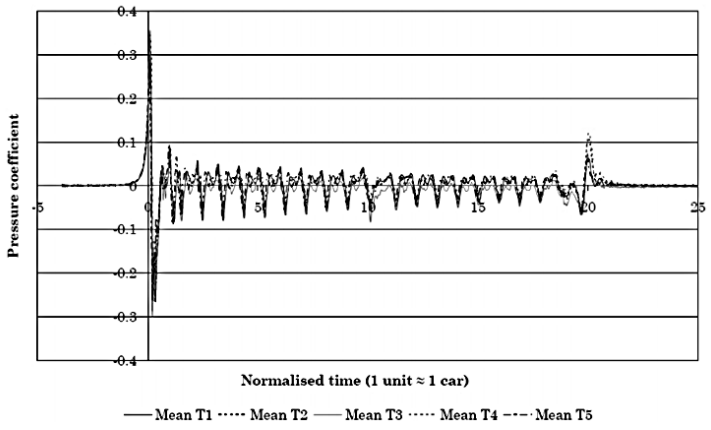

Figure 2: Pressure coefficients measurements taken from beneath a Eurostar train, From Quinn & Hayward (2008)

Quinn & Hayward (2008) also measured the cross rail velocity during each of the train passes, the results showed that the nose and tail regions produced high inward velocities towards the tracks centre whilst the general trend elsewhere was for an outward flow.

2.2.4. Train sides and roof

The skin friction values of 1/76thand 1/40th scale models of a HST train were compared to full scale results within the work of Brockie & Baker (1990), the results showed that the skin friction coefficient is highly dependent upon the scale used thereby suggesting the importance of using the largest scale possible. The authors' results showed that the boundary layer grew quicker and larger over the roof of the train than upon the sides, these results can be seen in Figure 3. The larger growth of the roof boundary layer was attributed to the boundary layer flow moving up the trains sides and converging upon the roof.

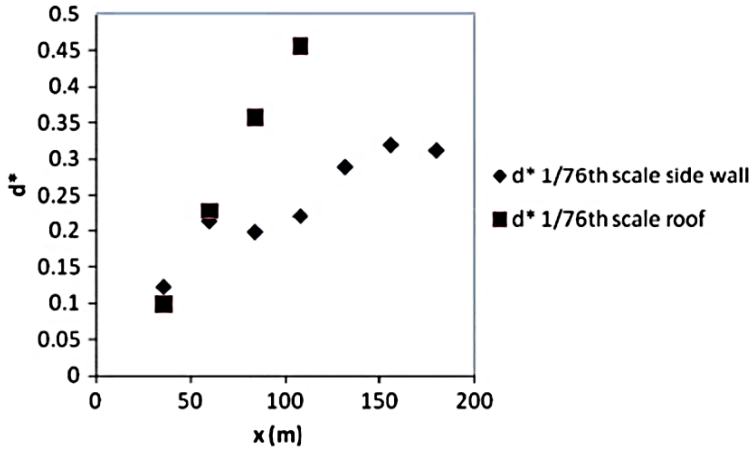

Figure 3: Boundary layer displacement thickness for side and roof of a 1/76th scale HST model. From Brockie & Baker (1990)

In Baker (2010) research from multiple sources are compiled to allow conclusions to be made upon the flow within these regions. Experimental data used was compiled from other authors who used a mixture of full scale and/or model scale testing methods. From the comparison of model scale results Baker was able to determine that the boundary layer continued to grow along the length of the train. Baker was also able to conclude that the boundary layer along the side of the train had an upward motion towards the roof of the train. Results recorded at full scale for a HST showed little boundary layer growth along the train side. The results that lead to this conclusion can be seen below in Figure 4.

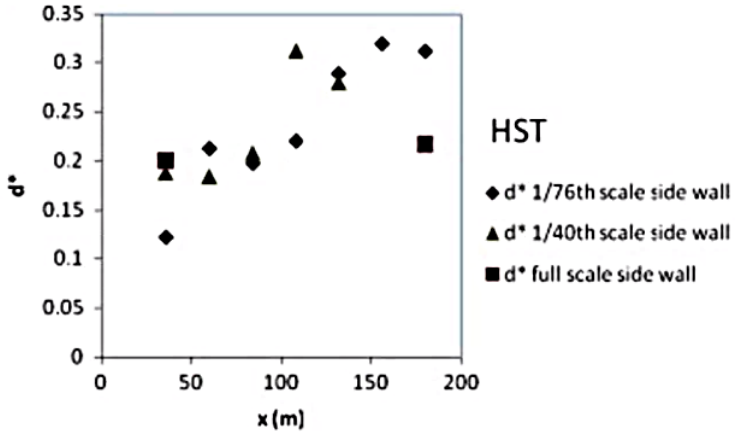

Figure 4: Variation in boundary layer displacement thickness along the length of a train from model and full scale testing. From Brockie & Baker (1990)

Large Eddy Simulation (LES) was used by Hemida & Baker (2012) to perform a simulation of the flow around a five car passenger ICE 2 train. The results showed that slipstream velocity in the region from the Top of Rail (TOR) to around one third car height was at a larger magnitude than in regions higher up, this was attributed to the exposed bogies and wheels creating more turbulence thereby energising the flow. The instantaneous results showed that flow was highly unsteady with large turbulent structures released regularly, primarily from the nose, ICG's and bogies. Results at multiple measurement distances from the COT showed the boundary layer to continue growing along the length of the train until the wake region, the rate of growth for the boundary layer can be seen to decrease after the second car in Figure 5.

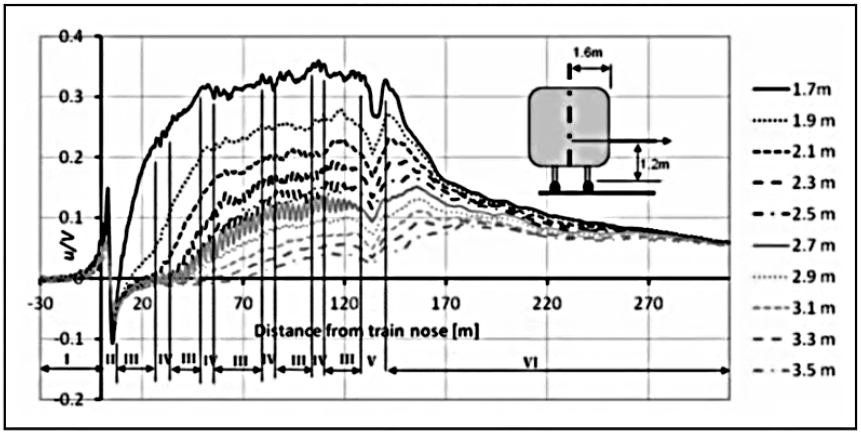

Figure 5: Trackside slipstream measurements of time averaged LES results and varying distances from COT and 1.2m above TOR, from Hemida & Baker (2012)

2.2.5. Inter Carriage Gap

The effects of the inter-carriage gap can be seen in the results of Wu (2004), the results show that during a crosswind situation a large vortex is formed at the leading top edge of the car directly following an ICG.

Jönsson (2007) conducted a RANS based simulation of two half car models with an ICG between them, periodic inlet and outlet boundary conditions were used to replicate the boundary layer build-up of a large train. Results showed that the modelling of the ICG is highly important as it feeds air into the low pressure underbody region of the train. It was also found that equipment which affects the flow over the train's roof such as pantographs can cause a large effect on the flows within the ICG and that any changes of the flow within the ICG can cause a large effect upon the flow regime within the underbody.

Research conducted using the LES approach in Hemida & Krajnović (2009) had a similar setup and geometry to that of Wu (2004) however the ICG was not modelled. Due to not

modelling the ICG there was no longer the formation of a vortex around the location where the ICG would be.

In the more recent research conducted by Hemida & Baker (2012) it was found that the ICG had only a small effect upon the time averaged velocity within the trains slipstream but caused a notable increase in the turbulence intensity of that region. Results also showed that the ICG was responsible for the production of regular instantaneous flow features which extended out into the trains wake.

2.2.6. Wake region

For the purpose of this literature review the very end part of the train tail is included within the wake region. Baker (2010) compared wake results of multiple passenger train geometries from both model and CFD tests. It was noted that within the wake region of both approaches two counter rotating vortices were formed which extend out far into the wake. These vortices are also visible within the more recent work of Hemida et al. (2012) and can be seen within Figure 6 where the flow direction is shown by vector arrows, these results were produced through the use of the more advanced LES method of CFD simulation.

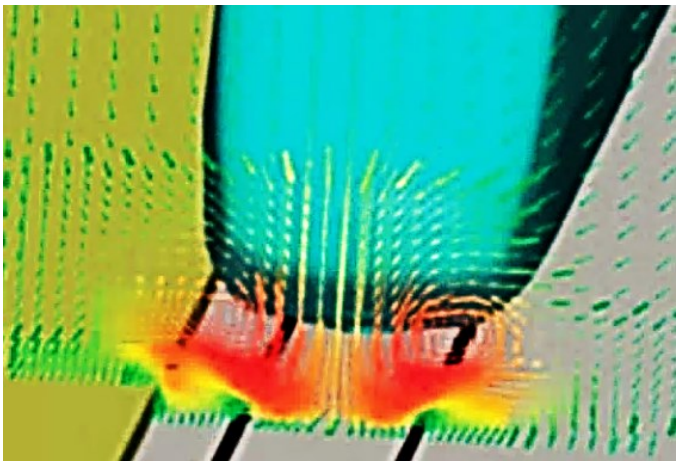

Figure 6: Vector arrows showing two vortices within the wake of an ICE2 train. From Hemida et al. (2012)

In Baker (2010) the work of Schulte-Wernin et al. (2003) and Sterling et al. (2008) are compared. It is found that in both cases oscillations occurred within the wake vortices. As distance from the train increases the velocity of the wake decreases and the spread from the COT position increases.

Research conducted by Muld et al. (2012) focused upon the wake of three different length 1/50th scale aero train models using the DES, the models were two, three and four cars long to study the effects of train length upon the wake characteristics. The mesh within the wake region was highly refined in comparison to the remainder of the train, the tail region featured 9.1 million cells of the 18.5 million cells for the larger train mesh.

The results show that upon the tail of the train the surface pressures are low around the side and roof edges due to flow acceleration, down near the tail point the pressure stays high. within the trains wake there were two counter rotating vortices producing a strong downward flow at the trains centre before travelling out at ground level before recirculating back up and towards the centre, this matches with the results shown in Hemida et al. (2012). The authors visualise the flow using streamlines, these streamlines showed that the vortices start at the roof before being drawn down into the wake. Iso-surfaces of the flow show that an oscillation occurs within the wake region, this oscillation is caused by the initial shedding of the vortices and causes the strength balance between the two vortices to fluctuate with time.

In the research of Huang et al. (2014) where results collected at full scale were compared to results obtained from CFD analysis of a 1/25th scale CRH2 model using the Improved Delayed Detached Eddy Simulation (IDDES) approach. The results obtained by the authors showed that just prior to the trains tail a large negative pressure spike occurs, this is quickly followed by a large positive pressure spike of around the same magnitude. The flow velocities

within this region also show a large spike, similar in magnitude to the nose peak, this velocity then decreases as distance into the wake increases. Overall, the authors found good levels of correlation between the IDDES and full scale results.

In Baker et al. (2014) the tail shape of the train was found to cause different flow features within the wake, pointed train tails accelerated the flow longitudinally from the train and into the wake whilst rounded noses caused an increase in the flow velocity towards the track centre line.

2.3. Effects of crosswinds upon passenger trains.

2.3.1. Crosswind literature introduction

The literature studied in this work so far only focused upon the slipstream of trains with little to no crosswinds, however this condition rarely exists outside of testing with passenger trains normally subjected to ambient winds from all angles at varying velocities whilst in service. The relative angle between crosswinds and a train is referred to as a yaw angle, this is the resultant angle created by the difference in velocities and angles of incidence. Crosswinds can potentially drastically change the slipstream around a train which in turn can cause consequences in regards to the safety of passengers and nearby personnel, Flynn (2015).

There have been multiple studies of the effects of crosswinds upon the slipstream of high-speed passenger trains using full scale, model scale and more recently CFD methods, however most research focused upon crosswind yaw angles of 30^{o} and above. Furthermore as previously mentioned research conducted using CFD tended to rely upon either highly simplified geometries and complex CFD approaches, which resolve a large portion of the flow or detailed geometries with CFD approaches based upon the modelling of flow.

2.3.2 Slipstream and wake regions

The effects of crosswinds upon the slipstream of a train were also investigated through the use of CFD in Khier et al. (2000). The authors used the k-epsilon (k-ε) turbulence model to study the yaw angles 20^o, 40^o, 60^o, 80^o and 90^o of a simplified two-car InterRegio train. The results showed that vortices were release from both the upper and lower edges of the trains leeward side, this agrees with the findings of Hemida & Krajnović (2009) and Wu (2004) that both used similar geometries.

In Baker (2010) full scale tests were analysed along with model and CFD results from multiple sources. It is stated within the conclusion that trains in crosswinds experience different flow shear and turbulence levels depend upon their speed. The crosswind results showed that within the wake of the train the longitudinal vortices that were produced caused an enhancement of the slipstream velocities upon the leeward side when compared to no crosswind cases.

In the research of Hemida & Krajnović (2009) the slipstream of a simplified ICE 2 train was investigated at a yaw angle of 30^o using LES. The train model was a one and a half car length model that featured a nose profile at the tail, this geometry can be seen in Figure 7. The geometry was similar to that of experimental work conducted within Wu (2004) but omitted the bogie and ICG geometries. Results showed that upon the leeward side of the train two dominant vortices format at the nose of the train. As can be seen in Figure 7 one vortex is formed and released from the lower leeward edge of the trains nose and fed by smaller vortices released from the lower leeward edge. The second vortex is formed from the trains nose and continues up and along the upper leeward edge remaining attached until the end of the leading car.

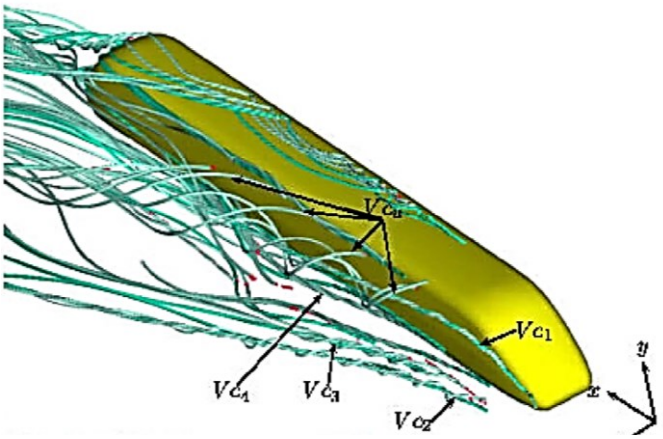

Figure 7: CFD model of a simplified ICE 2 train used in Hemida 7 Krajnović (2014) with streamlines showing vortices formed.

2.3.3 Surface pressures and aerodynamic forces

In the research of Diedrichs (2003) CFD was used to investigate the effects of crosswinds upon a three car ICE 2 train. The quadratic k-ε turbulence model was used to perform steady state full scale simulations. The results showed that the overturning moment for the lead car was over double that of the second car. The lead car also experienced higher lift loads though the difference between the two cars was considerably smaller. These differences resulted in overturning moments upon the leeward rail to be roughly double for the first car compared to the second.

The results presented within Diedrichs (2010) used both RANS and DDES to study the crosswind stability of two train models at two different yaw angles of 30^{o} and 41.5^{o}. The DDES results were only used for the higher yaw angle case but were found to be less diffusive leading to a lower pressure prediction around the nose. The results show that the first roof equipment produces a low pressure over the first half of the roof whilst the second roof equipment contributes a large portion to the lift force due to the low pressure it creates.

Research conducted by Tian Li et al. (2013) used CFD with the k-ε turbulence model to investigate the effects of crosswinds upon a simplified three car EMUV250 which did not features ICG's or bogies. The presented results found that the first car of the train showed the largest side and lift aerodynamic forces when subjected to a crosswind yaw angle of 8.08^{o}, matching the findings of Diedrichs (2003).

In the research of Hemida & Krajnović (2009) the results showed that the side force aerodynamic load was focused upon the nose of the train due to the low pressure drop within this region, this pressure drop was recorded to be twice the magnitude of the pressure drop recorded along the remainder of the body. Both side and lift forces were found to oscillate at a Strouhal number of 0.1 based on the averaged horizontal oscillation frequency of the wake vortices.

2.4. Testing methods introduction.

Literature within this section will focus upon the findings of various authors in regards to the different testing methodologies, obtainable accuracies and limitations of both model scale and CFD testing. Due to full scale results not being used within this research no further literature based upon it will be studied. Literature on model scale testing will cover both static model testing in wind tunnels and moving model methodologies. Literature for CFD simulations will cover the RANS, LES and DES methodologies applied to train and other comparable cases of external flow simulation.

2.4.1 Scale model testing literature.

Although not conducted for this research, results gathered from model scale tests are used for the purpose of validating the CFD approach at various stages throughout this thesis. Due to

this the understanding of the strengths and weaknesses of model scale tests is important in ensuring results are correctly interoperated. Model scale testing can be categorised into two forms of testing, stationary wind tunnel tests and moving model tests. The testing processes employed to obtain the external data used within this thesis are explained for each of the approaches within the methodology.

2.4.1.1. Wind tunnel testing.

Chiu & Squire (1992) conducted research using an idealised leading car model exposed to four different crosswind yaw angles of 60^{o}, 70^{o}, 80^{o} and 90^{o}, wind tunnel tests were conducted for the purpose of CFD validation. The wind tunnel model was mounted upon a raised ground board to reduce the build-up of a boundary layer within the wind tunnel. The authors found that the use of a ground board led to the production of only a small boundary layer that remained attached prior to the train. After the train the authors note that the boundary separation was found to inevitable though they report that this was useful for studying wake structures using an oil flow technique.

An analysis of wind tunnel research results from multiple sources was conducted by Baker and Humphreys (1996). It was concluded that in order to improve the accuracy of side and lift force coefficient values it would be necessary to include a moving ground and conduct the tests at a high Reynolds number. The authors state this necessity for high Reynolds numbers may be overcome by the use of highly turbulent flow. At higher yaw angles the authors concluded that the method of model mounting also become an important factor in obtaining correct lift coefficients.

Research conducted by Bocciolone et al. (2008) used a wind tunnel to analyse the flow around a 1/20 scale ETR 480 train, the results obtained showed that the aerodynamic coefficients were highly sensitive to the turbulence characteristics of the wind tunnel flow and that this sensitivity increased with increases in yaw angle. In research conducted by Schober et al. (2010) the authors concluded that the wind tunnel testing of a train upon an embankment that is experiencing crosswinds can lead to the calculation of unrealistic force coefficients. It was the recommendation of the authors that any such tests be conducted upon flat ground prior to the application of the Baker hypothesis first proposed in Baker (1985).

2.4.1.2. Moving model testing

Baker et al. (2001) studied the slipstream and wake of a $1/25^{th}$ scale model ICE train moving along a 150m track at speeds of 30 m/s. From the tests the authors were able to conclude that variations in model speed only have a small effect upon results obtained providing correct methods of normalisation are used.

The research conducted by Bocciolone et al. (2008) investigated the use of a moving model passing through the wind tunnel section. The authors notes the limitation of this approach due to the small amount of time the train passes through the test section but state the movement of the model had no significant effect upon the measured force coefficients.

Research conducted by Soper et al. (2016) studies the influence of ground geometries upon the slipstream of a train, this data was also used for validation of the ballast study that forms chapter 5 in this thesis. Testing was conducted using the same moving train facility as Baker et al. (2001). Testing was conducted upon both ICE 2 and Class 43 HST geometries, each of

which were four cars in length. Measurements were recorded using Cobra probes manufactured by Turbulent Flow Instrumentation (TFI) which can be seen in

Figure 8, these probes can measure to an accuracy of ±0.5 m/s, ±5 Pa and ±1% for velocities. The final uncertainty for results obtained using these measurements was deemed to be 2%. The authors note that a limitation of these probes is their ability to only record flow within a 45^{o} cone from the sensors face, any flow outside of this region is recorded as a zero. The authors note that this becomes an issue around the nose of the train where flow reversal is known to occur.

Figure 8: $1/25^{th}$ scale HST and cobra probes. From Soper et al. (2016)

2.4.2. Accuracy, limitations and setups of CFD approaches within literature.

CFD forms the basis of the work presented within this thesis, it is therefore critical that setup techniques and limitations of the approach are research within the literature. The literature for three different numerical methods are studied, these are RANS, DES and LES. As previous parts of this literature review already looked at how these methods handle train aerodynamics the following literature will also broaden out into similar fields where research was conducted using the different approaches. It is therefore the authors aim within this section of the

literature study to learn about case setups used, limitations of each approach and how they compare to each other.

2.4.2.1. The RANS approach.

Research was conducted comparing several RANS turbulence models including the S-A, Realisable k-ε and SST k-ω in Axerio-Cilies & laccarino (2012), in this work the authors compare flow predictions around a 60% scale formula one race car wheel using CFD and Particle Image Velocimetry (PIV) data at a Reynolds number of 5×10^5. Results showed the SST k-ω turbulence model was able to produce the closest match to experimental data when comparing vortex core locations and that the Realisable k-ε turbulence model proved to be the least accurate. When comparing aerodynamic forces obtained by CFD testing it was found that the SST k-ω and S-A turbulence models were at the two extremes of the predictions.

Research conducted by Tian Li et al. (2013) studied the airflow around a three car train at a yaw angle of 8.08^o, five different RANS turbulence models were used, the standard, Re-Normalisation Group (RNG) and realisable versions of the k-ε turbulence model and the standard and SST k-ω turbulence models. When comparing predicted lift and side forces from the CFD test to experimental data it was found all but the standard k-ω turbulence model predicted similar forces. The k-ω turbulence model constantly predicted larger forces on the head of the train and lower upon the tail though the variations were noted to be small by the authors.

2.4.2.2 DES and its variants.

Morton et al. (2003) used the DES approach to calculate aerodynamic forces over an f18 aircraft, the authors results showed that the DES approach provided an increased level of accuracy over the investigated RANS approach when calculating the aerodynamic forces for an F18 aircraft. Research conducted within Im & Zha (2011) found that both the DES and DDES approaches when studying a staling NACA0012 aerofoil were considerably more accurate at predicting aerodynamic forces than the unsteady RANS approach. Both of these agree with the findings of Hemida & Krajnovic (2009), Guilmineau et al. (2011) and Maddox et al. (2004) who all applied DES to ground vehicle aerodynamics with high levels of success when comparing aerodynamic forces, velocity profiles and pressures to experimental data.

Guilmineau et al. (2011) used DES to simulate the flow around a generic Ahmed car design. Three variants of the DES approach using the SST k-ω turbulence model were used along with an Explicit Algebraic Reynolds Stress Model (EARSM). Results for the DES approach showed good correlation with measured velocities and turbulent kinetic energy profiles, the EARSM approach also tested showed worse correlation. Simulations were conducted at a Reynolds number of 2.78×10^6 with an inlet velocity of 40 m/s. The blockage ratio for the domain was 4.3%. Three different mesh densities were tested with 7.5×10^6, 12.3×10^6 and 23.6×10^6 cells each, the wall normal height of these meshes was set so that the y+ range was 0.75 – 250. A 95% central differencing 5% upwind scheme was used to improve simulation stability.

DDES was used by Flynn et al. (2014) for the simulation of a class 66 freight trains slipstream traveling at 23 m/s at $1/25^{th}$ scale. The Reynolds number for the flow based upon train height and free stream velocity was approximately 3×10^5, meshes of 25×10^6 and 34×10^6 cells were used. The surface meshes of the train were 4×10^5 for the container cars and 6×10^5 for the

more complex geometry of the power car. The first layer height was set to 0.l mm which resulted in a y^+ range of 10 – 50 for the majority of the train's surface. The computational domain measured twenty eight train heights in front and behind the train and twenty two train heights wide and tall. A 95% central differencing scheme was employed with the remaining 5% set to upwind to improve simulation stability. The time step was set so that 99% of cells had a Courant–Friedrichs–Lewy (CFL) (Courant et al. 1928) number of ≤ 1. When compared to experimental data it was noted that good comparability was achieved at all but the region of flow reversal around the nose.

2.4.2.3. LES approach.

Axerio-Cilies & Laccarino (2012) also investigated the 60% scale wheel model using LES, the model differed slightly in that the brake duct and hub spokes were not modelled. The time steps of the simulation were set so that the maximum CFL number was 1.8. The LES results predicted flow structures that were not present within the results of the RANS approaches, the difference can be seen in the comparison of iso-surfaces conducted by the authors in Figure 9. One of the more important differences was the two counter rotating vortices coming off the wheel and into the wake were predicted to be much larger in the LES case. The comparison of aerodynamic forces for both drag and lift showed that the realizable k-ε and Reynolds stress models were able to predict aerodynamic forces close to that of the LES approach, the k-ω SST approach predicted notably higher values for both forces.

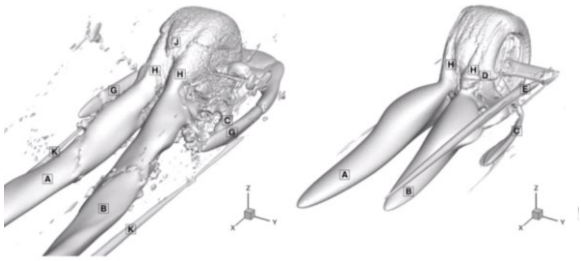

(a) LES isosurface of λ_2 for CI (b) R$k\varepsilon$ isosurface of λ_2 for CI

Figure 9: Comparison of flow structures using LES and RANS CFD approaches. From Axerio-Cilies & laccarino (2012)

In the work of Krajnović et al. (2012) where LES was used to simulate the flow around a simplified ICE2 train it is noted the LES approach was capable of accurately predicting dynamic changes in aerodynamic coefficients despite the considerably lower Reynolds number of 22,615 in comparison to what a real train would experience. Despite the very low Reynolds number used the authors still mention that the computational grid was required to be relatively fine. The wall normal distance (y^+) was below 1 for 99% of the cells of the fine mesh. A 98% second order central differencing was used with the remaining 2% using the upwind approach to improve stability, the time integration was set to second order. When compared to the experimental setup the LES approach proved to be capable of predicting the dynamic changes in the profile of the aerodynamic coefficients as the train moved through the crosswind section, but occasionally over predicted the changes in surface pressure.

Chapter 3. Methodology

3.1. Model scale.

Model scale data is used for the validation of the CFD work. This data was collected using both wind tunnel tests and a moving model rig. Model scale testing was conducted by external sources on behalf of the "The measurement of train aerodynamic phenomena in operational conditions" project that this thesis forms part of.

3.1.1. Wind tunnel

Wind tunnel results used within this research were collected from tests conducted by Rowan Williams and Davies Irwin Inc. (RWDI, 2012). A simplified two car model of the class 43 HST was used at a scale of $1/25^{th}$. This model was simplified by removing smaller geometric details from the trains under body and bogie regions. The power car was fitted with a total of 313 pressure taps, these taps were arranged in loops around all sides of the train, the locations of these loops are shown when necessary throughout this thesis.

The train model was mounted upon a single track ballast and rail (STBR) that conformed to the dimension requirements stated within the TSI, the dimensions of which can be seen in

Figure 10. The STBR was fixed to a splitter plate mounted 0.2m above the wind tunnel ground plane in order to reduce the boundary layer size approaching the train. Blockage ratio was not a concern due to the model being mounted within the open section of the wind tunnel. The splitter plate was rotated from 0 degree to 90 degree yaw angles in 5 degree increments.

The XYZ origin is set so that it is at the COT and TOR positions (black dot in Figure 10) and in line with the very start of the trains nose. The axis are set so that the X axis is parallel to the train with the positive direction running front to rear, the Y axis is horizontal and

perpendicular to the train with the positive axis moving to the trains left side and the Z axis is vertical and perpendicular to the train with the positive value in the upward direction.

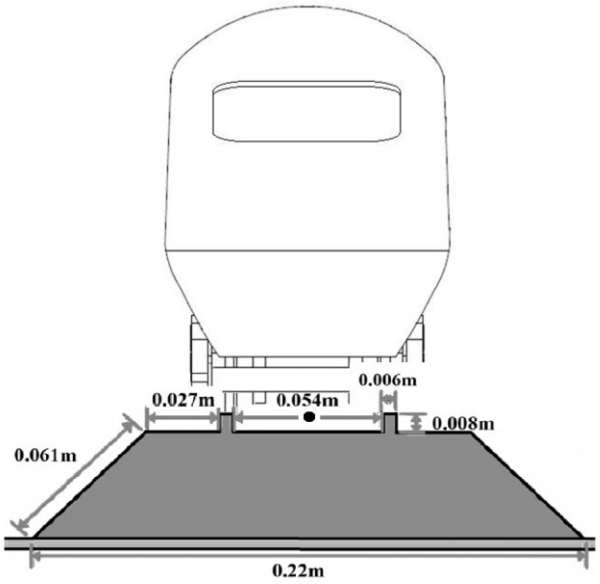

Figure 10: STBR measurements, black dot represents the COT and TOR position

The wind tunnel was set to a constant wind speed 13.2 m/s with a turbulence intensity of 10%. This resulted in a Reynolds number of approximately 1.2×10^5 based on the trains height of 0.165m. This Reynolds number is below the TSI specified minimum of 2.5×10^5 to ensure no Reynolds number scaling effects occur. Pressure tap measurements were recorded at each angle for 120 seconds to calculate time averages. Aerodynamic forces were calculated by RWDI for the train by extrapolating pressure tap measurements over the surface of the train.

3.1.2. TRAIN rig

Experimental testing was carried out by colleagues at the University of Birmingham using the University of Birmingham's Transient Railway Aerodynamics INvestigation (TRAIN) facility

located in Derby, UK. The facility comprises of a 150m double rail track upon which 1/25th scale train models are fired along. External aerodynamic measurements are taken within a 50m section using Cobra probes from Turbulent Flow Instrumentation. These probes are able to measure the three velocity components independently and also the local static pressure within the trains slipstream, all data was recorded using a custom built data logging system. The track contains a section where ballast heights can be adjusted and a section with a crosswind generator. The crosswind generator comprises of fans set to produce a wind speed of 11m/s perpendicular to the track. By varying the speed at which the train travels along the track it is possible to change the effective yaw angle.

The train carriages were fitted with eighteen pressure taps to monitor surface pressures that would allow comparisons to data collected during wind tunnel tests. To remove run to run fluctuations in the flow around the train twenty runs were completed for each case setup, an ensemble average was then calculated to provide results directly comparable with time averaged CFD results. An advantage of using the TRAIN facility is it allows the testing to be conducted with no deviation in results due to a ground plane boundary layer.

3.1.3. Model scale measurement limitations.

To conduct model scale tests both models had to be adjusted from the full scale train. For the wind tunnel tests this involved the removal of smaller details from the geometric details within the train's bogie and under body regions, a sensor umbilical cord was also fitted which passed between the STBR and the train's power car under body. To use the class 43 HST model at the TRAIN facility it had to be modified to incorporate the necessary firing

mechanism, larger gauge bogies, guides to fit on the wider tracks and a metal box chassis required so that the train could sustain the forces during the firing and braking procedures.

limitations also exist due to the use of Cobra probes for measurement at the TRAIN facility, The sensors used are unable to record reversed flow and therefore do not record the reversed flow that is known to occur just after the train's nose.

3.2. CFD Introduction

This chapter will provide an overview of the numerical fundamentals of CFD along with the finer numerical details and case setups used to achieve the objectives of this research.

With the constant improvements in computational power over the years what were once unfeasible simulation concepts are now becoming possible, this includes highly complex geometries with very fine resolution meshes, more complex numerical approaches which resolve a larger portion of the flow or indeed a combination of both. These advancements in methods though require validation as assumptions cannot be made on the basis of if it works for one situation it will work for all. For this reason the now somewhat outdated RANS approach is also included within the research due to its long history of use within this field.

The simulations presented within this research are conducted using the open source software package OpenFOAM by OpenCFD Ltd (OpenFOAM, 2014). The choice to use this software was made due to the lack of licensing requirements enabling the use of as many processors simultaneously as necessary. This would not be possible with commercial software packages available as they generally require an individual licenses per node (CPU) used. Along with CFD the OpenFOAM software package is also capable of solving thermal, acoustic, chemical

reactions and more. Due to the open source nature of the software the base code along with any basic variables such as boundary conditions can be adjusted if necessary to solve specific problems.

3.2.1. Numerical fundamentals.

The CFD aspect of the OpenFOAM software package is based upon the application of the Navier-Stokes equations to a discretised (mesh) computational domain, this approach is commonly known as Direct Numerical Simulation (DNS) (Orszag, 1970.). The direct solving of the Navier-Stokes by nature is highly computationally expensive and indeed for the cases investigated within this thesis impossible with the facilities available, for this reason approaches which rely upon either the time averaging of the Navier-Stokes or the modelling of the smaller turbulence length scales are most commonly used within research and industry for complex geometries.

3.2.1.1. Discretisation schemes

OpenFOAM like most other CFD software packages uses the Finite Volume Method (FVM) (Toro, 1999. And LeVeque, 2002.) to discretise partial differential equations for fluid dynamics and thermal problems. The application of FVM requires the use of control volumes and the computational problem to be discretised into smaller “control volumes”, this is often referred to as meshing with each smaller volume referred to as a cell within this work. This approach enables the requirement for conservation to be easily satisfied through the calculation of flow in and out of a control volume. Due to all simulations within this work

having a Mach number of below 1 the air can be treated as an incompressible fluid, therefore the incompressible continuity and momentum equations from the Navier-Stokes are:

$$\frac{\partial u_i}{\partial x_i} = 0$$

$$\frac{\partial u_i}{\partial t} + u_j \frac{\partial u_i}{\partial x_j} = f_i - \frac{1}{\rho}\frac{\partial p}{\partial x_i} + \nu \frac{\partial^2 u_i}{\partial x_j \partial x_j} \quad (1)$$

Where u_i represents the velocity components, x_i and x_j represent the Cartesian coordinates, f_i the body forces and ν is the kinematic viscosity.

To calculate the values within these partial differential equations finite difference schemes are used. One possible scheme is the central differencing scheme or linear as it is referred to within OpenFOAM, this scheme maintains the highest energy levels as values at the face between two nodes are interpolated using the values from the corresponding nodes. Central differencing is however highly unstable in complex geometries due to the high Péclet numbers that can occur if a mesh that is too coarse. The Péclet number is defined as:

$$Pe = \frac{Rate\ of\ advective\ transport}{Rate\ of\ diffusive\ transport} \quad (2)$$

To bypass the potential instabilities of using central differencing it is possible to use the highly stable upwind scheme, though this scheme features its own shortcomings. This approach is sensitive to the direction of flow and makes the simplified assumption that the value at the cell face is the same as the value at the centre of the upwind cell or cells depending on the order of the scheme used, thus potentially losing energy out of the flow.

The order of a scheme refers to how many mesh cells, other than the investigated cell are used when calculating its value. A 1st order scheme would only take into account the cell directly in contact with the investigated cell where as a 2nd order scheme would take into account this cells plus the next additional cell touching it and-so-forth as the orders increase. Figure 11 shows this upon a 1D mesh, where for 1st order the investigated cell (cell c) is dependent upon cell b, for 2nd order the investigated cell is dependent upon cells b and d.

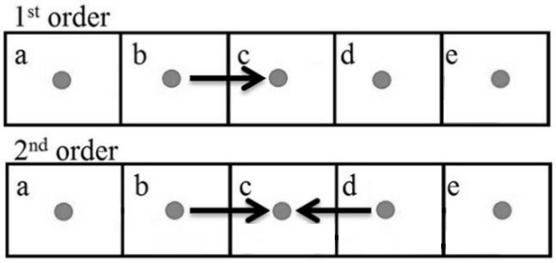

Figure 11: Diagram showing cell dependency for 1st and 2nd order schemes.

Due to the nature of RANS simulations being iterative, it is a necessary requirement to use the upwind approach. For the DES based simulations a third approach was used, this was the Total Variation Diminishing (TVD) scheme or limited linear as it is referred to in OpenFOAM. This scheme relies upon interpolation of points much like central differencing but due to the application of a limiter known as the Sweby (1984) limiter it does not suffer from instabilities at Péclet numbers larger than 2. This scheme was used within the work of Flynn (2015) where it was found to provide accurate results whilst maintain stable simulations. All DES and DDES simulations within this thesis used a Sweby limiter of 0.5 with a second order backward scheme for the temporal terms. This provides an increase in simulation stability as it prevents any rapid changes occur due to the reliance on the two previous time steps.

Work conducted using the RANS approach within this thesis used the Semi-Implicit Method for Pressure Linked Equations (SIMPLE) algorithm first proposed in Patankar and Spalding (1972). The SIMPLE algorithm decouples the pressure and velocity variables within the Navier-Stokes equations to enable their solution. The SIMPLE approach is designed for steady state cases and is therefore unsuitable for use with either the DES or DDES approaches, for these approaches the Pressure Implicit with Splitting of Operator (PISO) algorithm was used. This algorithm was first proposed in Issa (1986), the key difference between these two approaches that enables the PISO approach to be used for transient cases is it is non-iterative in its approach. Time steps within the transient simulations were set so that the maximum CFL at any point within the domain did not exceed 4, this value was chosen as it was the largest value which did not cause stability issues whilst still providing a speed up to solution times.

3.2.2. Reynolds averaged Navier-Stokes equations.

One method for bypassing the computational requirements associated with DNS is the use of the RANS approach. This approach relies upon the time averaging of the Navier-Stokes equations to calculate the average flow. In calculating the average flow the Reynolds stress tensors is produced, this represents the turbulent flows effect upon the averaged flows values. To model the Reynolds stress tensor, turbulence models are incorporated into the simulation. Five different turbulence models are used within the preliminary stages of this research, the Spalart-Allmaras, k-ε, Realizable k-ε, RNG k-ε and SST k-ω.

3.2.2.1. Spalart-Allmaras

OpenFOAM uses an adapted version of the Spalart and Allmaras (1994) turbulence model proposed in Ashford (1996). This is a one equation turbulence model specifically designed for situations where flow separation does not occur such as in aerospace. This turbulence model works by solving a transport equation for a modified turbulent viscosity value, as the model is only single equation it is the least computationally expensive turbulence model used in this research. The model relies upon a number of constants which were chosen through empirical experimentation to provide the most accurate results for the tested cases.

$$\left(\frac{\partial}{\partial t} + u.\nabla\right)\tilde{\nu} = \frac{1}{\sigma}\nabla\cdot((\nu + (1+C_{b2})\tilde{\nu})\nabla\tilde{\nu}) - \frac{C_{b2}}{\sigma}\tilde{\nu}\Delta\tilde{\nu} + C_{b1}(1-f_{t2})\hat{S}\tilde{\nu} - \left(C_{w1}f_w - \frac{C_{b1}}{\kappa^2}f_{t2}\right)\left(\frac{\tilde{\nu}}{d}\right)^2 + f_{t1}\Delta U^2 \quad (3)$$

The coefficients for this turbulence model are:

C_{b1}= 0.1355, C_{b2} = 0.622, C_{w2} = 0.3, C_{w3} = 2, C_{v1} = 7.1, C_{v2} = 5, κ=0.41 σ=0.66666

To account for the large cell sizes (y^+ value) used near the walls in all meshes produced for this research, the Spalding wall function first proposed in Launder and Spalding (1974) was applied to all cases using the Spalart-Allmaras turbulence model.

3.2.2.2. k-ε

The k-ε turbulence model is arguably the most commonly used and studied turbulence model. The standard model was first proposed in Jones and Launder (1972). The turbulence model is a two equation model with k representing the turbulent kinetic energy (equation 4) and ε

representing the turbulent dissipation (equation 5). Due to being a two model approach it is more computationally expensive than the S-A approach.

Turbulent kinetic energy (k):

$$\frac{\partial}{\partial t}(\rho\kappa) + \frac{\partial}{\partial \chi_i}(\rho\kappa u_i) = \frac{\partial}{\partial \chi_j}\left[\left(\mu + \frac{\mu_t}{\sigma_\kappa}\right)\frac{\partial k}{\partial \chi_j}\right] + P_\kappa - \rho\epsilon \quad (4)$$

Turbulent dissipation (ε):

$$\frac{\partial}{\partial t}(\rho\epsilon) + \frac{\partial}{\partial \chi_i}(\rho\epsilon u_i) = \frac{\partial}{\partial \chi_j}\left[\left(\mu + \frac{\mu_t}{\sigma_\epsilon}\right)\frac{\partial \epsilon}{\partial \chi_j}\right] + C_{1\epsilon}\frac{\epsilon}{\kappa}(P_k + C_{3\epsilon}P_b) - C_{2\epsilon}\rho\frac{\epsilon^2}{k} + S_\epsilon \quad (5)$$

Where:

u_i represents the velocity component for the corresponding direction

E_{ij} represents the component of the rate of deformation

μ_t represents the eddy viscosity and is calculated with the equation:

$$\mu_t = \rho C_\mu \frac{\kappa^2}{\epsilon} \quad (6)$$

P_κ represents the production of k and is calculated with the equation:

$$P_k = -\overline{\rho u_i' u_j'}\frac{\partial u_j}{\partial \chi_i} \quad (7)$$

P_b represents the effect of buoyancy and is calculated with the equation:

$$P_b = \beta g_i \frac{\mu_t}{Pr_i}\frac{\partial T}{\partial \chi_i} \quad (8)$$

Constants used within this turbulence model are:

$C_\mu = 0.09$ $\sigma_\kappa = 1$ $\sigma_\epsilon = 1.3$ $C_{1\epsilon} = 1.44$ $C_{2\epsilon} = 1.92$

All cases within this research using any of the ε based turbulence models rely upon the ε wall function to account for high y^+ values, the ε wall function was design for high Reynolds number flows and works by using measured near wall ε values as constraints within the ε equation.

3.2.2.3. RNG k-ε

The Re-Normalisation Group or RNG k-ε turbulence model was first proposed as an adaption to the standard k-ε turbulence model in Yakhot et al. (1992), the purpose of this model was to better account for effects created by smaller scales of motion. The turbulent kinetic energy (equation 9) remains the same as in the standard k-ε turbulence model but adjustments are made to the turbulent dissipation energy equation (equation 10).

Turbulent kinetic energy:

$$\frac{\partial}{\partial t}(\rho\kappa) + \frac{\partial}{\partial \chi_i}(\rho\kappa u_i) = \frac{\partial}{\partial \chi_j}\left[\left(\mu + \frac{\mu_t}{\sigma_\kappa}\right)\frac{\partial k}{\partial \chi_j}\right] + P_\kappa - \rho\epsilon \quad (9)$$

Turbulent dissipation:

$$\frac{\partial}{\partial t}(\rho\epsilon) + \frac{\partial}{\partial \chi_i}(\rho\epsilon u_i) = \frac{\partial}{\partial \chi_j}\left[\left(\mu + \frac{\mu_t}{\sigma_\epsilon}\right)\frac{\partial \epsilon}{\partial \chi_j}\right] + C_{1\epsilon}\frac{\epsilon}{\kappa}P_k - C_{2\epsilon}\rho\frac{\epsilon^2}{\kappa} \quad (10)$$

Where:

$$C_{2\epsilon}^{*} = C_{2\epsilon} + \frac{C_{\mu}\eta^{3}(1 - \eta/\eta_{0}}{1 + \beta\eta^{3}} \quad (11)$$

$$\eta = Sk/\epsilon \quad (12)$$

$$S = (2S_{ij}S_{ij})^{1/2} \quad (13)$$

Constants for the RNG k-ε turbulence model are:

$C_{\mu} = 0.0845$ $\sigma_{\kappa} = 0.71942$ $\sigma_{\epsilon} = 0.71942$ $C_{1\epsilon} = 1.42$

$C_{2\epsilon} = 1.68$ $\eta_{0} = 4.38$ $\beta = 0.012$

3.2.2.4. Realizable k-ε

The Realizable k-ε turbulence model is an alteration of the standard k-ε turbulence model first proposed in Shih et al. (1995). In comparison to the standard k-ε model this model relies upon different equations for both the turbulent kinetic energy (equation 14) and for the dissipation rate (equation 15). This version of the k-ε model also allows for variation in the Cμ variable instead of it remaining a constant, the equation responsible for this is shown in equation 20. Due to these adjustments this model satisfies the required inequality between the Reynolds stress tensor components thus allowing the model to be described as realizable.

Turbulent kinetic energy:

$$\frac{\partial}{\partial t}(\rho k) + \frac{\partial}{\partial \chi_{j}}\left(\rho\kappa u_{j}\right) = \frac{\partial}{\partial \chi_{j}}\left[\left(\mu + \frac{\mu_{t}}{\sigma_{\kappa}}\right)\frac{\partial k}{\partial x_{j}}\right] + P_{\kappa} + P_{b} - \rho\epsilon - Y_{M} + S_{\kappa} \quad (14)$$

Turbulent dissipation:

$$\frac{\partial}{\partial t}(\rho\epsilon) + \frac{\partial}{\partial \chi_j}\left(\rho\epsilon u_j\right) = \frac{\partial}{\partial \chi_j}\left[\left(\mu + \frac{\mu_t}{\sigma_\epsilon}\right)\frac{\partial \epsilon}{\partial \chi_j}\right] + \rho C_1 S\epsilon - \rho C_2 \frac{\epsilon^2}{\kappa + \sqrt{\nu\epsilon}} \quad 15$$

$$+C_{1\epsilon}\frac{\epsilon}{\kappa}\, C_{3\epsilon} P_b + S_\epsilon$$

Where

$$C_1 = \max\left[0.43, \frac{\eta}{\eta + 5}\right] \quad 16$$

$$\eta = S\frac{k}{\epsilon} \quad 17$$

$$S_k = \sqrt{2S_{ij}S_{ij}} \quad 18$$

$$Y_M = 2_{\rho\varepsilon} M_t^2 \quad 19$$

$$C_\mu = \frac{1}{A_o + A_s U^{(*)}\frac{\kappa}{\epsilon}} \quad 20$$

Constants for this turbulence model are slightly adjusted to that of the standard k-ε model, the constants are:

$\sigma_k = 1$ $\sigma_\epsilon = 1.2$ $C_{1\epsilon} = 1.44$ $C_{2\epsilon} = 1.9$

3.2.2.5. SST k-ω

The SST k-ω turbulence model was first proposed in Menter (1993) and is an alteration of the standard k-ω turbulence model proposed in Wilcox (1988), the version used within the OpenFOAM software package is a modified version proposed in Menter and Esch (2001). The use of a revised version is so that all coefficients can be blended (due to the application of a blended divergence scheme) in a consistent manner. The SST k-ω model relies upon the k-ω

turbulence model in the near wall regions and the k-ε approach in the free stream regions, thereby removing key limitations of each individual approach. For the k-ω part of the equation the turbulent kinetic energy and the specific dissipation equations are listed below as equation 21 and equation 22 respectively.

Turbulent kinetic energy:

$$\frac{\partial(\rho\kappa)}{\partial t}+\frac{\partial(\rho U_j\kappa)}{\partial x_j}=\tilde{P}_k-\beta^*\rho k\omega+\frac{\partial}{\partial x_j}\left[\Gamma_k\frac{\partial\kappa}{\partial\chi_j}\right] \quad 21$$

Specific dissipation:

$$\frac{\partial(\rho\omega)}{\partial t}+\frac{\partial\left(\rho U_j\omega\right)}{\partial\chi_j}=\frac{\gamma}{v_t}P_k-\beta\rho\omega^2+\frac{\partial}{\partial\chi_j}\left[\Gamma_\omega\frac{\partial\omega}{\partial\chi_j}\right] \quad 22$$

$$+(1-F_1)\,2\rho\sigma_{\omega2}\,\frac{1}{\omega}\frac{\partial k}{\partial\chi_j}\frac{\partial\omega}{\partial\chi_j}$$

Where

$$\Gamma_k=\mu+\frac{\mu_t}{\mu_k} \quad 23$$

$$\Gamma_\omega=\mu+\frac{\mu_t}{\sigma_\omega} \quad 24$$

$$P_k=+\tau_{ij}\frac{\partial \mathrm{U}_i}{\partial \mathrm{x}_j} \quad 25$$

$$\tilde{P}_k = \min(P_k; c_1\epsilon) \quad 26$$

The coefficients for this turbulence model are:

$\sigma_{k1} = 0.85034, \quad \sigma_{k2} = 1, \quad \sigma_{\omega1} = 0.5, \quad \sigma_{\omega2} = 0.85616, \quad \kappa = 0.41, \quad \gamma_1 = 0.5532,$

$\gamma_2 = 0.4403, \quad \beta_1 = 0.075, \quad \beta_2 = 0.0828, \quad \beta^* = 0.09, \quad c_1 = 10$

The ω wall function was applied to all cases dependent upon the SST k-ω turbulence model, this wall function was used to account for high y^+ values of the meshes used. The version of the ω wall function used within this research was proposed in Menter and Esch (2001) with the equation:

$$\omega = \sqrt{{\omega_{vis}}^2 + {\omega_{log}}^2} \quad 27$$

Where ω_{vis} is ω in the viscos region and ω_{log} is ω in the logarithmic region.

3.2.3. LES equations

Large eddy simulation was first proposed in Smagorinsky (1963) as a way of improving upon the accuracy of simulations in comparison to the RANS approach without the computational requirements of DNS. The LES approach works by resolving the larger turbulent flow scales whilst the effects of smaller scales are accounted for via a sub-grid scale model. This approach relies upon the assumption that the larger scales of turbulence are the key flow features that are defined by the investigated geometry and that the smaller scales are for the most part generic between cases, this theory was first proposed in Kolmogorov (1941).

Although LES is not directly used within this research it is used as part of the DES based approach detailed in section 3.2.4.

The key principle of LES is the filtering Equation (28), this equation is responsible for the decomposition of flow variables into components that will either be resolved or that will be modelled using the sub-grid scale model.

The LES filter equation is:

$$\bar{\phi}(x,t) = \frac{1}{\Delta}\int_{-\infty}^{\infty}\int_{-\infty}^{\infty} G\left(\frac{x-\xi}{\Delta}, t-t'\right)\phi(\xi,t')dt'd^3\xi \qquad 28$$

Where G is the filter, $\bar{\phi}(x,t)$ is the filtered portion, $\phi(\xi,t')$ is the unfiltered portion and Δ is the size at which the filter no longer applies.

3.2.4. DES and DDES

The DES approach was first proposed in Spalart et al. (1997). The DES approach upon the use of both the LES and RANS approaches previously mentioned, within regions where the flow is detached from the models surface the LES approach is implemented, whilst in regions where the flow is attached to surfaces the RANS approach is implemented with a turbulence model. The standard turbulence model to be used with the DES approach is the S-A model previously described in section 3.2.2.1. The aim of DES is to provide similar levels of accuracy for large flow features as to what could be achieved with LES whilst having

significantly less computational expense. The switching between LES and RANS is controlled by an equation called the DES limiter (Equation 29)

$$l_{DES} = \min\ (d_w, C_{DES}\Delta) \qquad 29$$

Where d_w is the nodal wall distance, C_{DES} is a constant of 0.65 and Δ represents the maximum mesh-spacing for each cell. The limiter l_{DES} is a modification of the distance function used within the S-A turbulence model.

The DDES approach was first proposed in Spalart et al. (2006). This variation was developed in order to remove two phenomena noted to occur with the standard DES approach. These two phenomena are Modelled Stress Depletion (MSD) and Grid Induced Separation (GIS). MSD was first named in Spalart et al. (2006) however the effect of it and GIS were first noted in Menter and Kuntz (2002).

MSD occurs when the mesh contains cells that are thinner than the boundary layer thickness but large in other directions, the DES limiter will not be hit so a LES approach will be used despite the meshes inability to provide an accurate simulation due to the large cell size. In this situation there will be a loss of flow detail which will result in a reduction of both the eddy viscosity and the Reynolds stresses. The occurrence of MSD can lead to the development of GIS, this is when flow separates from a face earlier than it should or when flow separate's from a region where it would not normally separate due the DES limiter forcing a switch to the LES approach in a region where the mesh is not suitably refined.

The DDES approach solves these issues that occur by continuing to use a RANS approach when it detects a boundary layer even if the mesh spacing would normally trigger the limiter

to switch to an LES approach. This is achieved by an adaption of the standard DES length scale equation to include the value of the eddy-viscosity.

$$l_{DDES} = y_d - f_d \max(0, d_w - C_{DES}\Delta) \quad 30$$

The f_d function is the new switching component and is defined as:

$$fd = 1 - \tanh((8r_d)^3) \quad 31$$

$$r_d = \frac{\nu_t + \nu}{\sqrt{U_{ij}U_{ij}\kappa^2 y_d^2}} \quad 32$$

Where y_d is the distance from the wall and ν_t is the eddy viscosity

3.3. CAD geometry adaptations

In order to produce suitable meshes for use within the presented research it was necessary for adaptations to be made to the CAD geometry of the train. Adaptations included the removal of smaller details within the bogie region, simplification of the geometry around the trains front windscreen edge and the addition of material between the wheels and the track to remove the pinch zone angle. Dimensions of the power car and passenger car can be seen in Figure 12 and Figure 13 respectively.

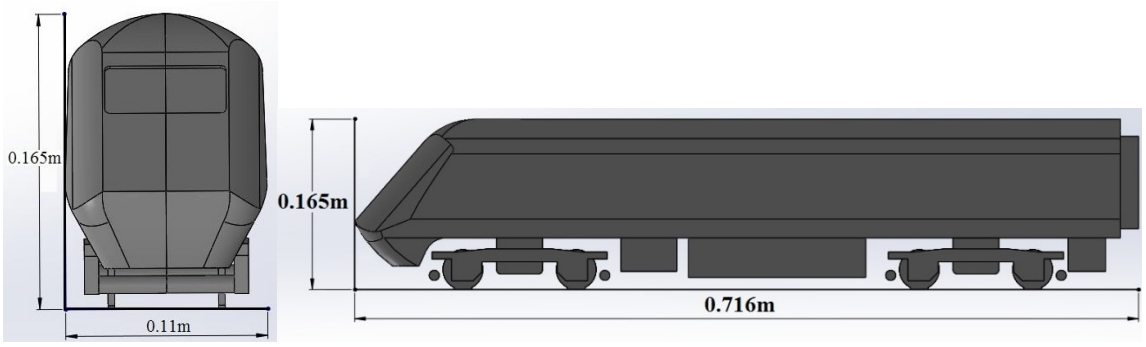

Figure 12: Dimensions of power car from the front and side.

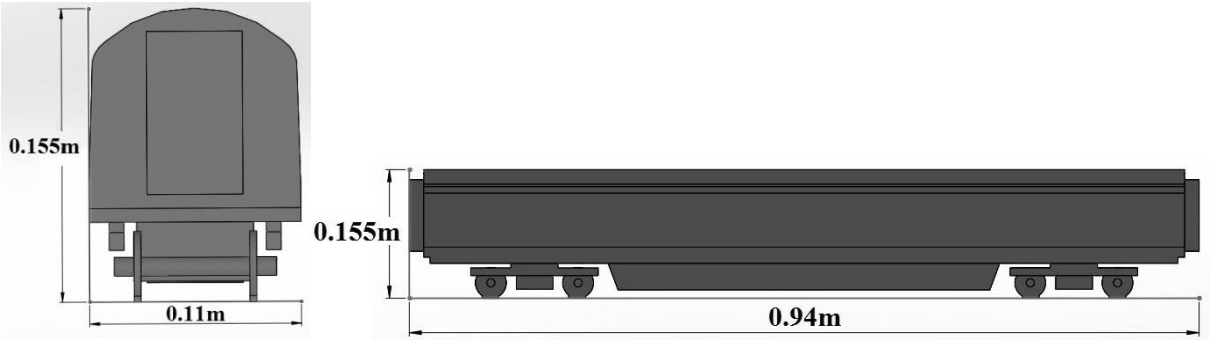

Figure 13: Dimensions of passenger car from the front and side.

For the TRAIN rig model the exact geometry of the firing mechanism was not included due to its complex shape and its location being in close proximity to the ground, instead the geometry was replace with a cube which replicates the majority of the firing mechanisms shape and provides a similar blockage to the trains undercarriage. The TRAIN rig model also incorporates an aluminium box section chassis, this box was added to the geometry used to replicate the TRAIN rig tests. The final adjustment made was the inclusion of the replacement bogies that are part of the firing mechanism, these are required as the TRAIN facility uses a slightly wider track gauge with wider rails to launch the models along. These additional bogies and frame are highlighted in Figure 14.

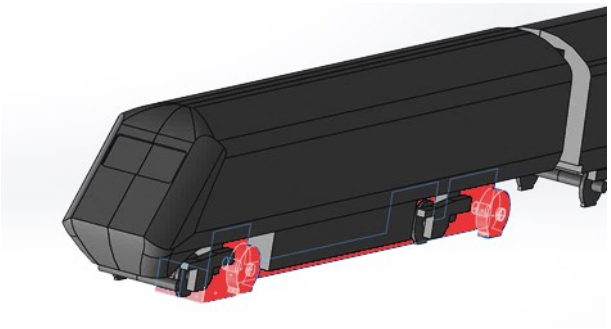

Figure 14: Leading (power) car with adjustments highlighted in red.

3.4. Meshing methodology

Three sets of meshes were required to complete the research, a set of meshes to replicate the RWDI wind tunnel tests, a set to replicate the ballast height tests and finally a set for the crosswind tests. Mesh dependency studies were conducted for each mesh set to ensure that there was no mesh dependency within the results whilst still maintaining an optimum mesh cell count. Mesh dependency was determined by finding little to no variation in results when comparing aerodynamic forces and surface pressures at multiple locations.

Each mesh was produced using the snappyHexMesh application within the OpenFOAM package. This approach produces an initial coarse Cartesian mesh before refining down specified regions. Next the investigated geometry is "cut" from the Cartesian mesh. Further refinement is then carried out upon the surface of the removed geometry if necessary. The final step is prism layers are added to any specified regions, these prism layers enable a finer mesh height near walls to allow for more accurate boundary layer modelling. The number of cells each mesh contained was controlled by changing the maximum cell size within each refinement region, the number of refinement regions and the number of prism layers.

Mesh statistics were check upon the completion of each meshing process to ensure the mesh was suitable for use. The CEN requirements state that the wall layer cells for the RANS approaches should feature a y^+ of between 30 to 150 or below 1 depending upon the use of wall functions.

3.4.1. Wind tunnel meshes

For the wind tunnel geometry a total of four meshes were initially tested as part of the mesh dependency study. The meshes comprised of 18, 24, 34 and 52 million cells and are referred to as coarse, medium, fine and very fine respectively. The domain extents remained constant for each mesh with a blockage ratio of 6% which is below the CEN recommendation of 10%. The dimensions of the domain can be seen in Figure 15.

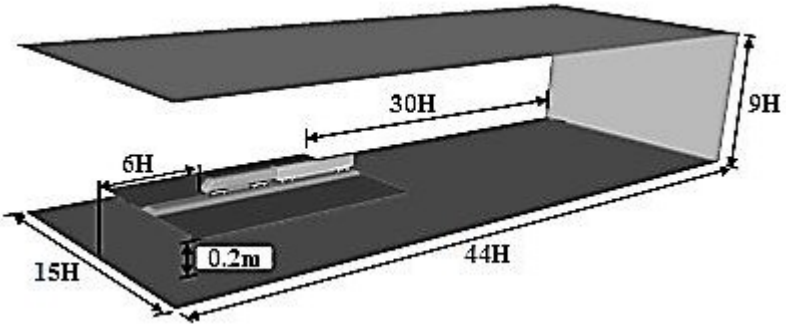

Figure 15: Computational domain with dimensions for RWDI simulations.

To ensure the finer details of the flow around the train are accurately captured three refinement regions were created. The largest of the refinement regions region extended to 1.5 train heights (H) each side of the train, 1H in front of the STBR step, 10H behind the train and 2H above the train. The medium refinement extended 1H in front of the train, 2H into the wake and 0.5H each side and above the train, whilst the smallest region extended from the top of the ballast to the mid axle height for the whole trains length and width. The final cell surface count for the lead engine car of the train were $7x10^4$, $1.3\ x10^5$, $1.7\ x10^5$ and $2.9\ x10^5$ for the coarse, medium, fine and very fine meshes respectively.

A visual overview of the refinement regions can be seen from above side on in Figure 16.

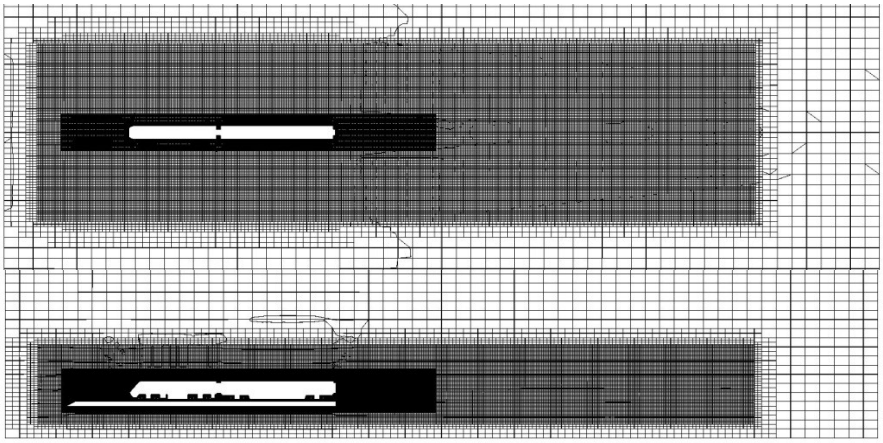

Figure 16: Cross sectional view of mesh at half train height (top) and COT position (bottom)

Figure 17 shows a close up view of the surface mesh for the “fine” mesh as well as a vertical slice through the centre of the domain, the denser mesh of the underbody refinement region can also be seen.

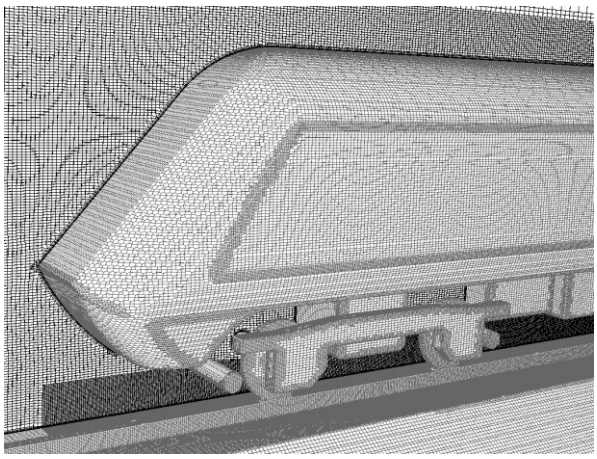

Figure 17: Close-up view of leading car and ballast, with a vertical slice through the COT position.

The y^+ values for each of the meshes when used approach can be seen below in Table 1. The y^+ value fluctuates between the different cases due to different predictions of flow

approaching the train, these differences originate over the leading edge of the ballast. The y^+ value was calculated using the inbuilt function within OpenFOAM via the equation:

$$y^+ \equiv \frac{u_f\, y}{\nu} \qquad 33$$

Where:

y = distance from wall

ν = kinematic viscosity

u_f = frictional velocity

Table 1: y^+ values for each of the four meshes.

Mesh	Cells (Million)	SST k-ω y^+ max	SST k-ω y^+ average	DDES y^+ max	DDES y^+ average
Coarse	18	64.6	25.4	106.0	34.7
Medium	24	56.6	21.9	82.3	27.3
Fine	34	43.1	13.4	51.9	15.7
Very fine	52	37.7	8.7	44.4	9.5

The final conclusion of the mesh dependency study was that beyond the fine mesh of 34 million cells no further increase in accuracy was obtainable. This conclusion was obtained by comparing the predicted aerodynamic drag and lift force coefficients as well as surface pressure coefficients with results obtained from the wind tunnel testing, the results of which can be seen below in Table 2 and Figure 18. It should be noted that the difference between fine and very fine meshes for the Lift Coefficient (C_l) in the DDES tests is due to rounding

with the actual difference less than 0.002 and therefore deemed negligible. Figure 18 shows C_p values for the four meshes using DDES compared to experimental results. The C_p values were calculated using the equation:

$$C_{p=}\frac{p_c-p_\infty}{0.5\rho u_\infty^2} \quad 34$$

Where:

p_c = pressure at cell

p_∞ = atmospheric pressure

ρ = fluid density

u_∞ = free stream velocity

The experimental results feature error bars of two standard deviations included as a margin of uncertainty for the experimental results. The results show that only the fine and very fine meshes are able to fully replicate the low pressure profile over the roof, For the SST k-ω results only the fine and very fine meshes were able to come close to replicating the peak.

Table 2: C_d and C_l values obtained during mesh dependency study.

	SST k-ω		Time Averaged DDES	
	C_d	C_l	C_d	C_l
Experimental	0.13	0.23	0.13	0.23
Very Fine	0.14	0.16	0.13	0.18
Fine	0.14	0.17	0.13	0.17
Medium	0.15	0.16	0.15	0.11
Coarse	0.16	0.16	0.21	0.02

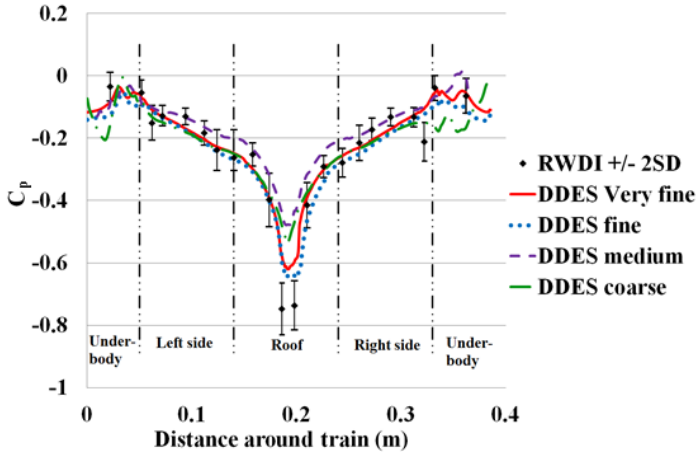

Figure 18: C_p measurements around train's surface for each of the four meshes using DDES. loop situated 0.11m back from trains nose.

3.4.2. Ballast height meshes

Using the mesh dependency study results obtained from the wind tunnel geometry as a guideline a more precise starting point could be determined for the ballast height mesh study. This led to a reduction in the number of meshes required for the mesh dependency study. The size of the computational domain was increased to 66H x 8.5H x 9H, with the trains nose situated 9H downwind of the domain inlet in a central position in regards to width. The blockage ratio for this domain size equalled 2%.

Three meshes were produced for the 0.75m ballast to perform a mesh sensitivity study, a 36 million cell coarse mesh, a 43 million cell medium mesh and a 48 million cell fine mesh. The meshes featured two refinement zones with one encompassing the other. The larger zone extended 5H in front of the train, 2.5H above the train, 2H either side of the train and 28H behind. The smaller refinement box extends 1.5H in front, 1.5H above, 1H either side of the train and 7H behind. These refinement regions can be seen in Figure 19 and Figure 20.

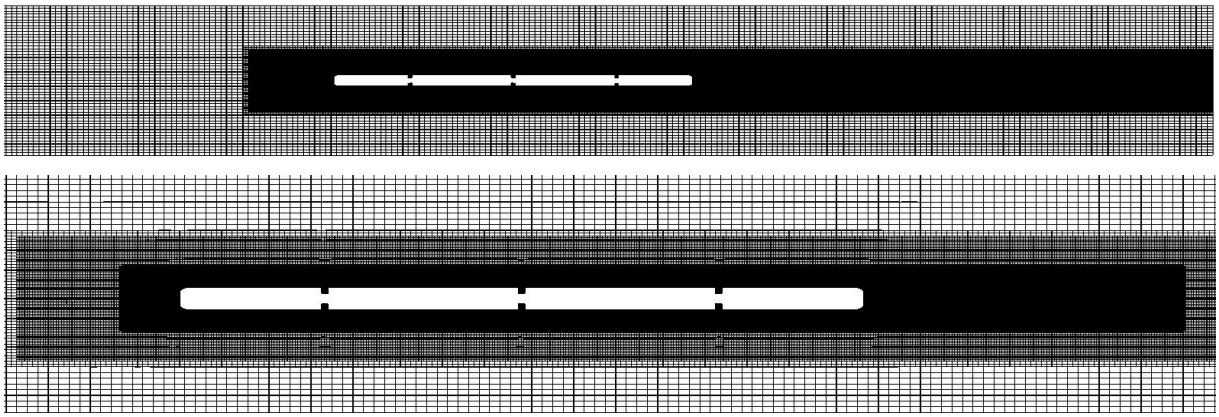

Figure 19: Refinement regions of ballast mesh viewed from above, Top: the full mesh at half train height. Bottom: close-up on smaller refinement region.

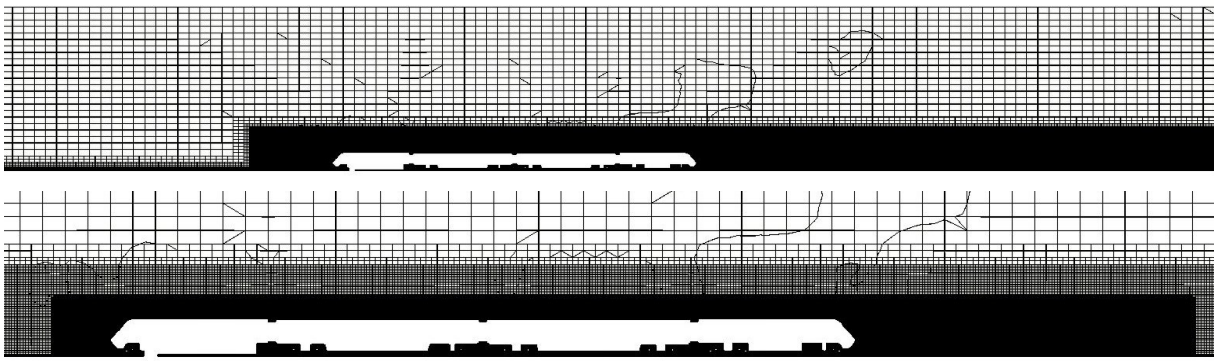

Figure 20: Refinement regions of ballast mesh viewed from the side, Top: the full mesh at COT. Bottom: close-up on smaller refinement region at COT.

The number of cells used to model the surfaces of the four cars of the train were 3.3 $x10^5$, 5.4 $x10^5$ and 7.4 $x10^5$ for the coarse, medium and fine meshes respectively. Despite the longer train the mesh cell count remained at a sensible level for the computational power available due to the removal of the additional refinement region within the underbody. This region was found to cause no significant effect upon the results obtained during the mesh dependency study within the numerical methods study section.

Each mesh comprised of five surface layers with the initial layer thickness of $2.5x10^{-5}$ m to give a y^+ of 60 when compared to the free stream velocity, final y^+ values for the majority of

the trains surface were within the range of 15 to 90. This is within the range accepted by the S-A turbulence model whilst using the wall function based upon the law of the wall (Spalding, 1961). The surface refinement and prism layers can be seen below in Figure 21.

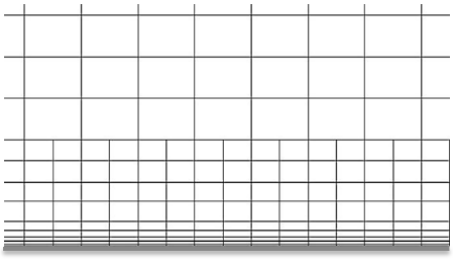

Figure 21: close-up on prism layers and surface refinement around the train, trains surface is the bottom line.

Comparison of aerodynamic force coefficients (Table 3) showed that the fine mesh produced no significant variation to the medium mesh. Further comparisons between time averaged pressure transients at a measurement location of 3m from COR and 1.2m above TOR also only showed minor variations which agreed with the finding of the medium mesh being suitable for producing non mesh dependent results.

Table 3: Aerodynamic force coefficients from medium and fine meshes for ballast effect tests.

	C_d	C_l
Coarse	0.397	0.010
Medium	0.411	0.012
Fine	0.410	0.012

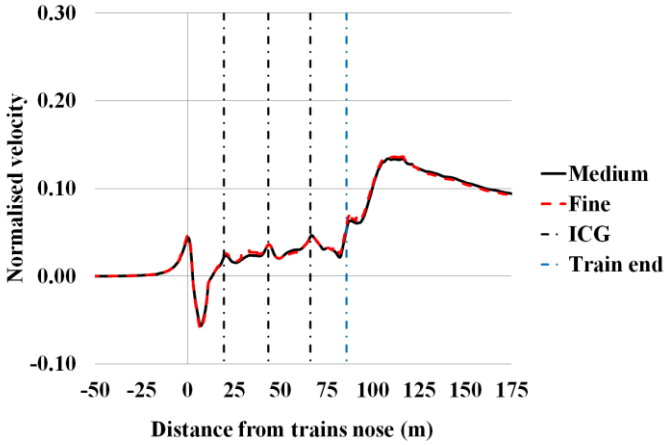

Figure 22: Mesh sensitivity study, normalised longitudinal velocity for medium and fine meshes with a 0.3m ballast

Figure 22 shows normalised longitudinal velocities measured at 3m from COT and 1.2m above TOR for both the medium and fine meshes, the results of the coarse mesh were not included as from the comparison of force coefficients the coarse mesh was deemed to be unsuitable and therefore would only clutter the graph. From the graph it can be seen that only negligible differences occur within the slipstream velocities for the two meshes.

3.4.3. Crosswind meshes

Due to the train geometry being identical to that used for the ballast height investigations the assumption was made that a mesh with the same surface and refinement statistics as the medium ballast height mesh would be optimal. To test this theory two meshes were produced and compared for the crosswind study, the meshes produced replicate the surface cell counts of the ballast height medium and fine meshes with refinements made upon the cell density in far regions to keep the total cell count within an acceptable range. The final cell surface counts were 5.4×10^5 for the medium mesh and 7.4×10^5.

To account for the crosswinds causing the trains slipstream to be asymmetric the domains size was increased to 6.5H on the windward side and 17H on the leeward side, these values were

chosen to match that of the crosswind generator at the TRAIN facility. The blockage ration of the computational domain varies from 2% to 3% as the yaw angle is increased from 5^o to 15^o respectively.

The refinement regions were also increased in width to account for the wake departing the train at an angle. The larger of the refinement regions extends 5H in front of the trains nose, 48H behind the train's nose and 7H above the TOR. The windward side of the refinement region extends 2H from COR, on the leeward side of the train the refinement region extends 8H from the COR. The smaller refinement region extends 1H and 2H From the COR for the windward and leeward sides respectively, 1.5H in front, 30H behind the trains nose and 1.5H above the TOR, these regions can be seen in Figure 23

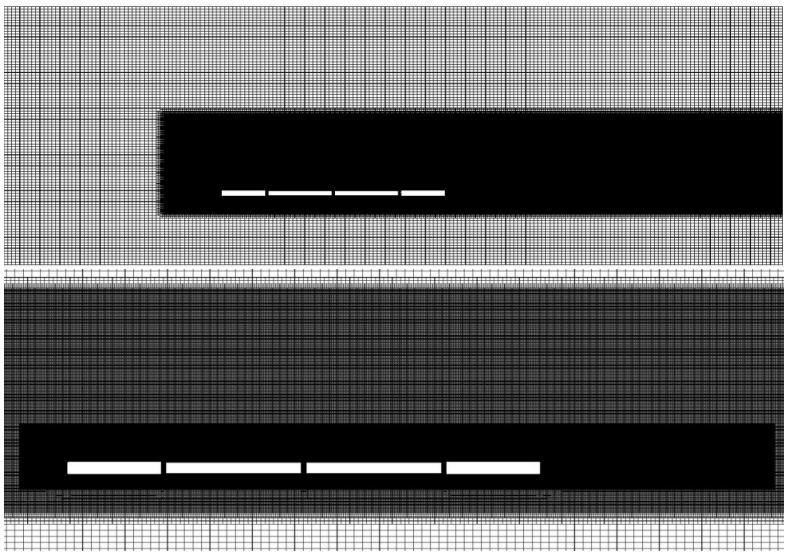

Figure 23: Refinement regions of crosswind mesh viewed from above, Top: the full mesh at half train height. Bottom: close-up on smaller refinement region.

Final cell counts for the meshes were $40.3x10^6$ and $74.5x10^6$ million cells for the medium and fine meshes respectively. Comparison of aerodynamic forces and time averaged pressure transients were compared for both meshes at a yaw angle of 10 degrees. Results of the

comparisons can be seen in Figure 24 and Table 4. The force coefficient results show only a small difference in both the drag and side force coefficients, this difference is around 0.01 for the drag value prior to rounding to three decimal places and was therefore deemed negligible. This shows that the extra refinement to the trains surface and particularly the wake region did not cause a significant effect upon the train.

Table 4: Aerodynamic force coefficients from medium and fine meshes for crosswind tests

	C_d	C_l	C_S	C_m
medium	0.543	0.059	0.528	0.051
fine	0.532	0.059	0.521	0.051

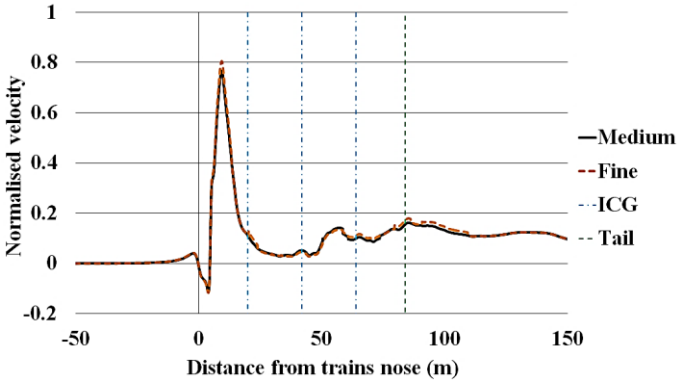

Figure 24: mesh sensitivity study of slipstream velocities upon leeward side of train at 10°. Measured at 2.5m from COT and 1.2m above TOR

Figure 24 shows the leeward side results for the slipstream normalised velocities at 2.5m from COT and 1.2m above TOR. Results were also compared for the windward side though only the leeward side features any discernible difference between the two meshes, the small differences between results was deemed to be negligible especially when computational time was taken into account. Therefore it was determined that the case results were not mesh sensitive.

3.5. Boundary conditions

Within each of the three mesh groups the train's surfaces were set as no-slip walls. For the RWDI wind tunnel simulations the ground plane, STBR and splitter plate were set as a no-slip walls. The sides and roof of the domain were set as slip walls to prevent the build-up of a boundary layer. Though this condition is not a realistic condition as a boundary layer would always form in real world situations the lack of a boundary layer on walls close to the train allows the use of a smaller domain without affecting the flow or pressures. The inlet was set as a constant velocity inlet at a velocity of 13.2 m/s to produce a uniform flow that is representative of the wind tunnel setup. The outlet of the domain was set as a fixed pressure of 0.

Both the ballast height and crosswind investigations used the same boundary conditions as the RWDI case for the outlet, roof and train boundaries. The ground surface was set as a no-slip moving wall with a velocity equal to that of the train's theoretical velocity (40 m/s). This boundary aims to replicate the conditions of a moving train through stationary air by removing the velocity difference that would occur between the free stream flow and ground plane had a stationary wall been used, therefore ensuring that no boundary layer forms for the flow heading directly towards the train. As the boundary condition is no-slip it allows the formation of a boundary layer when the flow is different to the trains theoretical direction and/or speed of travel. For the ballast height simulations the sides of the domain were set as a no-slip condition. To account for the y^+ values of the train and ground being above 1 the Spalding wall function was used.

By varying the inlet velocity component perpendicular to the train it is possible to change the flows yaw angle without the need to re-mesh a different rotated geometry. To ensure that the

full train experiences this crosswind component the sides of the domain were instead swapped to a constant velocity inlet condition and a fixed pressure outlet condition for the windward and leeward sides respectively. This approach was previously used successfully in the work of Flynn et al. (2015), Figure 25 shows this layout.

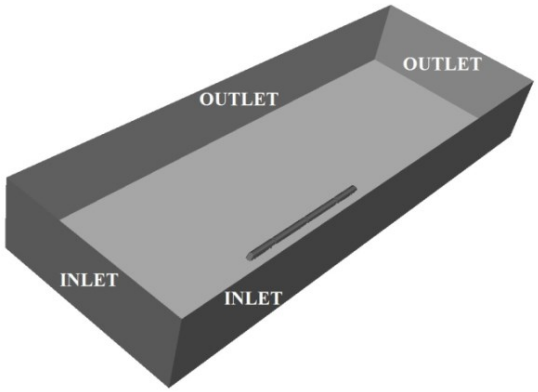

Figure 25: Inlet and outlet boundary walls for crosswind computational domain.

Chapter 4. Evaluation of CFD methodologies

4.1 Introduction

Before any simulations looking at the effect of yaw angles were conducted, it was first necessary to find the best-suited CFD approach and to evaluate its accuracy. To reduce the computation time required a smaller geometry case was chosen. The geometry chosen was a $1/25^{th}$ scale class 43 HST power car and towed passenger car mounted upon a STBR and splitter plate. This geometry was chosen as it matches the RWDI test previously mentioned in Chapter 3.1.1. The RWDI test provided an accurate benchmark due to the available data from the surface pressure taps over all surfaces of the leading car and the aerodynamic forces extrapolated from them. Two different CFD methodologies were investigated, the RANS approach with five different turbulence models and the DES approach, using both DES and the DDES variants with the S-A turbulence model. Five different turbulence models were investigated for the RANS approach, the S-A, k-ε, k-ε RNG, Realisable k-ε and SST k-ω.

These turbulence models were chosen to test the requirements made within the CEN, these are discussed in chapter 4.2. The choice to investigate the DES approach and its variant came from the lack of recommendations made with the CEN, this is despite the potential increases in accuracy these approaches are able to achieve.

Within this work the transient results were time averaged once the flow became fully developed. The flow was determined to be fully developed by monitoring aerodynamic forces and solution residuals until the values showed only small fluctuation over time. The averaging process was ended once the turbulence statistics no longer changed with time. By averaging the results it allowed the production of comparisons between the naturally transient DES

based approaches and the steady state RANS turbulence models. The work within this chapter also formed the basis of Morden et al. (2014).

4.2. CEN recommendations.

Requirements are made within the CEN on the appropriate CFD methodology to be used when conducting simulations of train aerodynamics. The requirements made for turbulence modelling state that when using the RANS approach only turbulence models that are classified as two equation or greater should be used. Furthermore it is stated that no k-ε based turbulence models should be used due to their inability to replicate natural wall normal behaviour without the use of wall functions. Both the LES and DES approaches are required to be proven valid for the setup currently being investigated. Spatial and time discretisation schemes should be set to at least second order to ensure accuracy and detail is maintained.

The CEN states that the surfaces of the train should be set as a non-slip boundary condition and that the track and ground surfaces should be set to moving unless replicating static testing for validation. For the ground and track surfaces it is stated the correct surface roughness should be used, however no recommendations are made on how this should be calculated or achieved.

4.3. Methods of Quality Assessment

In order to evaluate the accuracy of the multiple CFD approaches used, the obtained CFD results were compared to experimental results. It was determined that using aerodynamic forces alone would not provide enough detail and that the experimental pressure tapping data

should also be used. In order to make the handling of the large data sets more practical and provide a concise evaluation of each CFD approaches accuracy three quality assessment methods were used. The three different quality assessment methods were the hit rate (*q)*, which also forms part of the VDI guidelines (2005), the fractional bias (FB) (Cox and Tikvart, 1986) and Factor 2 methods.

These methods were applied to the analysis of CFD results previously in the works of Schatzmann et al. (2010), Buccolieri and Sabatino (2011) and Hertwig et al. (2012). Due to the manner by which these methods work they do not provide comparison of accuracy around aerodynamic features such as pressure spikes but instead provide an overview of the investigated region as a whole. This is especially true for both the *q* and Factor 2 methods, which are used to ensure the correct understanding of the results obtained by the FB method. The mathematical definitions of these methods are given below.

q is defined as:

$$q = \frac{1}{N}\sum_{i=1}^{N} n_i \tag{35}$$

Where:

$$n_i = \begin{cases} 1 \; for \left[\frac{p_i - o_i}{p_i}\right] \leq D \; or \; p_i - o_i \leq W \\ 0 \; for \; all \; else \end{cases} \tag{36}$$

where *N* is the number of measured points that fall upon the chosen location, *W* is the mean margin of error. The relative error, *D*, is set as 0.25 (25%) based on the recommendation

made in the VDI guidelines. Parameters p_i and o_i are the predicted and experimentally measured pressure coefficients respectively.

Factor 2 is defined as:

$$Factor\ 2 = \frac{1}{N}\sum_{i=1}^{N} n_i \tag{37}$$

Where:

$$n_i = \begin{cases} 1\ for\ 0.5\ \leq \frac{p_i}{o_i} \leq 2 \\ 0\ for\ all\ else \end{cases} \tag{38}$$

The range of possible results for both the q and factor 2 approaches is 0 to 1, with 1 representing a perfect match. For results below 1 it is impossible to determine if the inaccuracy is due to an overall trend to over or under predict.

FB is defined as:

$$FB = FB_{fn} - FB_{fp} \tag{39}$$

Where:

$$FB_{fn} = \frac{[o_i]_{fn} - [p_i]_{fn}}{0.5\left([o_i]_{fn} + [p_i]_{fn}\right)} \tag{40}$$

$$FB_{fp} = \frac{[o_i]_{fp} - [p_i]_{fp}}{0.5\left([o_i]_{fp} + [p_i]_{fp}\right)} \tag{41}$$

The FB method is limited in its application by its inability to be used with results that contain both positive and negative values. This limitation can be bypassed by first manually identifying and taking note of which results over predict and which under predict, and then multiplying the negative values by -1. Care must be taken in using the FB method on its own due to the ability of over predictions and under predictions to cancel each other out, resulting in an artificial increase in the accuracy value. In the FB square brackets represent the overall average of the field, the parameters *fp* and *fn* represent under and over prediction respectively. A FB value of 0 means there is perfect correlation between results, whilst a value above 0 represents an under prediction and below 0 an over prediction.

4.4. Results

Within this chapter results were compared to experimental data using aerodynamic forces and surface pressure coefficient (C_p) results. Comparisons of surface pressures were conducted using two approaches. Firstly visual comparisons are conducted over four measurement loops. Secondly comparisons were conducted using the aforementioned methods of quality assessment. The mesh statistics can be found in section 3.4.1 of the methodology chapter.

4.4.1. Comparison of Aerodynamic Forces

One method for the comparison of the seven investigated CFD approaches was to compare the predicted aerodynamic force coefficients to the ones collected from the wind tunnel investigation. Aerodynamic force coefficients were calculated during the experimental work by recording the average pressure from each of the 313 pressure taps situated upon the trains leading car. These pressure readings were then extrapolated over the trains surface to

calculate forces. For the CFD results to be comparable to the method used for the experimental results, viscous forces were ignored and only pressure forces from the trains leading car body were taken into account.

Table 5 shows a summary of the drag (C_d) and C_l coefficients for the seven CFD approaches and the experimental test. The C_d and C_l values vary greatly between the different CFD approaches showing the importance of choosing the correct numerical approach for each flow situation.

When comparing the C_d values the most accurate approach is the DDES approach which predicts the same C_d to two decimal places of accuracy. The DES approach under predicts the C_d by 0.01 whilst the SST k-ω and RNG k-ε approaches over predict the C_d by 0.01. The Realisable k- ε, standard k- ε and S-A approaches all greatly over predict the C_d with the S-A approach predicting a value of double the experimental.

The predictions of the C_l value by the CFD approaches were not as close, this is likely due to an insufficient pressure sensor resolution within the under body region of the experimental model resulting in missed pressure details. The most accurate CFD approach for the C_l is DES which predicts the C_l to be 0.18 compared to the experimental value of 0.23, this approach is closely followed in accuracy by the DDES and SST k-ω approaches which predict the C_l value to be 0.17. Once again the S-A approach is the least accurate, this time predicting a negative C_l value which is in the opposite direction to all the other approaches and the experimental results.

Table 5: Comparison of aerodynamic force predictions for power car.

	C_d	C_l
Experimental	0.13	0.23
S-A	0.27	-0.07
k-ε	0.23	0.17
Realizable k-ε	0.20	0.12
RNG k-ε	0.14	0.14
SST k-ω	0.14	0.17
DES (S-A model)	0.12	0.18
DDES (S-A model)	0.13	0.17

From the comparison of the aerodynamic force coefficients it can be seen that the three most accurate approaches were the two DES based approaches and the SST k-ω turbulence model. In situations where only the C_d is required the RNG k-ε approach is also capable of obtaining a high level of accuracy.

4.4.2. Comparison of Surface Pressures

In addition to comparing the aerodynamic forces predicted by the seven turbulence models to experimental data, the individual pressure tap data allowed for comparisons to be made using the surface pressure coefficients at each location. To allow quick analysis of the experimental results a large portion of the pressure taps were fitted in one of fifteen loops around the train, five of these loops were replicated within the CFD software for direct comparison, with the remaining loops ignored due to their close proximity to the five used. The location of four of

these loops can be seen in Figure 26. The results from the experimental work were time averaged over 120 seconds and are included in the graphs as points with bars. The bars represent +/- 1 Standard Deviation (SD) of the experimental results which is used as the margin of uncertainty for the experimental measurements.

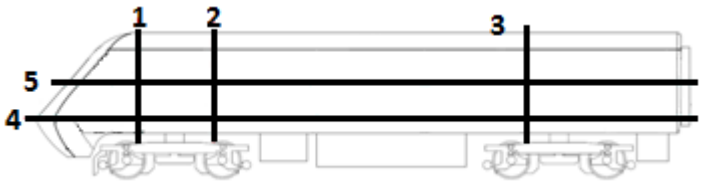

Figure 26: Loop locations upon first car.

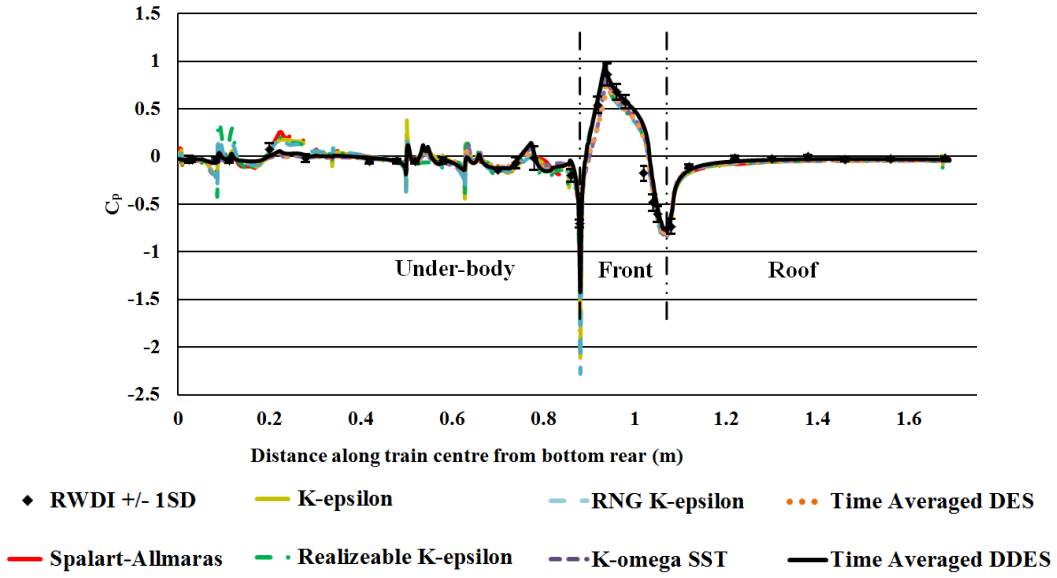

Figure 27: C_p at loop location 1. Situated 0.11m from the front of the train.

Figure 27 shows the time-averaged C_p around loop location one. This location features the largest pressure drop over the roof region. As distance from the roof centre increases the pressure increases towards atmospheric pressure. Over the sides of the train all approaches produce similar predictions that are within or close to the margin of uncertainty. The CFD approaches begin to diverge in their C_p predictions at the edges of the roof, here the DES and

DDES approaches begin to predict a larger C_p drop than the other approaches. This trend continues for the roof pressure drop spike where only the DES and DDES approaches get close to matching the experimental results. At the two pressure tap locations within this roof spike the DDES approach under predicts the C_p drop by slightly more than the margin of uncertainty. The DES results are less accurate than the DDES results while all other approaches predict results considerably outside of the margin of uncertainty. This under prediction is caused by the areas high sensitivity to the exact placement of the pressure tap and an inability of the DDES and DES approaches to accurately replicate any flow separation over the roof.

Within the underbody region the CFD results show a large amount of fluctuation for the C_p. This is not seen within the experimental results, this suggests that there was a lack of pressure taps within this region to provide a true analysis, this also backs up the assumption that this is the reason for the poor C_l correlation. However, it can be seen the Realizable k-ε turbulence model consistently predicts a C_p that is outside of the uncertainty range and is thus highly inaccurate within this region.

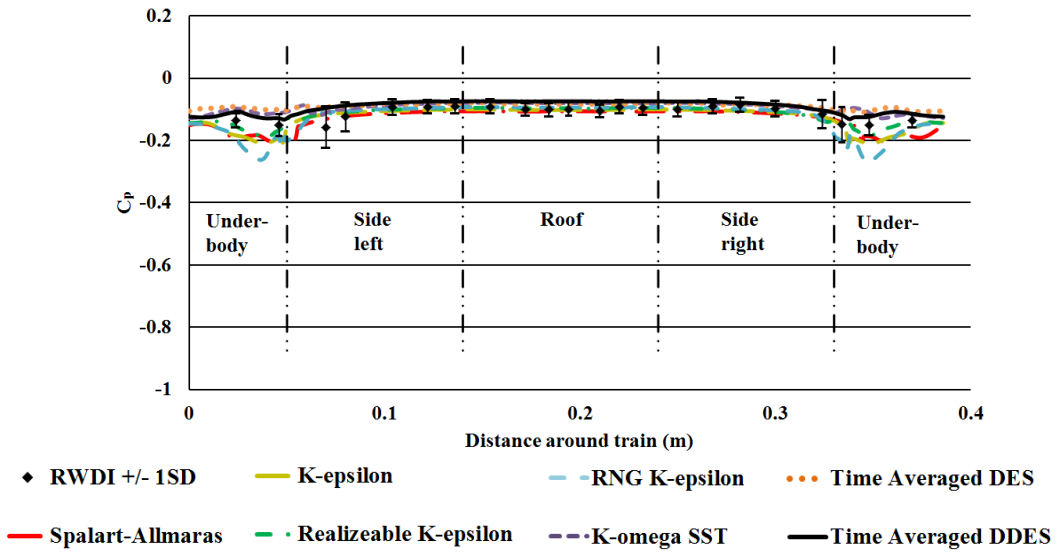

Figure 28: C_p at loop location 2. Situated 0.165m from the front of the train.

Figure 28 shows the CFD and experimental C_p's at loop location two. Unlike loop location one where there is a large variation in pressures around the surface of the train this location features a smaller C_p range. In all but the underbody region the different CFD approaches all fall within the experimental data's margin of uncertainty. The S-A turbulence model predicts a constantly larger negative C_p than all other approaches, the k-ε based turbulence models all predict similar C_p profiles that are smaller than the S-A results but lower than the k-ω SST and DES based results. Over the roof region the DDES approach is the only one to over predict the C_p though only slightly above the margin of uncertainty. Within the under body region the S-A and k-ε based turbulence models significantly over predict the pressure drop when compared to the experimental results. Within this region the DDES approach provides the closest results, falling within the margin of uncertainty at all points.

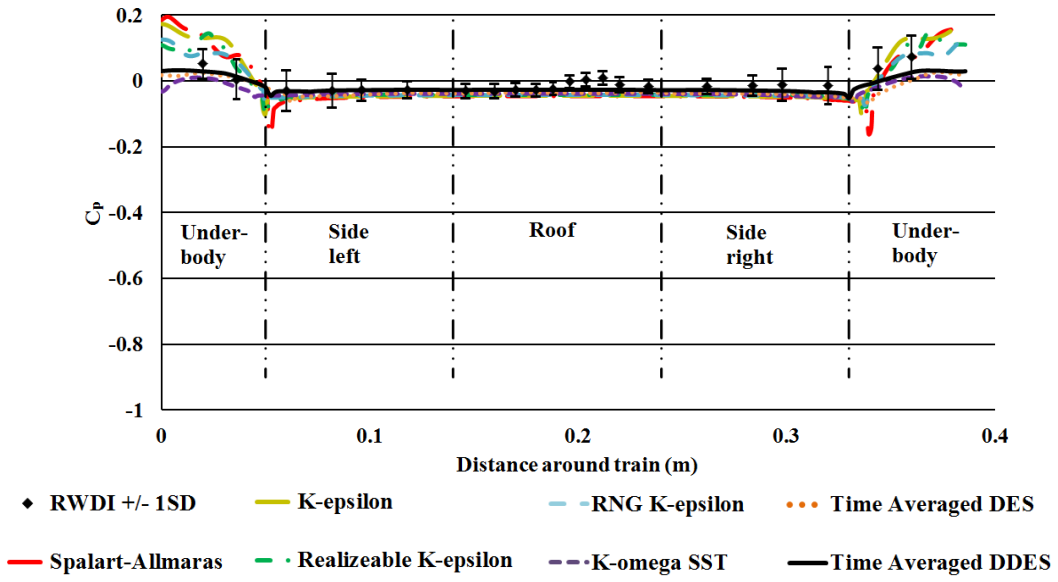

Figure 29: C_p at loop location 3. Situated 0.525m from the front of the train.

Figure 29 shows the C_p results for loop location three. At this location all of the CFD approaches fail to reproduce the pressure rise seen in the experimental data at the centre of the trains roof. This difference is due to differences between the wind tunnel and CFD geometries, due to the experimental model featuring ribs running along the trains surface. This difference in geometries was necessary for the building of a suitable computational mesh without elongated cells. Along the trains sides all of the CFD approaches fall within the margin of uncertainty range, of the CFD approaches the DDES approach proved to be the most accurate, regularly calculating the value closest to the experimental results. Within the trains underbody region, the CFD approaches split into two different C_p trends, the time averaged DDES, DES and SST k-ω models all under predict the C_p rise that occurs whilst all other approaches over predicting the rise in C_p. Most results within this region however stay within the +/- 1SD range of the experiment in particular the time averaged DDES approach and k-ω turbulence model.

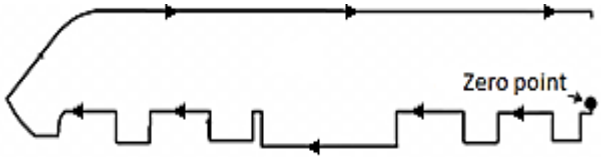

Figure 30: Loop along train centre line.

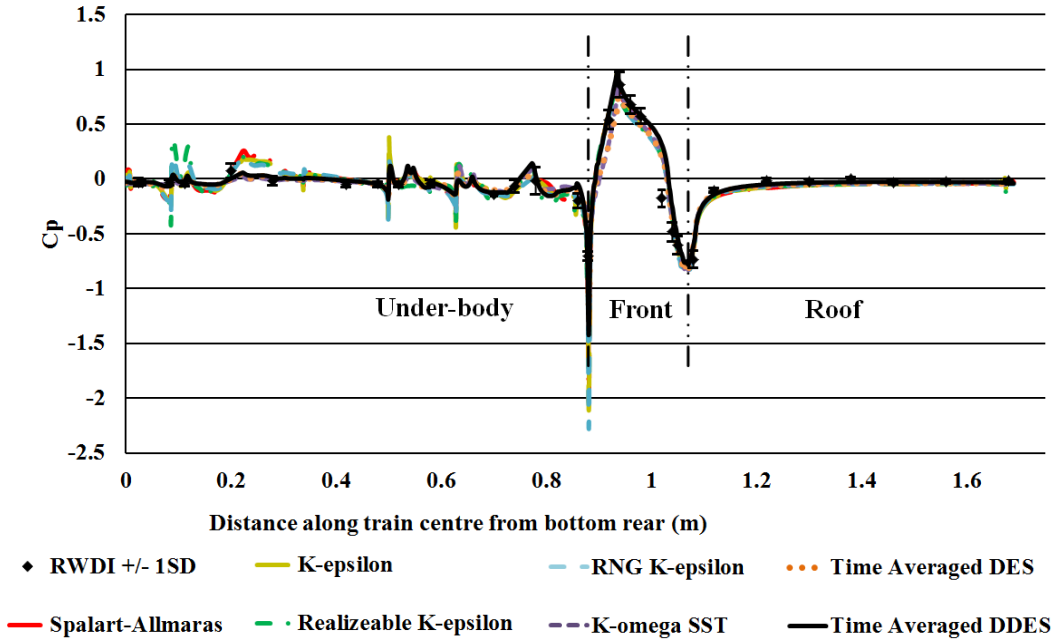

Figure 31: C_p along train centre line.

Figure 30 shows the location and direction of loop four, this loop goes around the train at the centre of the trains width, Figure 31 shows the C_p results for each of the CFD approaches along this loop. This loop features the greatest number of underbody pressure probe locations from the experimental results and thus provides the most complete view of the pressures within the underbody region. Within the underbody region the S-A and k-ε based turbulence models frequently over predict the pressure spikes by a large factor. The DES based and SST k-ω approaches all produce smaller peaks that more closely match that of the experimental recordings.

All approaches over predict the negative C_p spike on the edge between the front and the underbody regions by at least 200% with the standard and realizable k-ε models over predicting by 300%. This large variation however may just be due to placement of the pressure tap as this region would be highly sensitive to the slightest differences in measurement location due to the flow separation. Around the front of the train and over the

roof region all CFD approaches follow a similar trend to that of the experimental results, often falling within the margin of uncertainty.

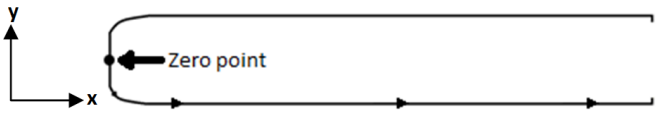

Figure 32: loop start location and direction.

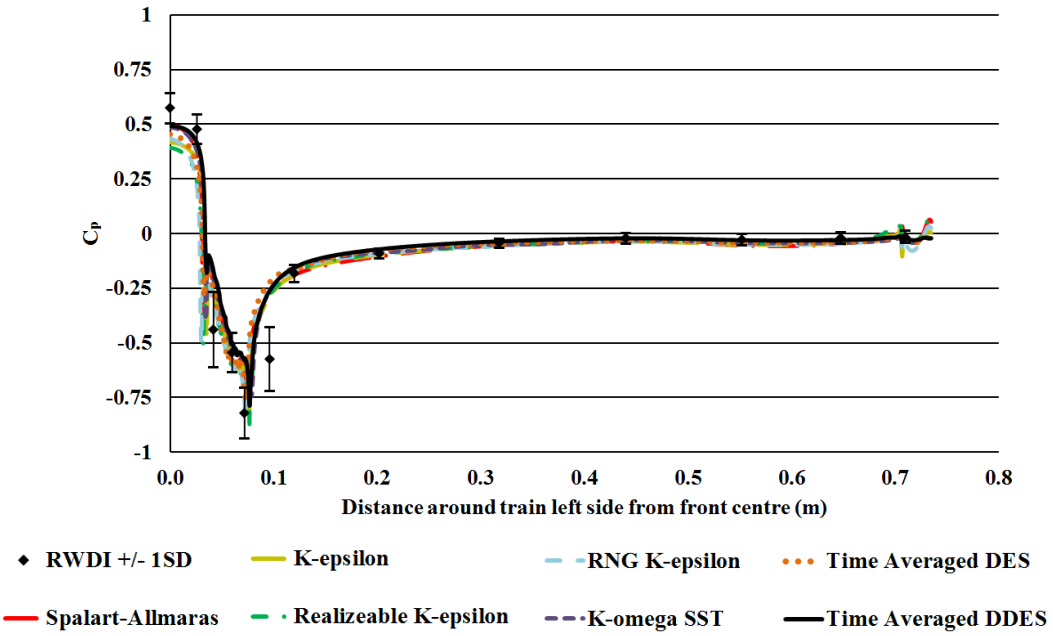

Figure 33: C_p at loop location 4. Situated 0.0675m above TOR.

Figure 33 shows the location and direction of loop five which is situated around the left hand side of the train, results for each of the turbulence models at this loop are shown in Figure 32. The high pressure measured around the centre of the nose region in the experimental work is best replicated by the DDES and S-A CFD approaches, the DES approach proves to be less accurate whilst the k-ε based turbulence models provide the worst accuracy. Due to this

location being right at the front of the train the reasons for the differences in pressure can be attributed to how flow is handled over the STBR step ahead of the train.

Around the curved edge between the front and sides of the train all approaches make similar predictions for the C_p, though in this region the k-ε and Realizable k-ε turbulence models prove to be the most accurate at replicating the low C_p point of around -0.45. These approaches predict a large pressure drop spike that the other approaches do not, this is because all other approaches under predict the flow separation that occurs at this point. Along the side of the train it is hard to differentiate between the different CFD approaches as they all fall within the margins of uncertainty, the DDES approach however can be determined to be slightly better due to generally fitting closest to the exact experimental results.

4.4.3. Analysis of results via Quality assessment approaches

Table 6 shows the results of the three quality assessment methods when comparing CFD results to the experimental data obtained from the 313 pressure taps. The q method of quality assessment shows that the DDES approach is the most accurate with an accuracy of 88%, this is a large improvement over the standard DES approach which only manages an accuracy of 82%. The DDES approach also proves to be the most accurate for the FB and Factor 2 methods. Of the RANS approaches the SST k-ω turbulence model is the most accurate followed by the S-A turbulence model. The k-ε based turbulence models prove to be the three least accurate.

The FB method of analysis shows that all approaches under predict the C_p except the SST k-ω turbulence model which over predicts. The Factor 2 method of assessment produces the closest set of results between the CFD approaches, using this method of assessment the SST

k-ω turbulence model proves to be slightly more accurate than the DES approach though still less than the DDES approach.

Table 6: Comparison table showing summary of result analysis using the three quality assessment approaches.

	q	FB	Factor 2
Ideal	1	0	1
S-A	0.75	1.75	0.73
k-ε	0.73	1.88	0.72
Realizable k-ε	0.74	1.41	0.74
RNG k-ε	0.72	2.79	0.75
SST k-ω	0.77	-1.69	0.79
Time Averaged DES	0.82	1.22	0.78
Time Averaged DDES	0.88	1.1	0.81

4.5. Conclusion of experimental validation.

Through visual comparison of the CFD approaches to experimental data it can be seen that the DES, DDES and SST k-ω approaches are best able to replicate the profiles around the loop locations. Along the sides of the train all approaches produce a good level of accuracy falling within the margin of uncertainty. Over the roof at the front of the train only the three fore mentioned approaches closely predict the negative pressure spike, with the DDES approach being the closest.

Within the underbody region the S-A and k-ε based turbulence models fail to match experimental results. Large fluctuations in C_p can be seen in Figure 31, In this region the DES and DDES approaches consistently match the experimental results profile with the DDES results falling within the margin of uncertainty at most locations. These findings match the results of the three quality assessment methods which all calculate the DDES approach to be the most accurate with the DES and SST k-ω approaches being the second and third most accurate respectively. The FB approach calculates the DDES approach to feature a general trend to under predict the surface C_p, this coincides with the findings from comparing aerodynamic forces where the DDES approach under predicts the C_l.

The results from the comparison of aerodynamic forces match the results of both the quality assessment and visual analysis. The force results show the DES, DDES and SST k-ω approaches provide the highest levels of accuracy. The aerodynamic forces show that the S-A, k-ε and Realisable k-ε turbulence models greatly over predict C_d, with the S-A also predicting a negative C_l value unlike all other approaches. It can be seen from this part of the investigation that the S-A and k-ε based turbulence models are not suitable for this type of investigation as is stated in the CEN recommendations. These approaches fail to replicate pressure spikes and produce an overall low level of accuracy when comparing surface pressures and aerodynamic forces.

From these findings remaining research is going to be conducted using only the DDES approach. The decision to not further include the SST k-ω turbulence model despite it being the most accurate of the RANS approaches was due to its high over estimation of surface pressures on a whole, and its inability to replicate key areas of the pressure profile such as over the leading roof edge. This is particularly important as crosswinds can potentially cause flow separation at other regions of the roof.

Differences exist between the predictions of each turbulence model due to how they calculate the Reynolds stresses that form during the Reynolds averaging and decomposition of the Navier-Stokes equations. These Reynolds stresses are variables that cannot be solved directly due to too many unknowns, instead the Reynolds stresses must be approximated using mathematical models. The formation of the Reynolds stresses is commonly referred to as the closure problem.

Chapter 5. Effects of varying ballast height

5.1. Introduction

Research within this chapter examines the effects ballast height causes upon the slipstream and wake regions of a high-speed passenger train. It is important to establish if ballast height causes any effect on the flow regime around a train for two reasons. Firstly it is necessary to determine if ballast height causes changes within the slipstream so that a final geometry that will be used when investigating crosswinds can be chosen. Secondly it is important to know if ballast height causes any effects on the slipstream as this will be important to full scale trains and the regulations they are built to. If the ballast height is shown to cause an effect upon the slipstream of the train, then it is necessary that the crosswind cases are run upon the flat ground geometry to remove any ballast effects.

Three different ballast heights were selected, a flat ground geometry, a 0.3m (at full scale) and a 0.75m (at full scale). All three of these ballast heights were investigated at the TRAIN facility by Soper et al. (2016). A ballast height of 0.3m was chosen as this is representative of a large portion of the UK's ballast, Furthermore this ballast height matches that of the Uffington location used for full scale measurements used within the " The measurement of train aerodynamic phenomena in operational conditions" project that this research is part of. The 0.75m ballast height is representative of an average ballast height in Europe and most closely conforms to the TSI recommendation of a STBR with a height of 0.825m ± 0.25m when conducting numerical simulations and 0.75m ± 0.25m when conducting full scale testing, CEN (2009). In order to enable easier reference to regulations and provide an increased sense of how the results presented relate to real trains, all dimensions within this thesis from this point forward will reference full scale dimensions.

Research conducted by Soper et al. (2016) found that the inclusion of a ballast shoulder caused the velocities at measurement locations to reduce over that of a flat ground case, this resulted in velocities that were further from the TSI limits at higher ballast heights. It was also found by the authors that smaller ballast heights lead to confinement of the flow to a smaller area than that of larger ballast heights. Results collected by the authors showed that pressures throughout the slipstream were relatively unaffected by the inclusion of different height ballasts. The experimental data gathered by the authors and published within this research is used within this chapter for validation of the CFD approach used.

Research conducted in Bell et al (2014) used a $1/10^{th}$ scale, one and a half car ICE2 model in wind tunnel tests where both flat ground and STBR ground setups were tested. The authors found that the lower slipstream vortices in a flat ground case moved outward at a higher speed than in the STBR case and were at a greater intensity within the measurement location, nose and tail velocity peaks were also recorded at nearly double the STBR level.

Each of the three ballast heights were tested using the DDES approach based upon the results of Chapter 3. The three meshes were all produced with the same parameters to ensure no variation due to mesh dependency occur. The mesh parameters were extrapolated from the results found in the mesh sensitivity study conducted upon the wind tunnel geometry. Within this chapter results are first validated for each of the ballast heights against experimental data obtained at the TRAIN facility, this validation uses one measurement location for each of the three investigated ballast heights. Results are then compared for the three ballast configurations C_p and normalised velocity values along measurement lines situated within the slipstream. Finally results are visually compared between the three configurations using velocity contours and path lines projected on planes perpendicular to the free stream flow.

The purpose of visual comparison is to provide further insight into the flow fields around the train and an overview as to how they are affected by ballast height.

5.2. Comparison of CFD results to experimental data

In order to compare the slipstream characteristics at different ballast heights it was first necessary to validate the CFD approach being used for external flow. The validation was conducted by comparing the DDES results with the experimental data collected at the TRAIN rig. Comparisons were conducted using profiles of the horizontal velocity within the trains slipstream at a measurement location of 3m from COT and 1.2m above TOR for the three different ballast geometries. A limitation of the experimental setup is the probes used to record the flow velocity feature a measurement "cone". The cone covers a range of 45^{o} from the central axis of the probes front face, outside of which the probe is unable to record the velocity. Due to this limitation any flow recirculation which occurs around the nose of the train cannot be measured. The effects of this limitation can be seen in the following figures where just after the trains nose the experimental data momentarily cuts out.

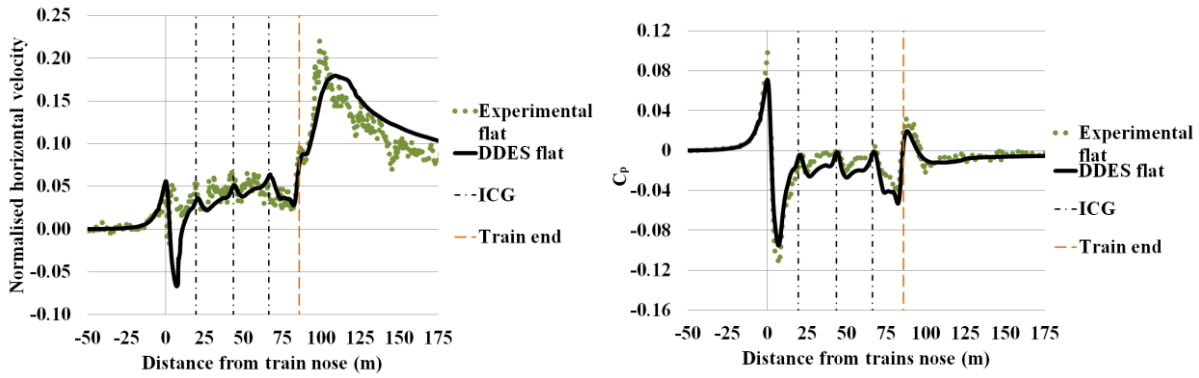

Figure 34: Experimental and CFD results for the normalised horizontal velocity and C_p profiles at 3m from COT and 1.2m above TOR for a flat ground geometry.

Figure 34 shows the normalised horizontal velocity for the flat ground cases. The DDES results are able to accurately replicate the profile of the experimental results though show a small overall trend of under prediction. For the normalised velocity the CFD results are constantly below that of the experimental until the wake region. This signifies the boundary layer growth rate in the CFD simulations is below that of the experimental setup, showing a limitation of using wall functions.

Flow features such as the velocity peaks during the Inter Carriage Gap's (ICG) correlate well with the experimental results in regards to location along train and fluctuation magnitude. The initial velocity spike at the trains nose matches well with the experimental results however the tail velocity peak is around 30% lower in the CFD results. This difference between the two approaches shows that the CFD results do not predict the wake to extend as far from the train as occurs within the experimental tests. Within the wake the rate at which velocities drop is similar between both methods though the CFD wake is set further back. This reinforces the explanation for the wake peak differences previously mentioned as this would be a side effect of different wake expansion rates.

When comparing the CFD pressure results with the experimental data it can be seen that apart from the peaks around the nose region all other pressure peaks are closely predicted. Differences at the peaks are potentially due to un-measureable differences in the measurement probes location between the CFD and experimental setup. Along the side of the second and third cars (19.5m – 66.25m) the pressure coefficients from the CFD investigation are lower than that of the experimental results. This difference is due to the CFD results predicting the ICG pressure spike to dissipate at a higher rate than occurred within the experimental setup. Within the wake the pressures match well but both peaks are failed to be replicated exactly within the CFD, this area of the train features a complex geometry with large regions where a

negative pressure gradient exists. The peaks are not replicated accurately within the CFD simulation due to the DDES approach failing to replicate flow separation and reattachment within the area.

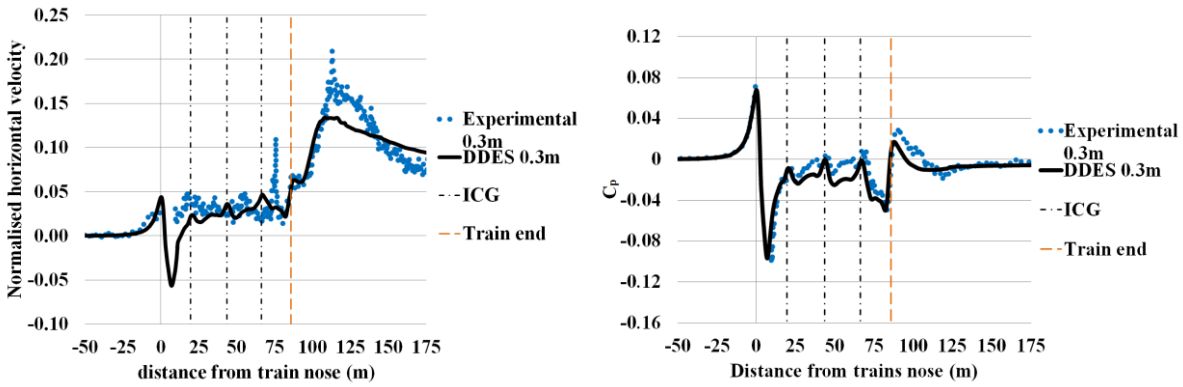

Figure 35: Experimental and CFD results for the normalised horizontal velocity and C_p Profiles at 3m from COT and 1.2m above TOR for a 0.3m ballast geometry.

Figure 35 shows the same measurement location as used in Figure 34 but now with a 0.3m ballast height, as before the DDES results show a general trend to under predict the normalised horizontal velocity when compared to experimental results. At this ballast height a velocity spike can be seen to occur around 75m after the nose of the train, this velocity spike is missed from the DDES results however this spike is not seen in the flat ground and 0.75m cases. This spike is either an anomaly, though unlikely as this is an ensemble average of twenty five runs or is a region where a small but strong flow feature exists. If this in indeed a small flow feature then it is possible the CFD predicts this feature in a slightly different location and is therefore missed by the measurement line. It is also likely that this flow feature exists in the experimental cases at 0.75m and flat ground but again misses the measurement location.

The tail velocity spike is less accurately replicated at this ballast height than in the flat ground case with a difference of nearly 40%. It is likely that this is due to the same effect as in the flat ground case with different rates of wake expansion, but is now exacerbated by the inclusion of a ballast slope. The C_p profile around the nose is once again accurately predicted by the CFD software, with both the positive and negative spikes matching better than in the flat ground case. Along the side of the trains second and third cars (19.5m – 66.25m) the C_p is again predicted to be of a larger negative magnitude than that of the experimental results, this trend was seen within the flat ground case but to a lesser extent as the experimental pressures were at a larger negative value. In comparison to the flat ground case the positive tail pressure pulse is also less accurately predicted when compared to experimental data with the CFD pressure dropping sooner than that of the experimental data.

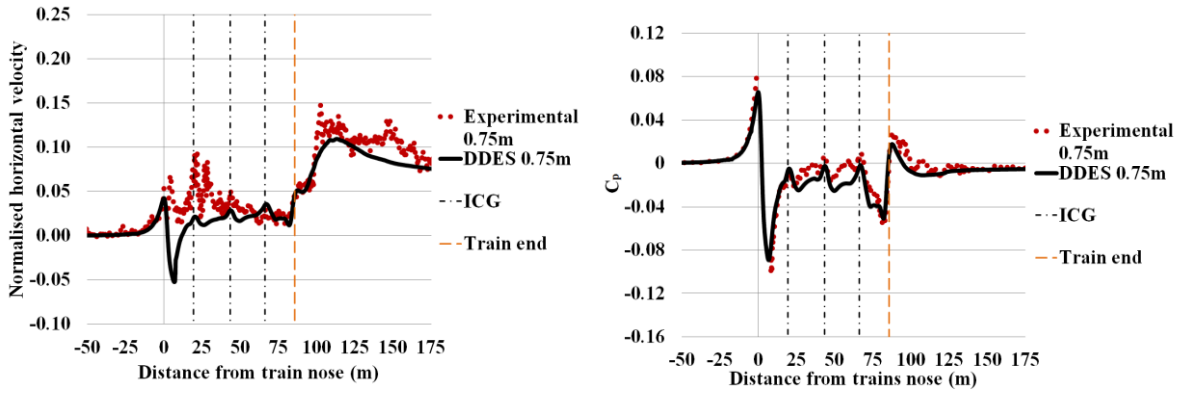

Figure 36: Experimental and CFD results for the normalised horizontal velocity and C_p Profiles at 3m from COT and 1.2m above TOR for a 0.75m ballast geometry.

Figure 36 shows results for the 0.75m ballast height. Around the first and second cars (0m – 43.5m after the nose) the experimental velocities are considerably higher than in the lesser two ballast heights. A result of this is the CFD case which features velocities lower than that

of the lesser ballast heights now shows a large level of under prediction. Due to the nature of this occurring whilst the ballast is at its highest this increase in experimental flow velocity is likely due to a region of high velocity flow being drawn downward into the measurement region, something not replicated within the CFD. CFD results along the length of the third and fourth cars (43.5m – 85.75m) correlate well with the experimental results but the CFD results under predict the velocity within the wake region, this difference may be caused by the higher velocity wake being situated lower down the ballast within the CFD simulations.

The C_p results follow the trend of the former two ballast heights investigated with good correlation for pressure pulses and a constantly lower pressure predicted along the second and third (19.5m – 66.25m) cars. Within the tail region the CFD results are a closer match to experimental data than in the 0.3m case but still show a larger difference than the flat ground results.

When comparing the normalised velocities for the three sets of ballast heights to their comparable experimental results it can be seen that as the ballast height is increased there is an increase in variance between the measurements from the two techniques. This increase is partly caused by differences between the surface roughness parameters used for the CFD and the experimental setup. Experimental surface roughness was not measured within this research and instead non slip conditions were imposed over a smooth surface for the CFD work. This is unlike the experimental setups for the 0.3m and 0.75m ballast cases which relied upon a cut MDF surface which was not smooth. The flat ground experimental setup however had a smooth non cut MDF surface finish which potentially accounts for the increased comparability between the two approaches with no ballast height. Within all three numerical studies the surface roughness was set the same as to remove one variable that could contribute to differences in the ballast height results.

5.3. Evaluation of ballast heights effect upon the slipstream.

To investigate the effects ballast height causes upon a trains slipstream measurements were collected for the normalised sum velocity (X, Y and Z components) and pressure coefficients along four measurement locations. These measurement locations were lines that spanned the entire computational domains length, the locations for each of the lines were based from the COT and the TOR with each lines zero point being at the trains nose. The locations used for the four lines were: 3m from COT by 0.2m above TOR, 3m from COT by 1.2m above TOR, 2.5m from COT by 0.2m above TOR and 2.5m from COT by 2.1m above TOR. The choice to use these four locations was due to each location corresponding to TSI measurement locations and due to the wide spread between them. From the study of literature the wide spread between locations should cover different regions of the slipstream. The location of these locations can be seen below in Figure 37

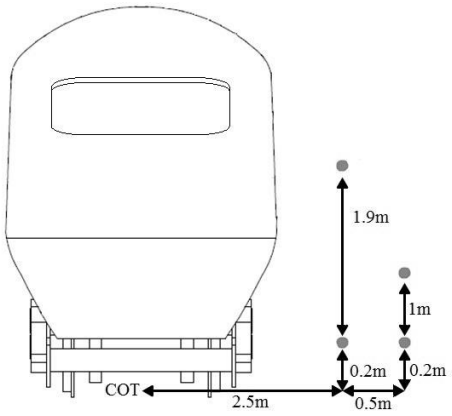

Figure 37: Location of measurement points in relation to COT (horizontal) and TOR (vertical).

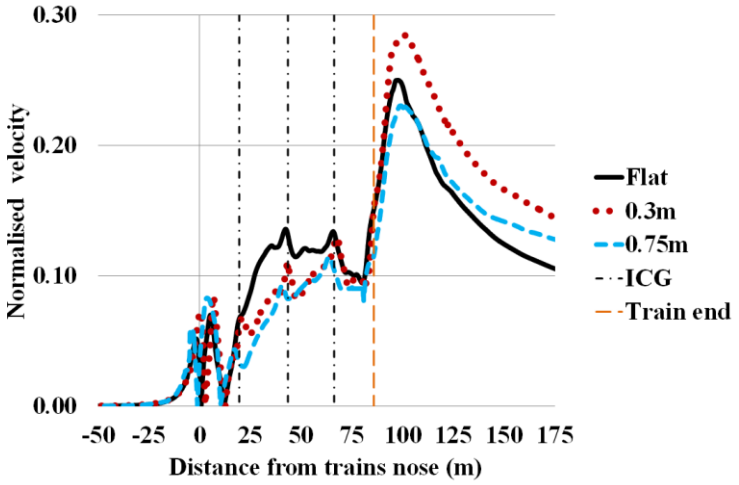

Figure 38: Normalised velocities at 3m from COT by 0.2m from TOR.

Figure 38 shows the normalised velocity at 3m from COT and 0.2m above TOR. Within this location of the slipstream ballast height causes no significant effect upon the normalised velocities around the first car of the train. From the start of the second car (19.5 m) the normalised velocities begin to show differences at each ballast height. The flat ground results show the highest velocity whilst the 0.3m and 0.75m ballast heights show lower velocities. From the results in section 5.4 it can be seen that this difference is caused by the slipstream being drawn down by the increasing ballast heights. The difference between the 0.3m and 0.75m ballast heights is considerably smaller than that of the flat ground and 0.3m ballast height.

Between the start of the second and end of the third car the slipstream velocity continues to rise for the 0.3m and 0.75m cases whilst the slipstream velocity for the flat ground case remains steady. This is due to the ground level vortex core within the slipstream moving down the ballast and away from the measurement point as can be seen in section 5.4. By the end of the third car the slipstream velocities at all three ballast heights are again equal. At the

beginning of the fourth car (66.25 m) a further velocity spike occurs, the rate at which the slipstream velocity grows in this spike is consistent between all three ballast heights.

The final peak value of this tail velocity is highest in the 0.3m case with the flat ground and 0.75m results predicting lower velocities. This suggests that a different portion of the wake is within the measurement region for the 0.3m case, though the velocity range within this region is too sensitive to be seen within the wake results of section 5.4. The rate at which the velocity drops back off is at the same rate for the flat ground and 0.3m ballast heights, however the rate for the 0.75m ballast shoulder is lower. This may be due to a higher velocity part of the wake being drawn into the measurement region at this ballast height, again the variation is too small to clearly identify within section 5.4.

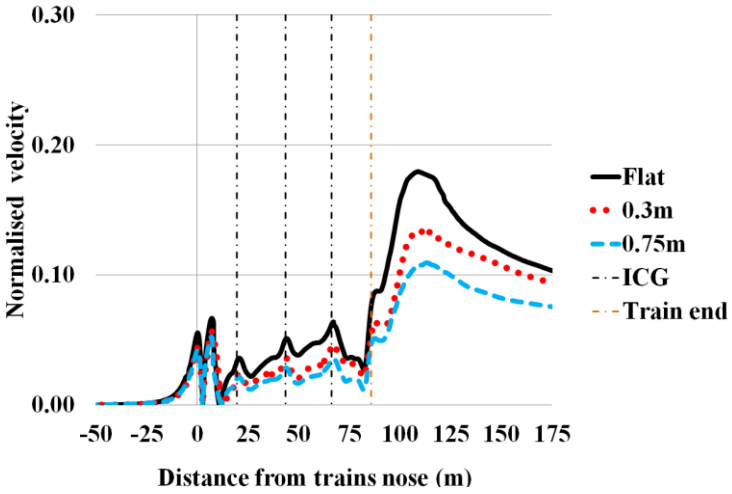

Figure 39: Normalised velocities at 3m from COT by 1.2m from TOR.

Figure 39 shows the normalised velocity within the trains slipstream at a measurement location of 3m form the COT and 1.2m above TOR. Along this location a clearer and more consistent effect of ballast height on slipstream velocities can be seen when compared to Figure 38. The initial velocity spike and flow reversal spike (second spike) around the trains

nose can be seen to be larger for the flat ground case than for either of the raised ballast cases. Before the end of the first car (< 19.5m) the flat ground slipstream features a higher velocity than that of two ballast cases. This trend continues until the end of the fourth car (85.75m) where all three results momentarily converge. At this measurement location the results show a difference due to differences in the size and location of a vortex located along the trains side. In the ballast height cases the vortex is larger though not stronger, this is due to the vortex having a larger area to expand into as the ground plane vortex is situated further away, this effect can be seen in the results of section 5.4.

Along the second and third cars (19.5m –66.25m) the gap between the 0.3m and the 0.75m results remains constant. Beyond the trains tail the three ballast heights again show a clearer effect on the velocities, in this region the flat ground predicts a peak velocity of approximately 70% more than that of the 0.75m ballast height. This measurement location is situated upon the outskirts of the wake in the flat ground case, when the ballast height is increased the wake is pulled slightly down in turn missing the measurement point.

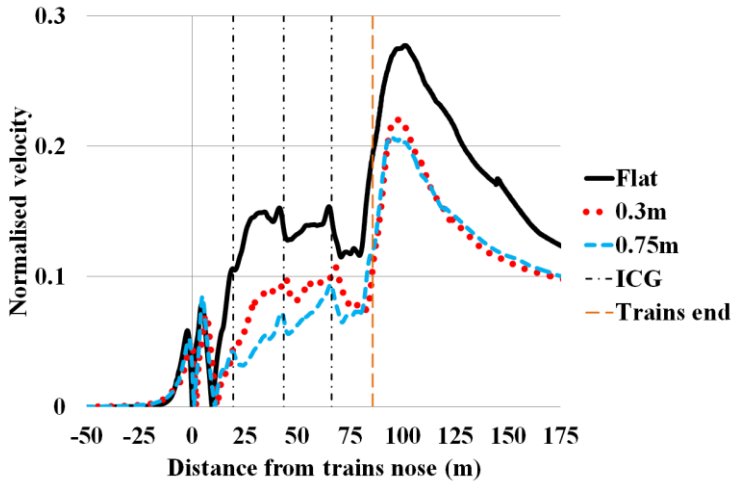

Figure 40: Normalised velocities at 2.5m from COT by 0.2m from TOR.

Figure 40 shows the normalised velocity results for the measurement location that is located the deepest within the slipstream, being situated at 2.5m from the COT and 0.2m above the TOR. The results at this location are more sensitive to ballast profile than at the 3m from COT location, the reason for this is this measurement location is nearer to the core of the slipstream and is therefore more sensitive to movement of the slipstream. After the initial velocity spike and flow reversal spike the results begin to separate, the flat ground slipstream features a constantly higher velocity than either the 0.3m or 0.75m ballast heights. Along the second and third cars (19.5m – 66.25m) the difference between the flat ground and the 0.3m ballast height velocities are around 50%. For the 0.75m ballast the difference is around 200% for the second car and 100% along the third car. These differences in velocity are the largest measured at any of the measurement locations investigated. Along the side and after the fourth car both the 0.3m and 0.75m ballast heights predict similar velocities. At the final velocity spike (100m) the difference between the flat ground and two other results is around 30% with the flat ground producing the highest velocity, this is caused by the wake being slightly less wide due to the ballast allowing the wake to dissipate over a larger area.

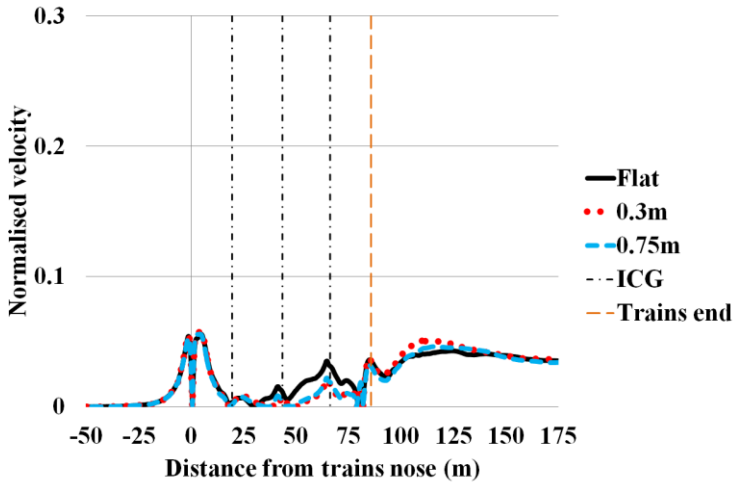

Figure 41: Normalised velocities at 2.5m from COT by 2.1m from TOR.

Figure 41 shows the normalised velocities within the slipstream at 2.5m from COT and 2.1m above TOR. At this measurement location the slipstream velocities are considerably smaller than at the other measurement locations, this is because this location is on the outskirts of the slipstream as can be seen in section 5.4. Along the first car the velocity is calculated to be the same at all three ballast heights. For the second and third cars (19.5m – 66.25m) the velocity increases at a higher rate for the flat ground than for both the 0.3m and 0.75m results. The fourth car (66.25m – 85.75m) produces a larger velocity drop than in the other measurement locations, this brings the velocities at different ballast heights back to similar predictions. Following this larger velocity drop the positive velocity spike is greatly reduced when compared to other measurement locations, this is followed by a second spike starting at around 100m. This second spike peaks with the 0.3m ballast height predicting the highest velocity followed by the 0.75m ballast height.

From the four measurement locations it can be seen that the general trend is for the velocities within the slipstream at each location to decrease as ballast height increases. The most sensitive regions to ballast height are the two measurement locations situated at 0.2m above TOR, this is due to their location in the high velocity flow near the ground level. The 3m by 1.2m location is less sensitive due to being in a region where the slipstream velocities are half of the lower two locations values. The 2.5m by 2.1m location is the least sensitive to ballast height as it falls on the very outskirts of the slipstream, which can be determined by the very low velocities and results shown in section 5.4. The most sensitive regions of the train are along the second and third cars, this is due to the slipstream requiring the length of the first car to build up and the final car featuring a large velocity drop before the flow enters the

wake. For this reason it can be assumed that on a longer train the ballast effect would continue to exist for all but the first and last cars.

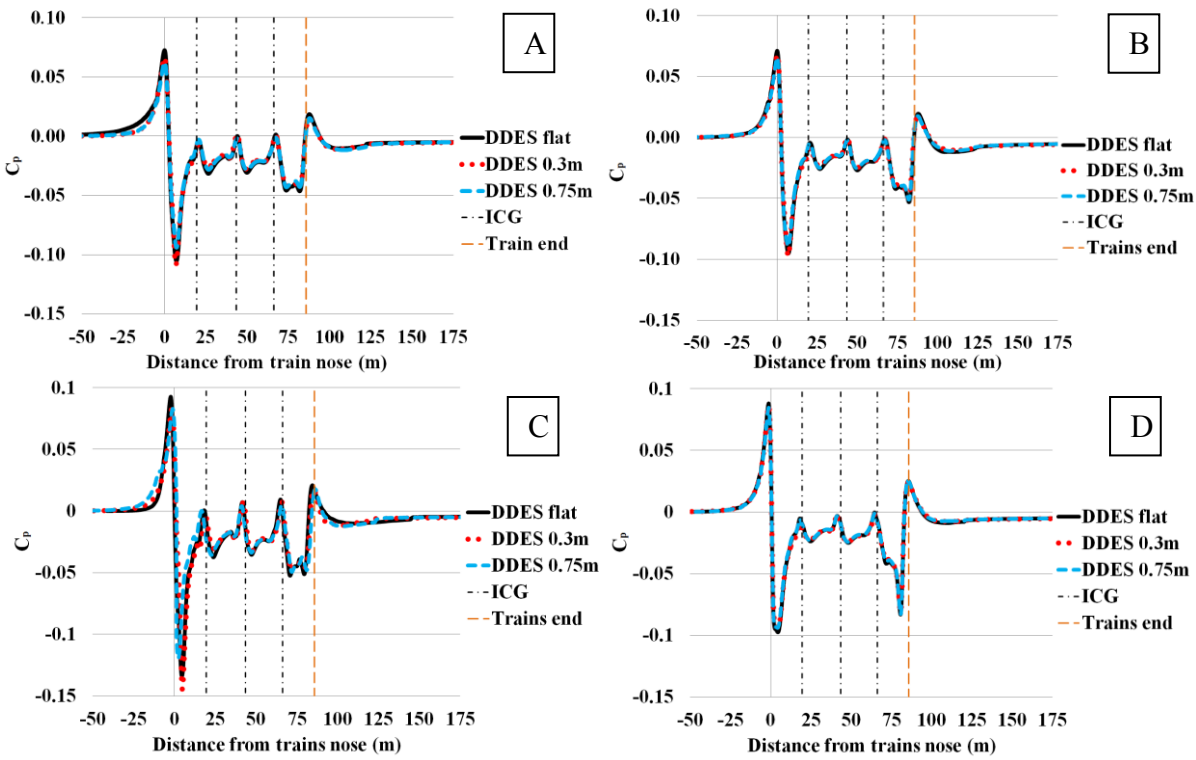

Figure 42: A-D: Pressure coefficients along the four specified measurement location at different ballast heights. A = 3m COT x 0.2M TOR. . B = 3m COT x 1.2M TOR. C = 2.5m COT x 0.2M TOR. D = 2.5m COT x 2.1M TOR.

Figure 42 A-D Shows the C_p values along each of the four measurement locations chosen. The results show that changes in ballast height cause little effect upon the pressure coefficients within the slipstream region of the train. A small difference can be seen in the head pressure pulse ahead of the train in the results of the measurement location situated at 2.5m from COT and 0.2m above TOR, here it can be seen that the ballast cases allow the

pressure to build up slightly earlier than on the flat ground case. This effect is due to the high pressure flow moving less in an outward direction than the flat ground case due to the ability for flow to also move down the ballast, thus resulting in a higher pressure region around the measurement point. This also explains why the flat ground case produced a slightly quicker pressure build up at 3m from COT by 0.2m from TOR measurement location. Furthermore due to this increased area to expand into the results at 2.5m from COT and 0.2m above TOR show the overall peaks of the pressure pulses to be lower than that of the flat ground case.

5.4. Comparison of velocity profiles

The final method used is to compare velocity contours upon planes that pass through the computational domain, these planes cut through the computational domain at an angle perpendicular to that of the free stream air flow. These planes show the differences that occur between the different ballast heights by comparing time averaged velocity contours at four measurement locations. The four measurement locations are situated at the midpoint of the second and third cars, 30m and 53m respectively, and within the wake region at 88.25m and 95.75m from the trains nose. These locations were chosen as these regions showed the largest variation between ballast heights in section 5.3.

The velocity contours are inverted as to represent a moving train rather than that of a stationary train in a moving flow, this was done to help with visualising the comparison between experimental and CFD results. Along with colour contouring by velocity the time averaged planes also feature streamlines to show the directions of flow. Unlike the velocity contours which show the resultant velocity of all three dimensions of the flow the streamlines only show the components parallel to the planes, this is necessary otherwise the flow

component parallel to the train would be too dominant therefore making the streamlines unclear.

By comparing the results over these planes, the reasons for notable differences between the trains slipstream at different ballast heights will be made visually clear. These streamlines will also provide an overview as to the form of flow structures within the slipstream which will provide insightful information for the crosswind work. Within each image the four measurement lines used in section 5.3 are marked by red dots, if these dots fall within regions of red (high velocity) then they are surrounded by a white ring. The inclusion of these measurement points allows for further comments to be made on the results of section 5.3.

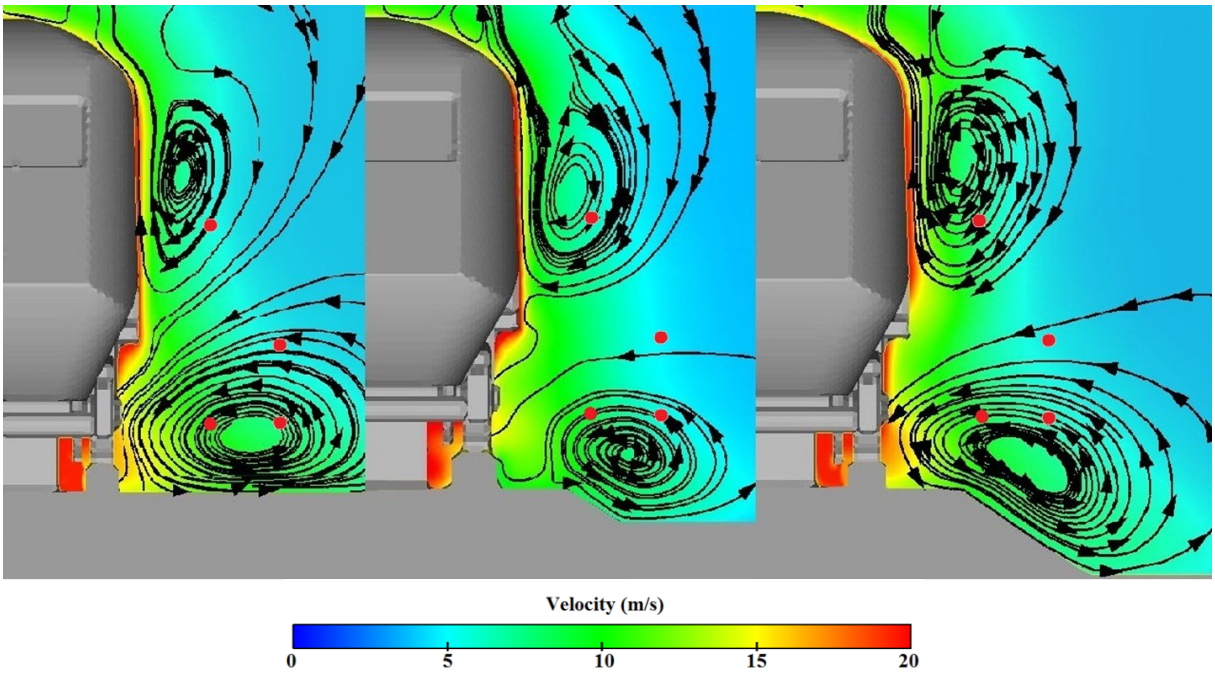

Figure 43: Time averaged velocities within the slipstream at midpoint of second car (30m from the front of the train).

Figure 43 shows the time averaged velocities within the slipstream along with the streamlines. The time averaged velocity contours at this location show that the accelerated flow that forms

the trains slipstream extends further out from the train near the ground level than at higher heights. This is to be expected due to the blockage between parts of the trains underbody and the ground creating more turbulent flow that is forced out sideways from the train. Two vortices form upon the side of the train, The higher vortex turns in a clockwise direction on the trains left side and is situated at around mid-train height. The second lower vortex rotates anti clockwise on the lower side of the train with the flow moving out from the train at ground level.

When ballast height is increased beyond a flat ground it can be seen that the high velocity air of the slipstream moves down the ballast side and away from the train, this effect is occurring as the lower vortex remains attached to the ballast surface and moves down the ballast side due to the Coandă effect. The 0.3m ballast can be seen to produce a narrower slipstream at ground level than the other two ballast heights, this is due to a reduction in the energy of the slipstream caused by the flow being forced to divert a second time by the positive gradient change where the ballast joins the lower ground. The 0.75m ballast height results show a similar effect with the slipstream not extending far along the lower ground plane but due to the longer slope side this is less evident.

Higher up the train side the ballast height can be seen to cause a small effect upon the size of the upper vortex and the cores location in each case. As the ballast height is increased it can be seen that the core moves away from each of the lower measurement points, moving the points towards the cores edge where velocities are lower. This accounts for the differences seen in section 5.3 along the second car.

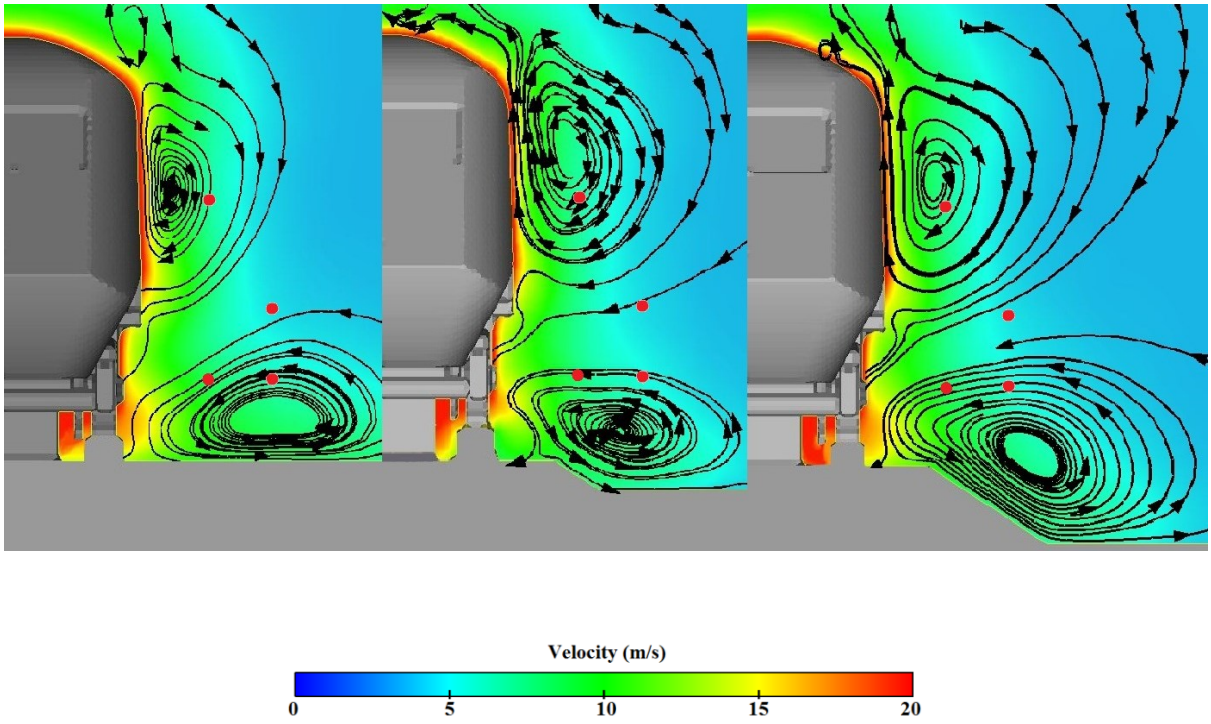

Figure 44: Time averaged velocities within the slipstream at midpoint of third car (53m from the front of the train).

Figure 44 shows the time average velocity at the midpoint of the third car. In comparison to Figure 43 it can be seen that the slipstream is slightly larger than at the second car. The underbody and near surface velocities are considerably higher, this is to be expected with the growth of the slipstream along the trains length seen in section 5.3. Along the second car the lower vortex moves down the ballast side increasing the core distance from the 0.2m height measurement points. For the flat ground case the 3m by 1.2m measurement location is within the range of flow affected by the lower vortex, however as ballast height is increased the measurement location becomes nearer to flow influenced by the upper side vortex.

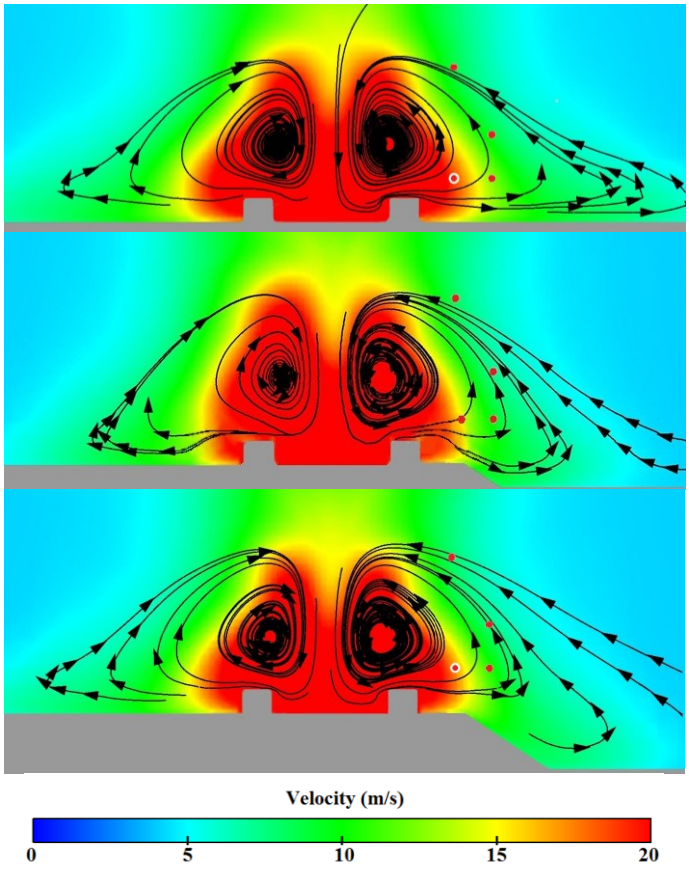

Figure 45: Time averaged velocities within the wake at 2.5m after the train (88.25m from the front of the train).

Figure 45 shows the wake velocity profile 2.5m after the trains tail (88.25m from the nose of the train) for each of the three ballast heights. In all three cases two counter rotating vortices are formed directly behind the train, with the central part of the flow between them having a downward motion. In the raised ballast cases the vortex seen at the bottom of the ballast in previous plane locations no longer exists. The two wake vortices cause flow to extend out from the wake centre along the ground of the ballast. This is because at this range behind the train the velocities within the wake are very high. For the 0.3m and 0.75m ballast height cases some of this flow travels down the ballast side until it reaches the lower ground level. Results also show that in cases with a ballast, the ballast side vortex draws in additional flow from the

free stream regions to the side of the vortex. The core locations of each of the vortices are constant through each of the ballast height cases at this location.

When comparing the location of the measurement locations to the wake it can be seen that in all three cases the 2.5m COT x 2.1m TOR location falls well outside of the high velocity regions and instead lies in a large lower velocity region. Due to this there is little variation between each of the ballast heights which matches the findings of Figure 41 this is also the reason for the small variation in results between the three cases at 3m COT x 0.2m TOR location. The 2.5m COT x 0.2m TOR location falls within the high velocity (red) region of flow within the wake for the flat ground case, whilst the two ballast height cases fall on the border of the high and low velocity regions. This causes the difference that can be seen in the wake of Figure 40. In the results of Figure 39 a large variation can be seen between the flat ground and ballast height cases for the 3m COT x 1.2m TOR location. From this plane it can be seen that the difference is caused due to the location being much closer to the high velocity flow of the flat ground case, whilst the measurement location within the 0.75m and particularly the 0.3m cases is near to the border between the wake and free stream flow.

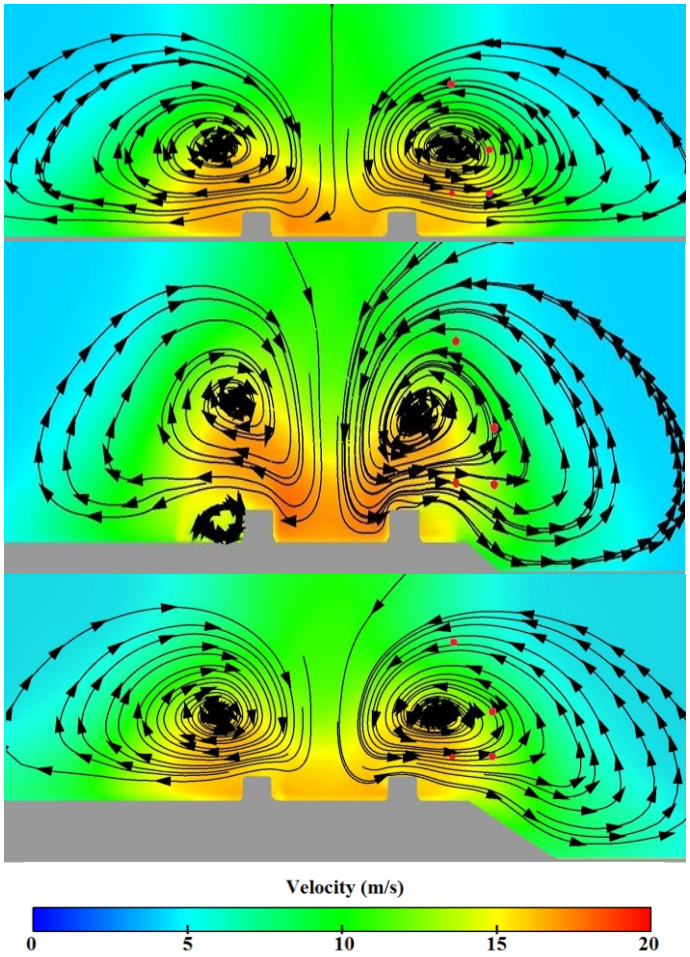

Figure 46: Time averaged velocities within the wake at 10m after train (95.75m from front of train).

Figure 46 shows the wake velocities and flow direction over a plane situated 10m into the trains wake (95.75m after the trains nose). Compared to the 2.5m wake results of Figure 45 the wake velocities within the central and higher parts of the wake are considerably lower. Two counter rotating vortices still exist but these are now situated further out from the trains centre. The vortices are now larger and more round in their shape. As with the results of Figure 45 the ballast can be seen to cause no significant effect upon the location of the vortex cores. In the raised ballast cases the vortices again extend down the ballast side due to the Coandă effect. Due to the vortices being situated further outward compared to the 2.5m results the vortex extends down the ballast sides and further along the lower ground level.

Due to the new vortex positions the 2.5m COT x 0.2m TOR measurement location is now situated within the wake region of high velocity for all three ballast heights. Both of the measurement locations situated 3m from the centre of rail are on the boarder of the high velocity region for the flat ground and 0.75m cases. For the 0.3m case the 3m COT measurement locations are situated more central in the lower velocity section of the wake whilst the 2.5m COT x 2.1m TOR measurement location is now situated above the vortex core. For the flat ground and 0.3m cases the 2.5m x 2.1m measurement point is inside of the low velocity region, for the 0.75 m case the point is above the wake due to the wake not extending as high up. This is the reason for the lower normalised wake velocities seen in Figure 41.

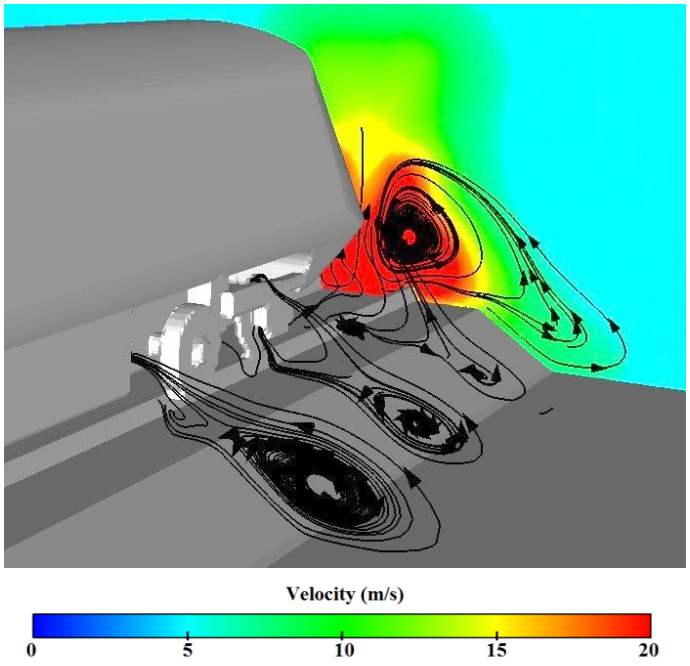

Figure 47: Slipstream vortex location for 0.75m ballast.

From the results of Figure 45 and Figure 46 it can be seen that the slipstream vortex noted along the side of the train no longer exists within the wake. Figure 47 shows the tail end of the train from the 0.75m ballast case with path lines to show the directions of rotation within the

vortex at this region. The path lines show how the slipstream vortex quickly dissipates at the end of the train before the two counter rotating vortices form within the wake. This occurs due to the large low pressure spike at the end of the train noted in Figure 42 drawing the majority of flow in towards the train, thus preventing enough flow to continue along the ballast surface and form a detached vortex. The tendency for the underbody region of the tail to produce an inward flow was also noted in the work of Quinn and Hayward (2008). This effect occurs in all three cases as all can be seen to produce a vortex along the trains side until the wake region.

From the results shown in this section it can be concluded that the ballast height difference does not cause the slipstream to diffuse any quicker despite the larger free stream area to expand into. Instead the slipstream moves down the ballast side due to the Coandă effect with more of it passing under the measurement locations used in section 5.3. It is due to this movement that velocity readings in section 5.3 reduce with ballast height.

5.5. Ballast height conclusion

The initial stage of this chapter was to validate the CFD approach against experimental data for each of the ballast heights, the aim of this was to determine if the difference in results produced by the two approaches increased as ballast height increased. The normalised velocity results from the flat ground geometry were found to be in best agreement to the experimental results, whilst the two ballast height cases featured larger differences between the two approaches. For the flat ground case around the nose velocity spike the DDES approach was able to accurately match the experimental results. Along the side of the train and at the tail velocity spike the DDES results showed an under prediction. Within the wake

of the train the DDES results produce a consistent over prediction of the velocity. Pressures throughout the measurement location show a trend to under predict the experimental results in all three geometries.

When comparing the CFD results for the different ballast heights against each other it can be seen that slipstream velocities are affected by ballast height, whilst ballast height causes little to no effect on pressures. As ballast height is increased the general trend is for the measured slipstream velocity to decrease. The magnitude of this effect reduces as distance from the train is increased, this is due to the slipstream velocities decreasing with distance from the train. At all measurement locations the results show a considerably smaller drop in velocities between the 0.3m and 0.75m ballasts than between the flat ground and 0.3m ballasts. Around the nose of the train the initial velocity spike and flow reversal spike show little to no variation at different ballast heights. The variation in results with ballast height occurs due to the high energy flow near the train remaining attached to the ballast side as it travels outward and down the sides of the ballast, this is confirmed by the results in section 5.4 where the flow is visualised along planes. The path lines clearly show how the slipstream of the train remains attached to the ballast side pulling it down, this results in a reduced velocity around the measurement locations in comparison to the flat ground case.

From the findings of this chapter it is possible to assume that a single sided ballast could cause an even larger effect on the slipstream of a train when situated upon to windward or leeward side during crosswind conditions. Furthermore as ballast height was increased the variance between both CFD and experimental results grew, therefor there is the potential that the same would be true for any crosswind case. For these reasons the crosswind work will be conducted upon a flat ground geometry.

Chapter 6. Validation of Crosswind results.

6.1. Validation introduction

The tests conducted by RWDI included yaw angle tests in 5^o increments up to 90^o. The setup used at RWDI is not directly comparable to the setup of the crosswind CFD cases due to the use of a STBR, lack of a launching geometry and the low Reynolds number ($1x10^5$) used for the RWDI tests, however the results will provide useful analysis as trends should remain similar between the two approaches. Comparisons are drawn using two approaches. Firstly aerodynamic drag, lift and side forces for the first car are compared to the crosswind CFD results. Secondly surface pressure results are compared around the five loops previously used in chapter 3 and also over three pressure taps situated upon the train's nose.

6.2. Aerodynamic forces

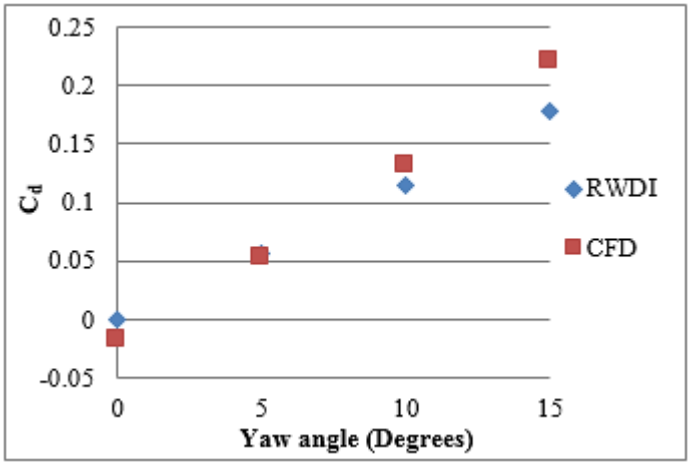

Figure 48: Change in C_d value against yaw angle for RWDI and CFD results.

Figure 48 shows the first car C_d values recorded during the RWDI testing and the C_d values recorded from the CFD simulations for the four yaw angles investigated. The no crosswind results show that the RWDI experiment produces a larger C_d value, this is due to differences within the firing geometry as differences were not seen within the results of chapter 4. At yaw angles of 5^o the C_d measurements are closer, this is due to the differences within the launch mechanism being less prominent as the yaw angle increases due to sheltering by the bogies. Both the 10^o and 15^o results show larger C_d values recorded within the CFD tests. The larger results from the CFD investigations are due to the DDES approach over predicting the separation that occurs over the roof region, this effect can be seen in section 6.3.

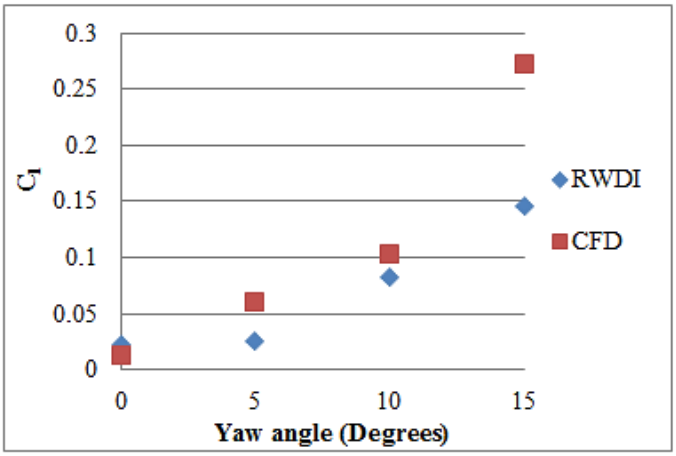

Figure 49: Change in C_l value against yaw angle for RWDI and CFD results.

Figure 49 shows the RWDI and CFD first car C_l values for each of the four yaw angles investigated. The results of chapter 4 showed that the lack of pressure taps within the underbody of the RWDI model led to pressure features being missed, therefore the results of this comparison should be taken with caution. At 0^o the RWDI results feature a C_l of over twice the CFD results though this value itself is only small. The CFD results for the 5^o yaw

angle calculate a 50% larger lift force than that of the RWDI tests. At 10° the difference between the two C_l values reduces to 20%. The C_l value at 15° is nearly twice that of the experimental results. The large difference at this yaw angle is due to an over prediction of flow separation over the roof and the addition of the firing carriage under the CFD model causing a rise in the underbody pressures.

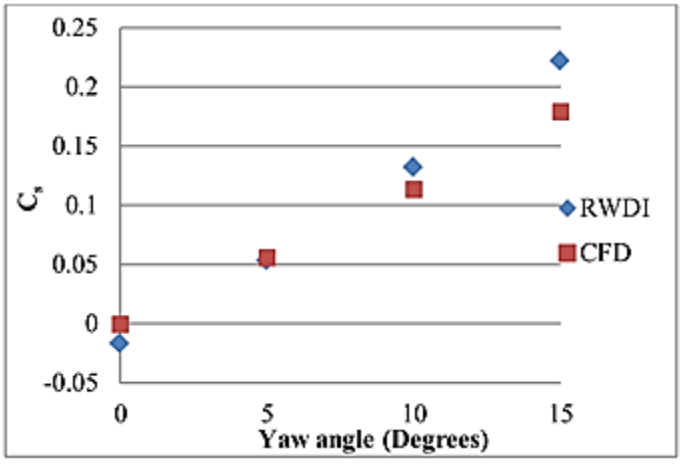

Figure 50: Change in C_s value against yaw angle for RWDI and CFD results.

Figure 50 shows the comparison of Side force Coefficient (C_s) values obtained in both the RWDI wind tunnel test and the results obtained from the CFD simulations. It can be seen that both of the approaches show a near linear relationship between the increases in side force and yaw angle. The RWDI results predict a sharper rise in the C_s value with yaw angle and at 10° and 15° predict higher C_s values, this is not what would be expected with the underbody geometry not being included in the calculation of the experimental coefficient. This suggests that the CFD results predict a lower pressure differential between the windward and leeward sides. From the comparison of the aerodynamic forces it can be seen that in general good correlation exists between the two approaches, particularly at the smaller yaw angles.

6.3. Surface pressure loops

The following section compares surface pressure coefficient values obtained using CFD to those recorded during the RWDI tests, pressures were compared over the same loops as used in chapter 4, these loops can be seen in Figure 26. Figure 51 right shows the location of corner markers and their corresponding abbreviations as used within the graphs of this chapter, these are used to give a clearer understanding of the locations of pressure features around the train. Measurements are at full scale with 0m representing Top Dead Centre (TDC), for loops four and five the front edges of the train are abbreviated to LW edge and WW edge representing leeward edge and windward edge respectively.

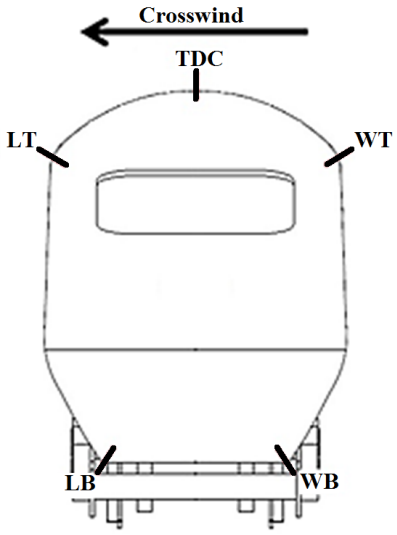

Figure 51: Corner marker locations and abbreviations.

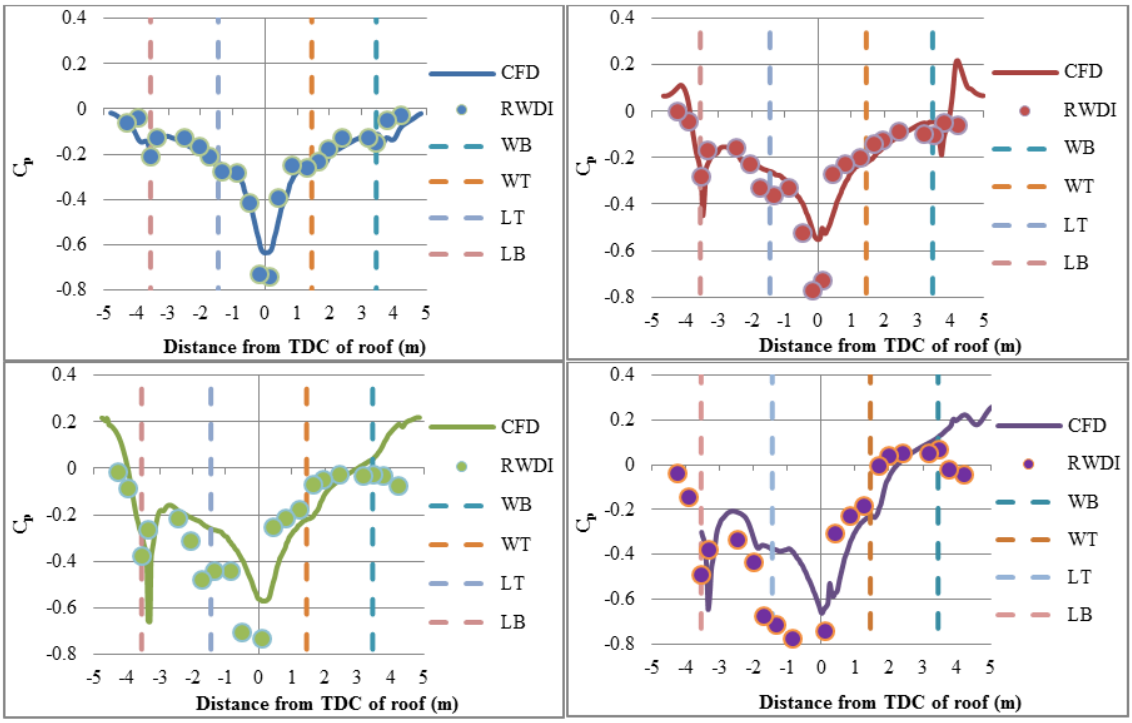

Figure 52: RWDI and CFD plots for Cp around loop 1. Top left: 0°, top right: 5°, bottom left: 10°, bottom right 15°.

Figure 52 shows a comparison between the CFD and RWDI results around loop one, results are shown for each of the four yaw angles individually. Results for the no crosswind case show high correlation between the two methods though the CFD results predict a lower C_p over the trains roof (0m) this matches the findings of chapter 4 where the DDES approach was shown to under predict the roof peak. At a yaw angle of 5° there is still good correlation between the two approaches though now an additional difference begins to occur upon the windward side of the roof at around 1m, at this location the RWDI results show a higher C_p value than recorded in the CFD. The results for 10° and 15° show larger differences between the two approaches upon the leeward side, the CFD results predict C_p values around half that recorded in the RWDI tests. These differences could be due to the different ground geometry

or the different Reynolds number between the two approaches. Despite the magnitude differences both the 10° and 15° results show similar C_p profiles around the train.

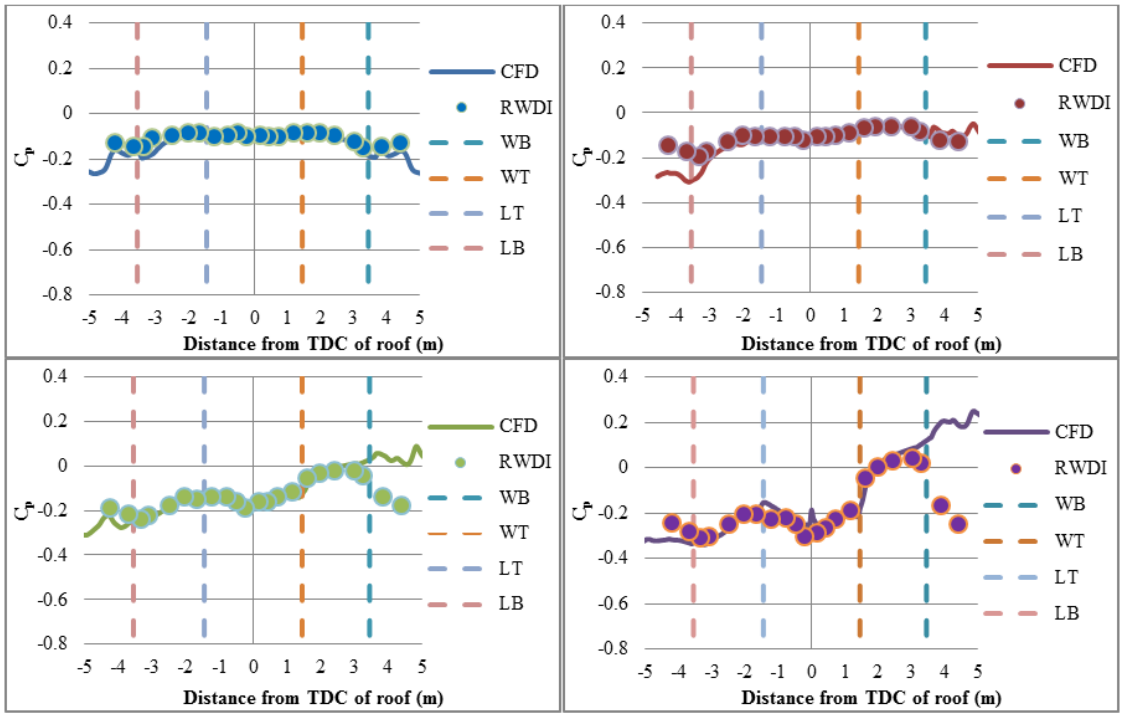

Figure 53: RWDI and CFD plots for Cp around loop 2. Top left: 0°, top right: 5°, bottom left: 10°, bottom right 15°.

Figure 53 shows the C_p results around loop location two, around this measurement loop the fluctuations in C_p are smaller than at loop location one. There are also no sharp changes or significant peaks in pressure. At this measurement location the CFD results for all four yaw angles match closely with those recorded during the RWDI tests. At 10° and 15° the windward side of the underbody region shows the C_p rising with distance from the edge in the CFD results and dropping with distance in the RWDI results, this difference is caused by the CFD geometry including a firing mechanism and box section frame as used at the TRAIN facility.

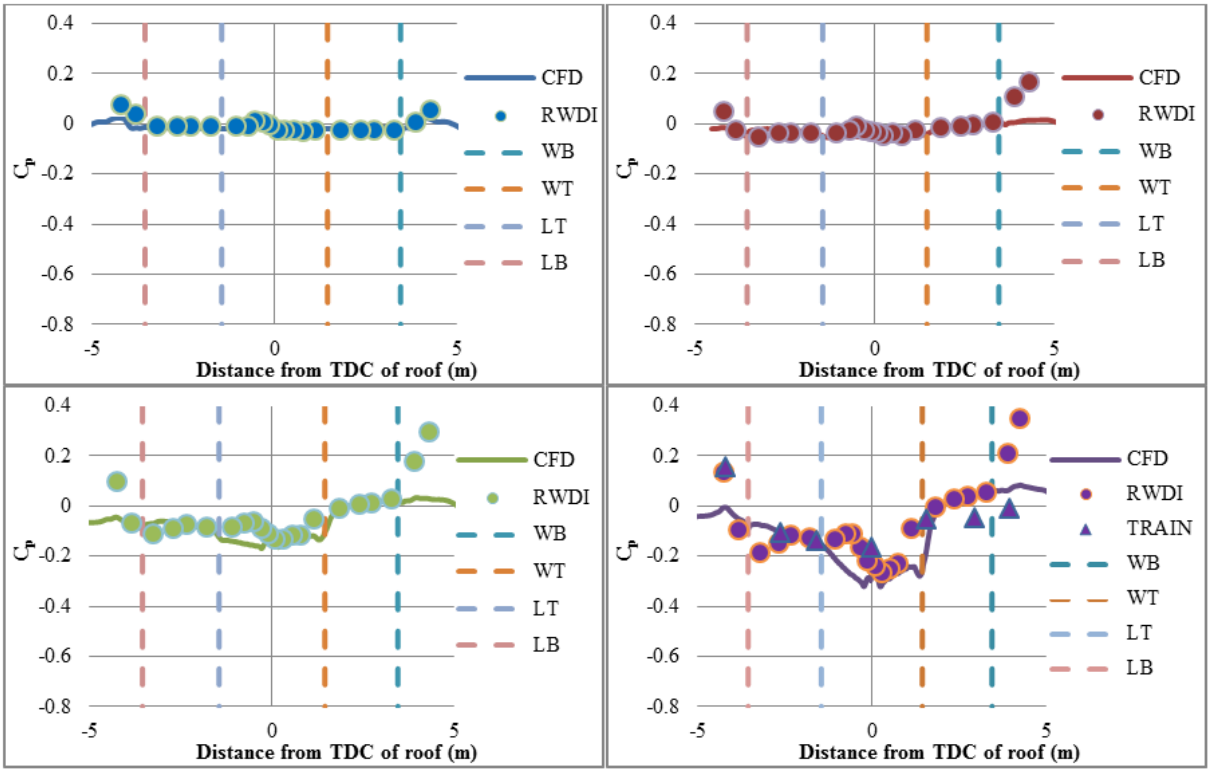

Figure 54: RWDI and CFD plots for Cp around loop 3. Top left: 0°, top right: 5°, bottom left: 10°, bottom right 15°.

Figure 54 Shows loop location three, this loop is situated towards the end of the first car. The 15° yaw angle results at this location also include measurements recorded at the TRAIN facility by fellow researchers at the University of Birmingham. Both the 0° and 5° results show high levels of correlation between the two different approaches. At 10° differences begin to occur between the two approaches on the windward edge and the leeward side of the roof. These differences also occur to a larger magnitude at a yaw angle of 15°. At both of these roof regions the CFD results predict larger C_p values than measured during the RWDI and TRAIN tests. The difference to the RWDI results is likely due to an over prediction of the amount flow separates over the roof. Only seven measurement locations were recorded during the TRAIN facility tests, of these seven only three of these locations correlate well with both the CFD and RWDI results. From the remaining four taps the two upon the windward side

predict a larger negative pressure. The measurement locations at the centre of the train and upon the leeward underside both match the RWDI results closer than the CFD results.

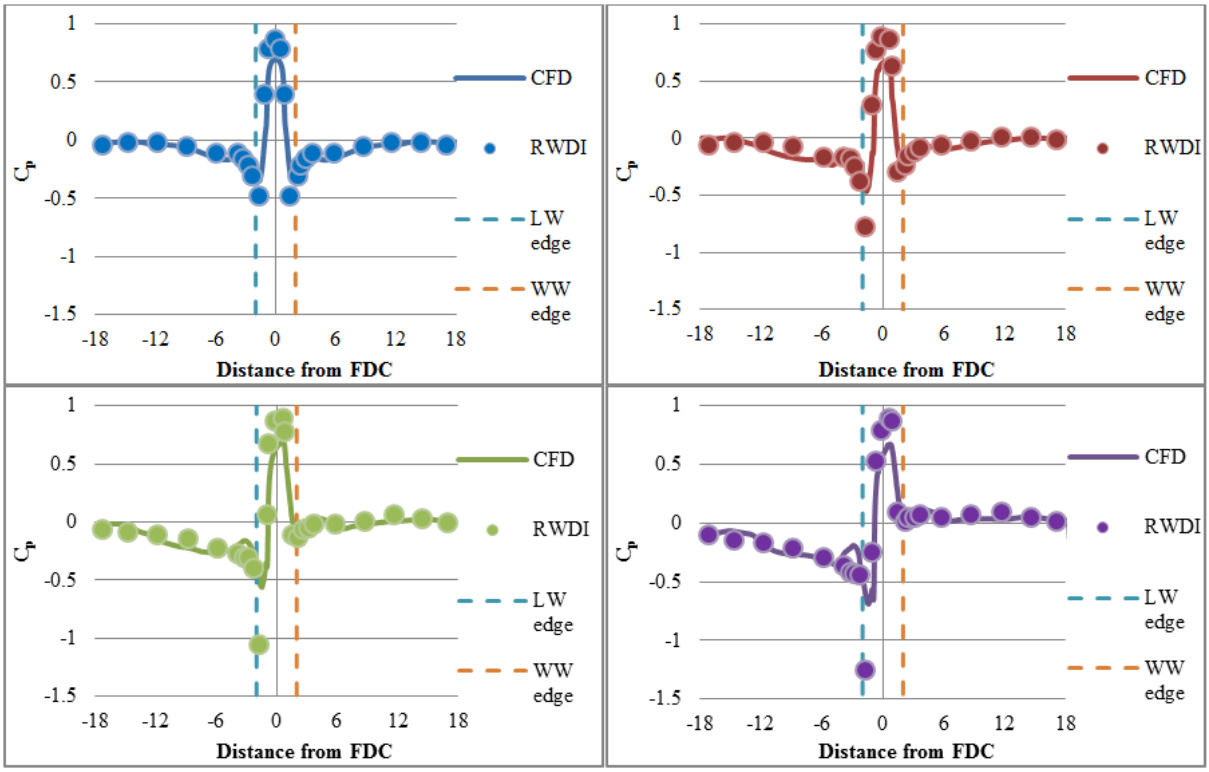

Figure 55: RWDI and CFD plots for Cp around loop 4. Top left: 0°, top right: 5°, bottom left: 10°, bottom right 15°.

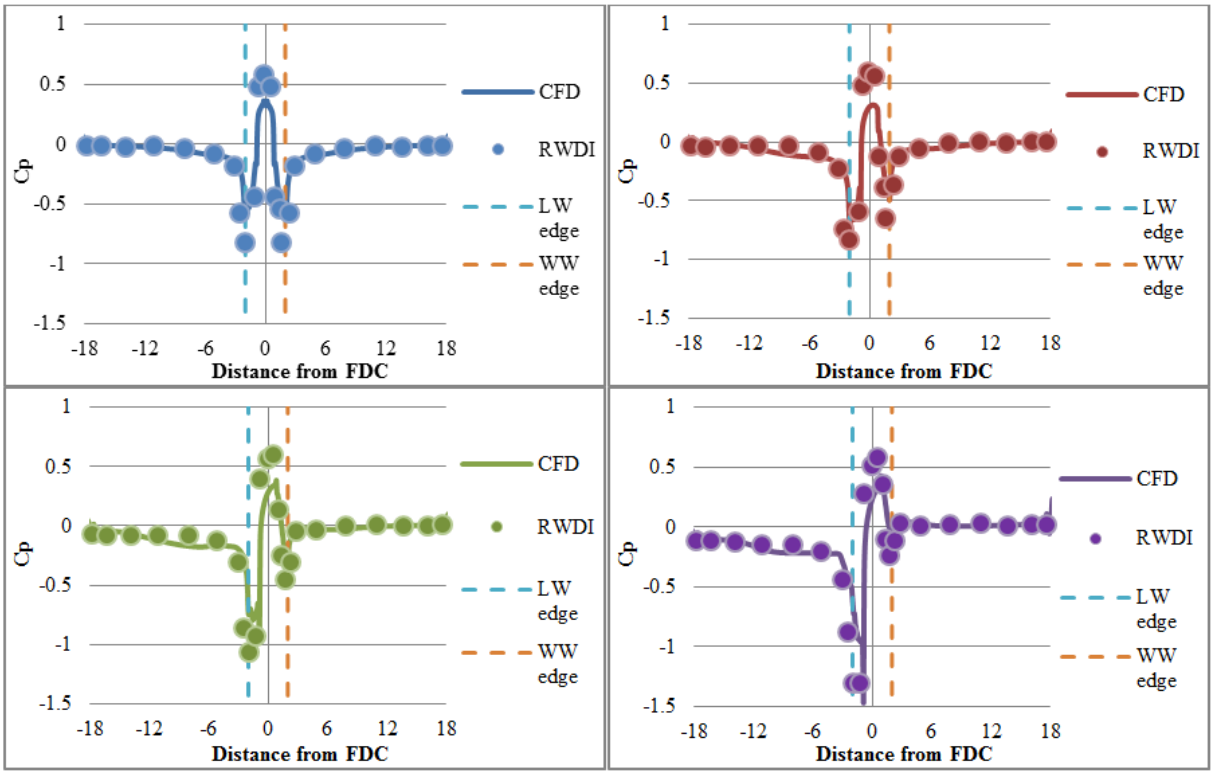

Figure 56: RWDI and CFD plots for C_p around loop 5. Top left: 0^o, top right: 5^o, bottom left: 10^o, bottom right 15^o.

Figure 55 and Figure 56 show the Cp results around loops four and five for each of the four yaw angles investigated. For both loop locations the CFD results predict lower pressures upon the front of the train, this is a result of the STBR diverting more flow towards the nose in the RWDI tests. Except for the nose region loop four shows good correlation at all but the leeward edge at the higher yaw angles of 10^o and 15^o. Around loop five the C_p profiles between the two approaches show a higher level of correlation than loop four, excluding the nose the only significant difference occurs upon the leeward edge in the 10^o results.

6.4. Comparison of CFD results to experimental measurements using quality assessment methods.

Using the same methods of quality assessment as used in chapter 4, the surface pressure coefficients from section 6.3 from all five loops were analysed against the experimental results collected at RWDI, once again plus and minus one standard deviation was taken to be the margin of uncertainty. Should a perfect match exist the results would match the "ideal" value presented within the table, the analysis results can be seen in Table 7.

The analysis of the results using the q method show that the accuracy of the CFD approach when predicting surface pressures decreases as yaw angle increases. The factor 2 results also show this, however as the scores are higher in all three yaw angle cases it shows that the main areas of variation are likely within the high pressure range regions, this can be determined as the high pressure regions feature a higher range within which results will count as accurate whereas the range remains constant within the q approach (+/- 1SD). This assumption matches the graphs in section 6.3 where the large differences can be seen to be mainly around peaks.

Though useful these approaches need to be used with caution, this is particularly evident in the FB approach. Results for the FB approach show that the CFD results over predict pressure coefficients, however the FB approach also calculates the 15^{o} yaw angle to be more closely matched to the experimental results than the 10^{o} case. This contradicts the other two methods of quality assessment and from the graphs in section 6.3 would appear incorrect. This occurs due to some large under predictions primarily around the underbody at loops one and two cancelling out over predictions elsewhere.

Table 7: Comparison table showing summary of crosswind CFD analysis using quality assessment approaches.

	Ideal	CFD 0°	CFD 5°	CFD 10°	CFD 15°
q	1	0.86	0.83	0.81	0.77
FB	0	-0.79	-0.85	-1.03	-0.89
Factor 2	1	0.86	0.84	0.83	0.81

6.5. Nose pressure

In addition to the five loops used in the previous section, C_p values were also recorded at measurement locations at the front of the train's nose. Results were recorded for the RWDI and CFD results at 0^o through to 15^o in 5^o increments whilst results from the TRAIN facility were only available for 15^o. The location of these taps can be seen below in Figure 57.

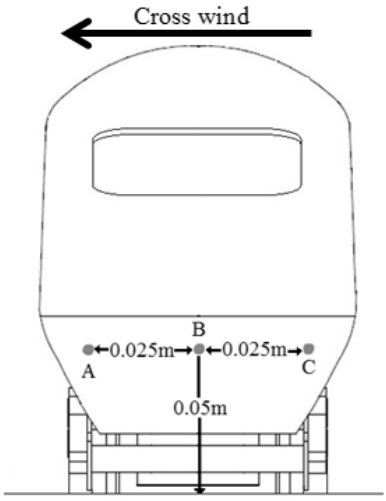

Figure 57: Nose measurement locations (model scale)

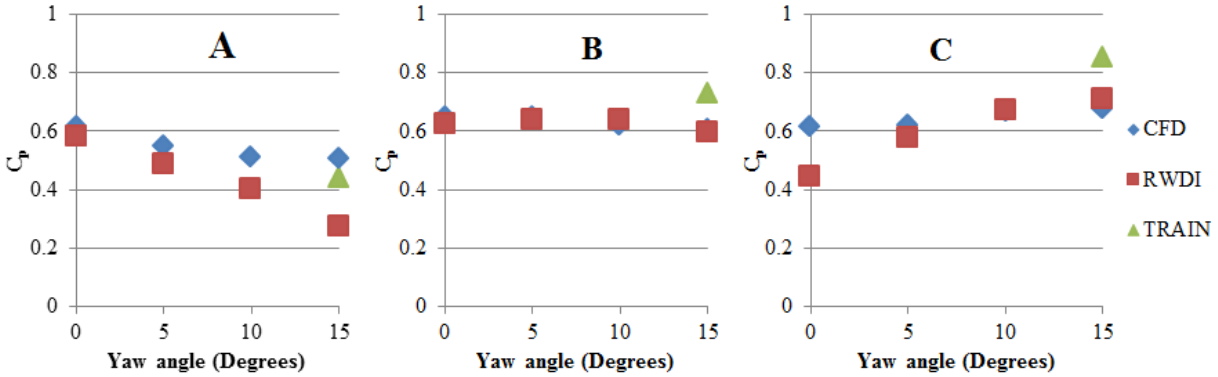

Figure 58: Changes in C_p with yaw angle for each of the three measurement taps shown in Figure 57.

Figure 58 shows the variation in C_p values recorded as yaw angle is increased. Graph A shows the leeward side tap, at this tap location results from both the RWDI and CFD approaches show the C_p dropping as yaw angle increases. The CFD results show the rate at which the C_p drops decreases with each additional yaw angle increase whilst the RWDI show the rate slightly increases. At 15^o this difference in profiles leads to a large variation between results, The TRAIN facility results at 15^o match more closely with the CFD results. At the central measurement point (graph B) the CFD and RWDI results produce near identical results at all yaw angles whilst the TRAIN test result is at a higher C_p value. Graph C shows the windward tap location results at yaw angles 0^o and 5^o the RWDI results are lower than the CFD results but rising with yaw angle, at 10^o the two approaches record a near identical value whilst at 15^o the RWDI C_p is slightly higher. The result from the TRAIN test is higher than both approaches by a similar amount again. The RWDI results for 0^o yaw angle at this location do not match those of graph A despite them being in symmetrical locations. This suggests there is an error in at least one of the two readings.

6.6. RWDI comparison conclusion

From the comparisons of aerodynamic forces within this chapter it can be seen that the results for the drag force shows higher levels of correlation than that of the lift force, this is likely due to the lack of pressure taps situated within the underbody of the RWDI model causing key pressure features to be missed. The side forces of the train were noted for being unexpectedly lower within the CFD results than within the experimental results. Surface pressure results later in the chapter showed that this was due to different predictions in the C_p values upon the sides of the train.

Comparisons over pressure tap loops showed mixed levels of correlation, the main areas where large differences occurred were regions of rapid pressure change such as the leading edges of the roof and leeward sides, and regions with a negative pressure gradient such as the forward half of windward side of the roof. Good correlation between the approaches was obtained upon regions where the pressures were nearer to atmospheric and the second half of the roof. The use of quality assessment approach confirmed the accuracy of the CFD results was primarily dependent upon the pressures within the area, as the higher yaw angles featured larger pressure ranges it lead to a decrease in accuracy.

The measurements taken at the TRAIN facility match well with the CFD results upon the sides of the train but do not match over the centre of the roof, at the front of the train the TRAIN test measurements are constantly higher than the RWDI measurements and higher than the CFD results at both the central and windward taps. The overall conclusion of this chapter is the CFD results are able to accurately predict the pressure over the trains surface at most locations, at the locations that don't match well the CFD results still predict the correct profile trends.

Chapter 7. Effects of Crosswinds on the slipstream of a passenger train.

7.1. Introduction

The research within this chapter examines the slipstream around the class 43 HST when exposed to crosswinds of 0^o, 5^o, 10^o and 15^o yaw angles. Comparisons are made between each of the yaw angle cases using three different approaches. Using three different approaches will enable correct and detailed explanations to be given for the changes in flow features noted. The first approach used is the plotting of time averaged pressures and velocity fields around the train as iso-surfaces. This approach though lacking in finer detail provides an overview of the flow regimes around the train as a whole that can be built upon by the later approaches.

Secondly the flow regimes are compared around the train through the use of cross sectional planes that are colour contoured by the time averaged normalised velocity and C_p values. These are used in two stages, firstly the whole train is once again examined via this approach using a vertical plane through the train/domains length and through a horizontal plane situated 0.2m above the TOR. Using the results of the iso-surfaces and the whole train planes to decide upon locations the second set of planes cut vertically through the domains width, upon these planes streamlines showing the directions of travel within the flow are plotted. The streamlines show the two components of the flow parallel to that of the plane, this approach was chosen as the component running parallel to that of the train would over weigh the other two making flow patterns less clear.

Finally comparisons are conducted using quantative values from measurement lines along the length of the computational domain at four locations. The measurement locations used are 3m

from the COT by 0.2m above TOR as this is a key TSI location for slipstream measurement and 3m from COT by 3m above TOR. The secondary location was chosen as results at the start of this chapter show the roof region to be one of the main areas that crosswinds affect. Each of these locations is situated on both the windward and leeward side of the train.

7.2. Overview of crosswind effects.

In order to provide an initial understanding of how crosswinds affect the slipstream around high-speed passenger trains this section focuses on visualising the flow fields around the train as a whole. From this overview key areas can then be selected for further investigation during the remaining sections of this chapter. Two approaches are used to visualise the flow, first iso-surfaces of both the time averaged velocity and pressure are produced to provide a 3D view of the larger structures. Secondly 2D planes are used, these planes cut vertically and horizontally through the domain and are colour contoured by either pressure or velocity to provide a clearer view inside the slipstream.

7.2.1. 3D Iso-surfaces

In this section flow structures are analysed through the use of iso-surfaces, these surfaces produce a 3D representation of the pressure and velocity fields around the train. Pressures fields are visualised at a coefficient value of -0.075 which equates to around -100 Pa. This pressure value was chosen by analysing the results of Chapter 4 with the aim of determining a value which would exclude the smaller pressure features along the train side but still clearly show the key features. The velocity field is visualised at a normalised value of 0.25 which is approximately 10 m/s but varies by around 1 m/s depending upon the yaw angle. This value

was again based off of the findings of chapter 4 with the aim of providing a clear visualisation of all key flow features. The iso-surfaces are coloured by the time averaged Q-criterion value (Hunt et al. (1988)) to show how turbulent the flow within these features is.

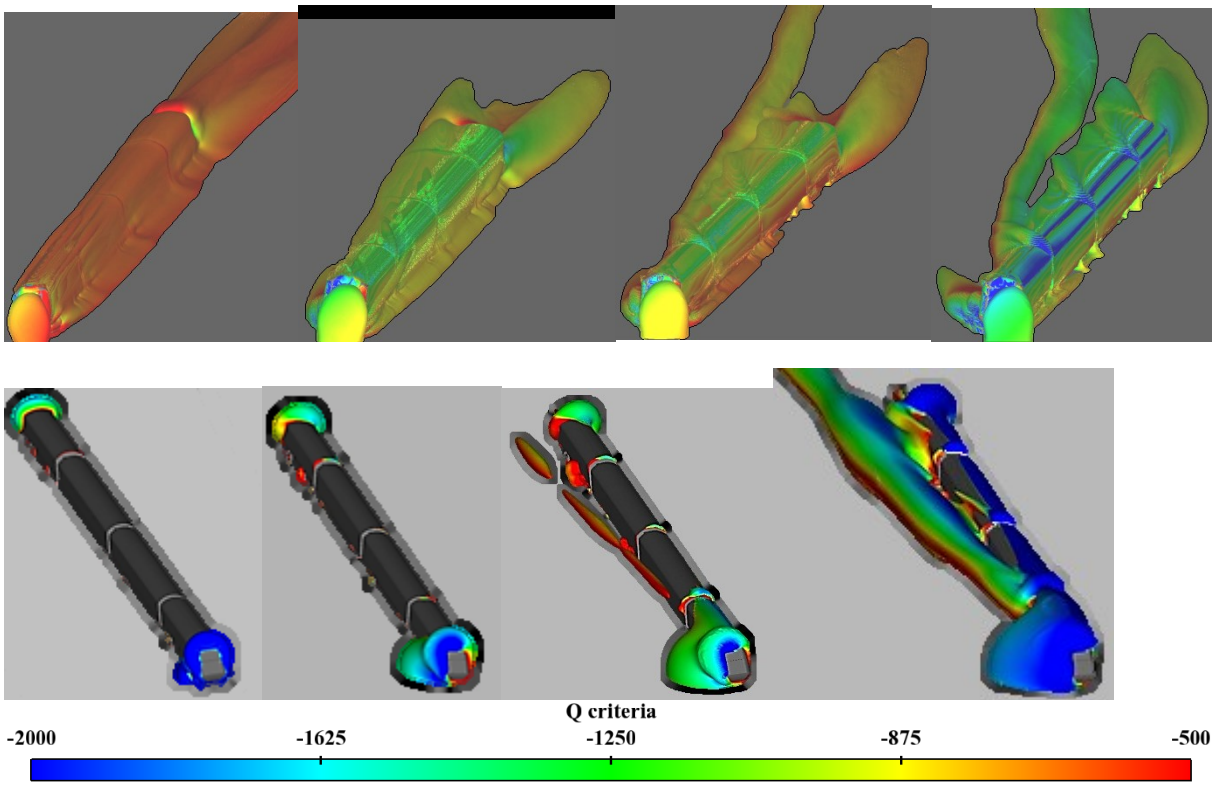

Figure 59: Iso-surfaces of normalised velocity magnitude above 0.25 (top row) and C_p values below -0.075 (bottom row) around the whole train for yaw angle 0^o, 5^o, 10^o and 15^o. Colour contoured by Q-criterion range shown at bottom.

Figure 59 shows Iso-surfaces of both mean pressure and mean velocity magnitude around the train. The pressure iso-surfaces show regions where the pressure coefficient is below -0.075 C_p whilst the velocity iso-surfaces show regions with a normalised velocity above 0.25. Around the nose region the pressure iso-surfaces show that as the yaw angle is increased the low pressure region around the edges of the trains nose increase in size and move towards the

leeward side of the train. The high velocity region ahead of the nose in the no crosswind case moves to the windward side of the trains nose as yaw angle is increased.

The growth of the low pressure region on the leeward side is due to flow separating and accelerating around the nose of the train and the underbody geometry. Flow coming over the roof of the first car at the higher yaw angles separates due to the negative gradient resulting in a low pressure region, this low pressure region joins with the low pressure region on the leeward side resulting in one large region.

As the yaw angle is increased a vortex sheds from the top leeward edge of the roof, at the normalised velocity value of 0.25 used for visualisation this shed vortex first becomes visible at 10^{o} whilst the 5^{o} results show the vortex attached to the side of the train. The pressure iso-surface shows the low pressure regions created by the shed vortex. At a yaw angle of 10^{o} the pressure iso-surface is small and broken, due to the high Q value it can be determined that this region is near the vortex core. At 15^{o} the low pressure region is considerably larger, this is due to the low pressure created by the flow accelerating over the roof. Due to the low pressure created by the roof the large majority of this low pressure iso-surface is situated above the vortex core, this can be determined from the variation of the Q value where the highly turbulent flow is at the lower edge.

At the tail of the train and within the wake the increase in yaw angle causes the wake to curve in a leeward direction, this effect becomes more evident at higher yaw angles where the crosswind velocity is higher. The low pressure regions around the tail of the train move to the windward side of the train, this is due to the increased amount of flow separating over the adverse gradient around the cars trailing edges.

7.2.2. 2D Cross section

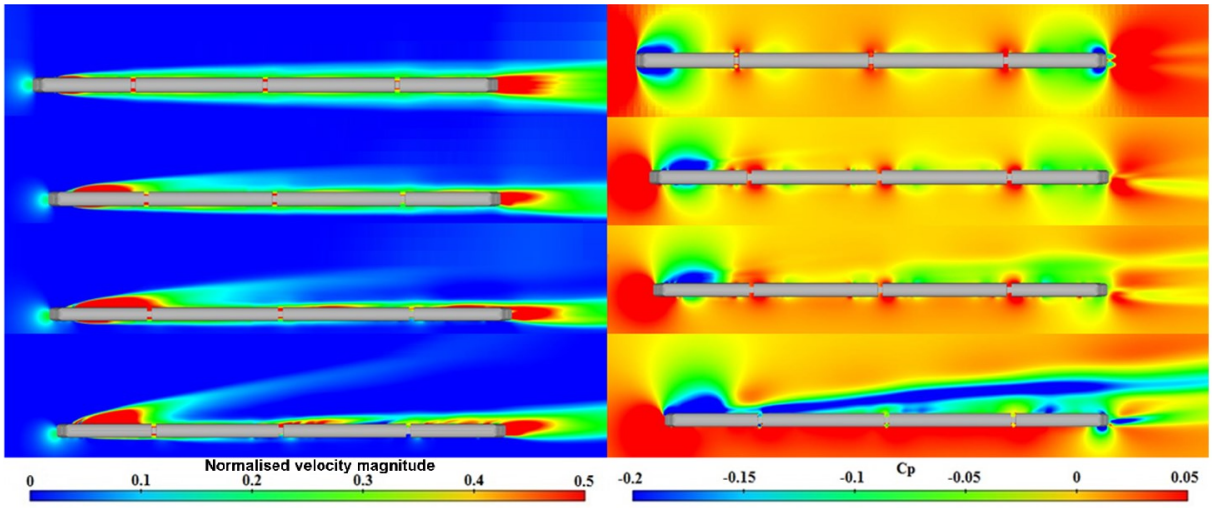

Figure 60: 2D cross-section of computational domain at 0.2m above TOR for each of the four yaw angles investigated, colour contoured by normalised velocity magnitude (left) and C_p (right).

Figure 60 shows a cross section through the domain at a height of 0.2m above TOR for each of the four yaw angles, two planes were produced for each yaw angle and colour contoured by normalised velocity magnitude and pressure coefficient. Around the nose of the train the pressure contours show that the high pressure region in front of the train moves to the windward side as yaw angle is increased, the high velocity region also moves to the windward side as yaw angle is increased as in section 7.2.1. Around the leeward side of the first bogie and the launching mechanism the results at all three yaw angles show large regions of low pressure, in the no crosswind case this region exist on both side of the train but nearer to the front. This difference is due to the increased amount of flow passing directly under the train in the no crosswind case. In the crosswind cases this low pressure region does not vary greatly between the 5^o and 15^o yaw angles, this suggests the complex underbody geometry is less sensitive to variations in yaw angle. The velocities within the same region show large

variations with yaw angle, between 5° and 10° the high velocity magnitude region grows in both width and length. As the yaw angle is increased up to 15° the flow moves further out into the free stream region but does not travel as far along the train.

Along the remainder of the trains length the pressure results show that as yaw angle is increased there is an increase in pressure to the windward side. On the leeward side there is a decrease in pressure that is created by the shed vortex higher up the trains side. Velocities on the windward side decrease as yaw angle is increased, this is due to the impinging flow suppressing any pulses from the underbody geometry and preventing the build-up of a deep boundary layer. The leeward side shows an increase in the very high velocity regions close to the trains surface with accelerated flow coming from the ICG's and bogies, these high velocity regions cause little effect on the overall growth of the boundary layer in the results of chapter 7.4. Results around the wake region show that as yaw angle is increased the width of the wake decreases, this is due to the windward side of the wake getting pushed to the leeward side by the oncoming flow. Pressure results within the wake show a more significant change with yaw angle. As yaw angle increases pressure within the wake begins to decrease, this is due to the vortex nearest the windward side of the train moving down and towards the leeward side of the train.

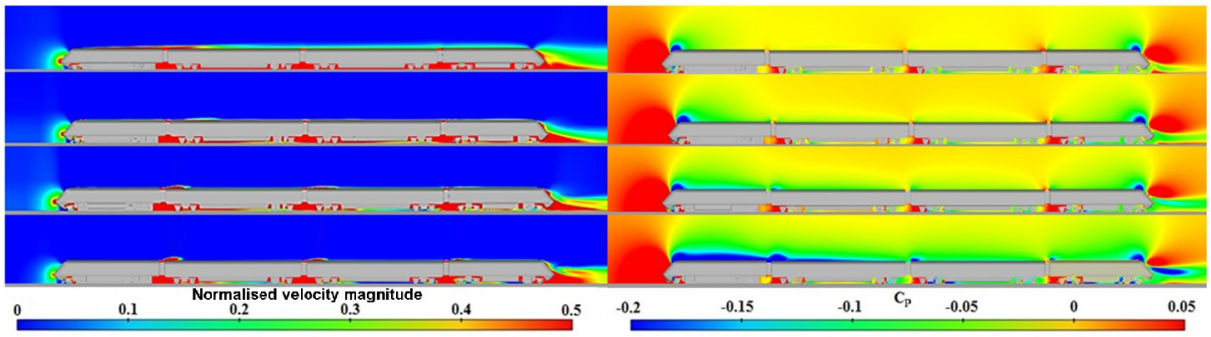

Figure 61: 2D cross-section through computational domain at COT for each of the four yaw angles investigated, colour contoured by normalised velocity magnitude and C_p as labelled.

Figure 61 shows the normalised velocity magnitude and pressure coefficient contours down the centre line of the train for each of the four yaw angles investigated. The results show that changes in yaw angle cause little effect on the pressures and velocities directly ahead of the train centre. The pressure over the roof of the leading car can be seen to gradually decrease with yaw angle until between 10^{o} and 15^{o} yaw angles where a large drop in pressure occurs, this large drop in pressure occurs due to flow passing and separating over the roof region as seen in section 7.2.1. The increase in yaw angle causes the build-up of a boundary layer seen in the no crosswind case to no longer occur as the flow is moved across the roof.

As yaw angle is increased the ICG's produce an increased effect on both the pressures and velocities over the roof. At higher yaw angles the flow is no longer moving straight along the roof, this causes more flow to encounter the leading edge of the following car. The blunt shape of this leading edge causes the flow to separate resulting in a momentary drop in pressure and increase in the flow velocity. Within the underbody the increase in yaw angle results in a reduction of velocity and an increase in pressure, this is due to the flow that is drawn along by the bogies being disturbed by the crosswind flow. Within the wake region the increase in yaw angle causes a minimal effect upon the velocities along the centre line. Yaw angle causes a more noticeable effect upon the wake pressures, with an increase in yaw angle causing an increase in the size of the low pressure region. This increase in size at this location is due to the windward side vortex being moved nearer/through the centre line of the train.

7.2.3. Whole train overview summary

Results within this section show that as yaw angle is increased there are significant changes to the shape of the trains slipstream. As yaw angle is increased there is a decrease in the velocity on the windward side of the train, this effect is most notable near the ground level where turbulent flow is released from the underbody region. On the leeward side of the train the results show that an increase in crosswind angle results in an increase in the slipstreams size, further more as the yaw angle was increased to 10^{o} and above a large vortex could be seen to form and separate from the trains slipstream. Pressure results show that as yaw angle is increased the leeward side of the train experiences a decrease in pressures particularly around the leading edge of the nose and first bogie. As the yaw angle is increased to 15^{o} large regions of low pressure also form over the roof of the train.

7.3. Detailed cross sections

To expand upon the results given in section 7.2 this section focuses upon the use of 2D planes cutting through the computational domain perpendicular to that of the trains travel, the planes cut through the domain at various locations along the trains length based upon the results of section 7.2. Each plane shows the time averaged C_p and normalised velocity magnitude, the planes contoured by the normalised velocity magnitude also feature streamlines to show the directions of flow using only the flow components parallel to the plane.

7.3.1. Nose region

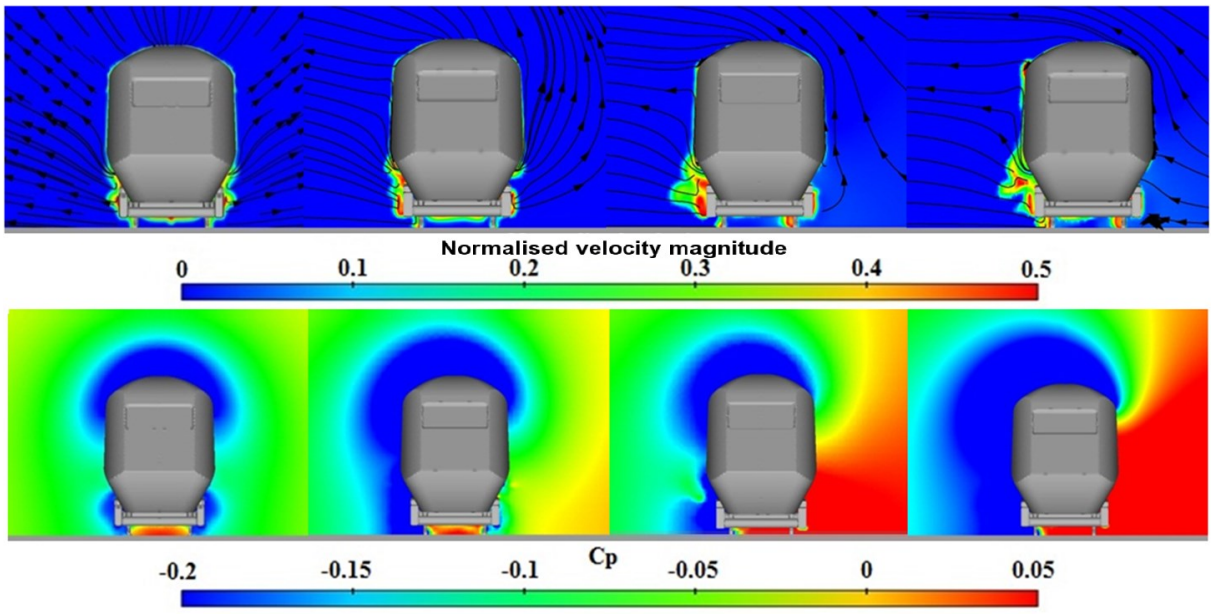

Figure 62: 2D cross-section through computational domain at 2.5m after trains nose for each of the four yaw angles investigated, colour contoured by normalised velocity magnitude (top row) and C_p (bottom row).

Figure 62 shows a cross section through the domain at 2.5m from the nose of the train, results for both normalised velocity magnitude and pressure coefficient are shown for each of the four yaw angles investigated. This plane is situated after the high velocity and pressure region ahead of the nose and prior to the large high velocity and pressure region seen just after the first bogie in Figure 60. At this location the velocity results show only a small variation with yaw angle. As the yaw angle is increased the region of high velocity flow created by the first bogie grows on the leeward side of the train.

On the windward side of the train there is a reduction in the size of this accelerated flow region as yaw angle grows, at a yaw angle of 15^o the region size is reduced to just a small boundary layer. Streamline results for the 0^o and 5^o yaw angles show the flow on the leeward side of the train move away from the trains surface, whilst the 10^o and 15^o results show the

flow to move away for the top half of the train and towards for the bottom half of the train. This effect at 10^o and 15^o shows that a large region of low velocity recirculation exists due to flow coming over the roof region and separating.

At a yaw angle of 5^o the streamlines show that flow on the windward side of the train moves away from the trains surface and upwards over the roof. At 10^o flow moves out and up from the trains side in a region near to the train, further from the train flow is moving towards and up over the train due to the oncoming flow. The results for 15^o show that all of the flow is coming into the windward side of the train with no flow moving back towards the oncoming flow. As a result of the oncoming flow in the 10^o and 15^o cases it can be seen from Figure 62 that a region of high pressure exists upon the windward side of the train. The pressure results also show that at a yaw angle of 5^o and above a region of low pressure is created upon the leeward side of the train, bridging the gap between the roof and bogie low pressure regions seen at 0^o. The pressure results at 10^o show an indent of higher pressure within the low pressure region, this is caused by the flow recirculation occurring within this region.

7.3.2. First car

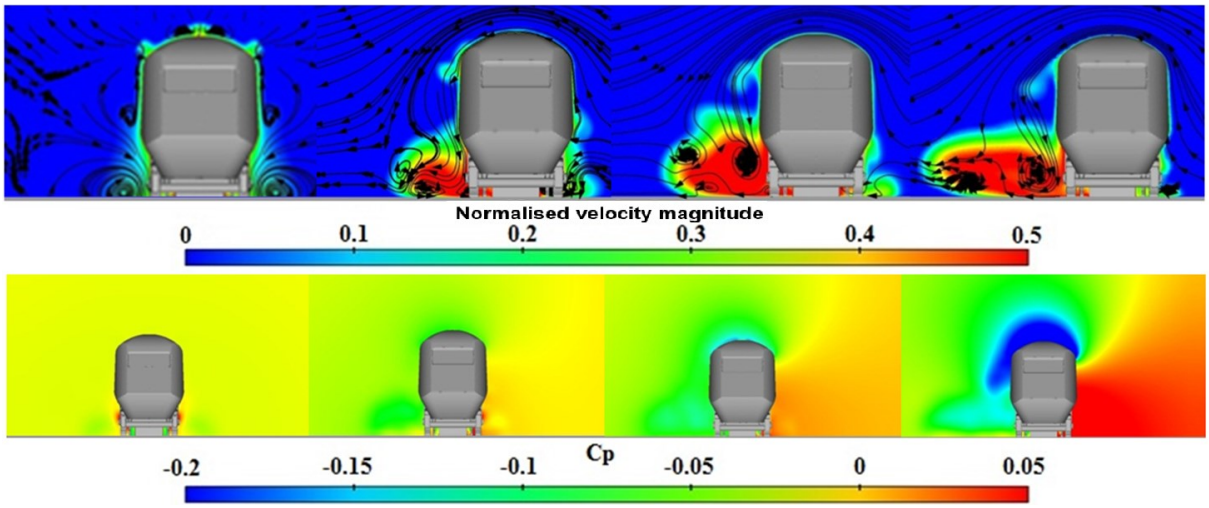

Figure 63: 2D cross-section through computational domain at 10m after trains nose for each of the four yaw angles investigated, colour contoured by normalised velocity (top row) and C_p (bottom row).

Figure 63 shows normalised velocity magnitude and pressure coefficient contours upon a cross sectional plane through the domain at 10m from the nose of the train. Unlike the plane location used in Figure 62 this plane passes through the large region of accelerated flow created by the first bogie seen in Figure 60. In the no crosswind case it can be seen that a large vortex exists down near the ground plane, this vortex is created by flow separating from the first bogie. Upon the leeward side as the yaw angle is increased up to 5^o two vortices now exist, both of these are situated close to each other at the outer extent of the high velocity region. Within the 0^o case the vortex was fed by flow from the bogie, the vortices at 5^o are also partly fed by flow coming down from the roof region. In both the 10^o and 15^o cases the vortex fed from the roof region move closer to the train and higher up the trains side, this is due to the increased amount of flow separating from around the first bogie.

Like the 2.5m results the slipstream on the windward side of the train gets compressed by the oncoming flow in the crosswind cases, the amount by which the slipstream is compressed increases with yaw angle. The effects of this increase in yaw angle are more oncoming flow to the windward side, this can be seen by how the pressure increases with yaw angle. The increase in crosswind velocity causes flow to accelerate and separate over the leeward side of the roof, this creates a low pressure over the roof and on the leeward side. This effect becomes most significant between the 10^{o} and 15^{o} results where the pressure change is at its greatest.

7.3.3. Remaining cars

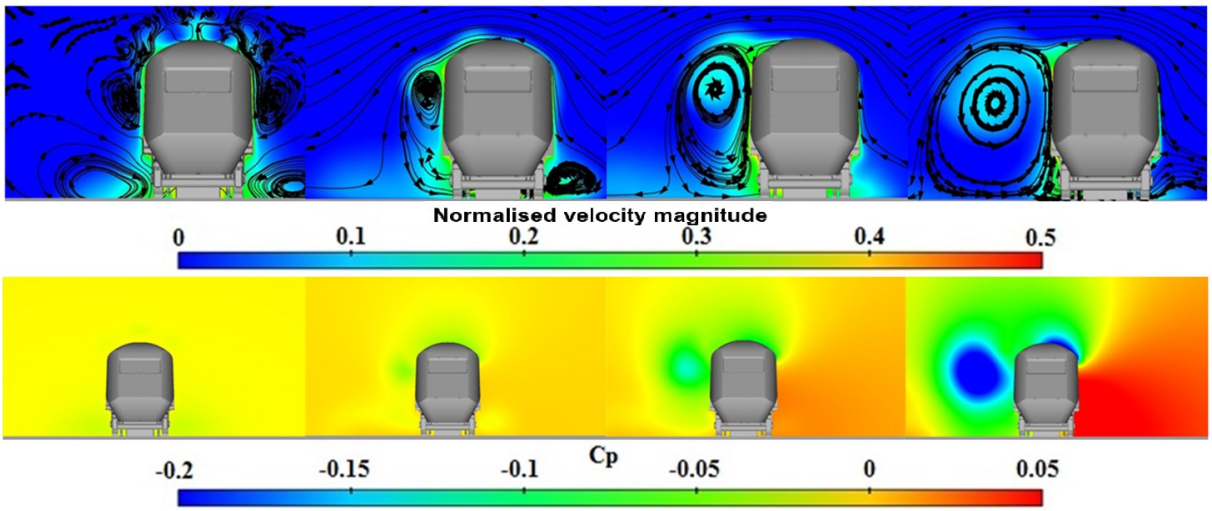

Figure 64: 2D cross-section through computational domain at 30m after trains nose for each of the four yaw angles investigated, colour contoured by normalised velocity (top row) and C_p (bottom row).

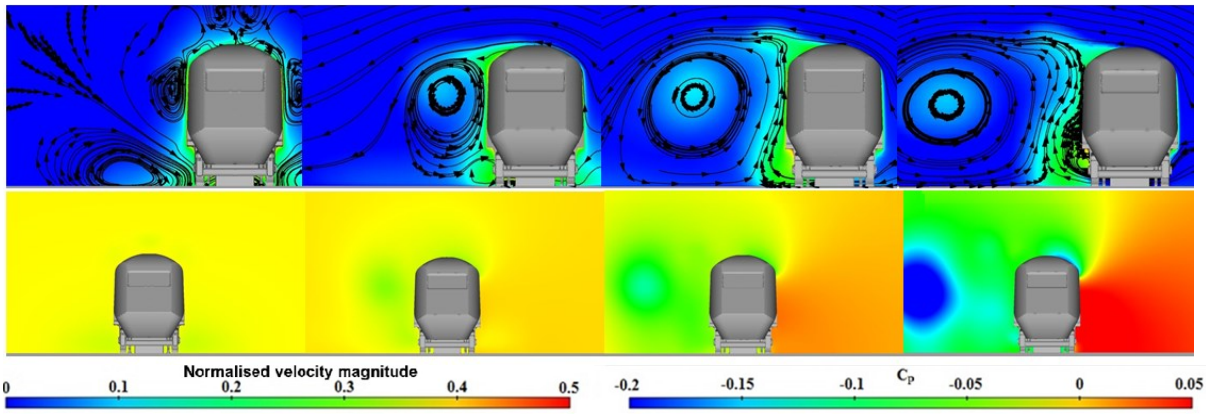

Figure 65: 2D cross-section through computational domain at 53m after trains nose for each of the four yaw angles investigated, colour contoured by normalised velocity magnitude (top row) and C_p (bottom row).

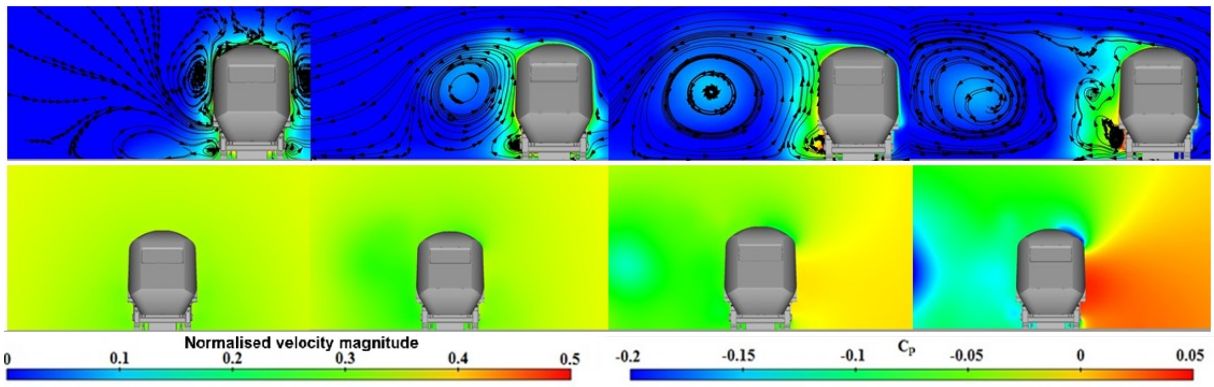

Figure 66: 2D cross-section through computational domain at 73m after trains nose for each of the four yaw angles investigated, colour contoured by normalised velocity magnitude (top row) and C_p (bottom row).

Figure 64, Figure 65 and Figure 66 show planes through the domain at 30m, 53m and 73m from the trains nose respectively which corresponds to the middle of the second, third and fourth cars. At each of these locations the no cross wind results show vortices situated at the ground plane either side of the underbody region, vortices are also formed at the top of the trains sides near the roof edges. At 28m above the roof of the train two counter rotating vortices form situated just either side of the centre line. Multiple vortices also exist around by

the roofs edge, by 53m these vortices no longer exist due to a balance of dissipating and being absorbed into the remaining larger vortex at each side. Except the aforementioned differences as distance along the train increases the main change to the flow around the train is the growth in size of each of the four main vortices and the reduction in pressures around the train caused by the boundary layer build-up.

At a yaw angle of 5^o the flow field around the train drastically changes, on the leeward side at 28m the lower vortex no longer exists whilst on the windward side the vortex by the roof no longer exists. As the distance along the train increases the leeward side vortex grows in size with its core moving further from the trains surface, this results in a pressure drop occurring on the leeward side of the train. By 53m the windward side the lower vortex no longer exists having dissipated due to the oncoming cross wind flow. At all three measurement locations the 10^o and 15^o results do not show any vortices on the windward side of the train. At 28m the leeward side vortex is considerably larger in the 10^o results than in the 5^o results, by 15^o the leeward vortex is now roughly the same height and width as the train itself, this causes a large region of very low pressure to the leeward side of the train.

By the 53m plane the leeward vortex is situated further from the side of the train in turn moving the low pressure region further from the trains side and creating a region of separation on the leeward side of the roof. At 73m the vortices are situated further from the side of the train in the 10^o and 15^o cases. The 10^o results show a small region of recirculation next to the underbody of the train. The vortex in the 15^o results is fully separate from the surface of the train, this allows a smaller vortex to form in the gap at around half train height. The pressures on the leeward side of the train at 15^o are lower due to the vortex moving further away and the accelerated flow being released from the roof.

7.3.4. Wake

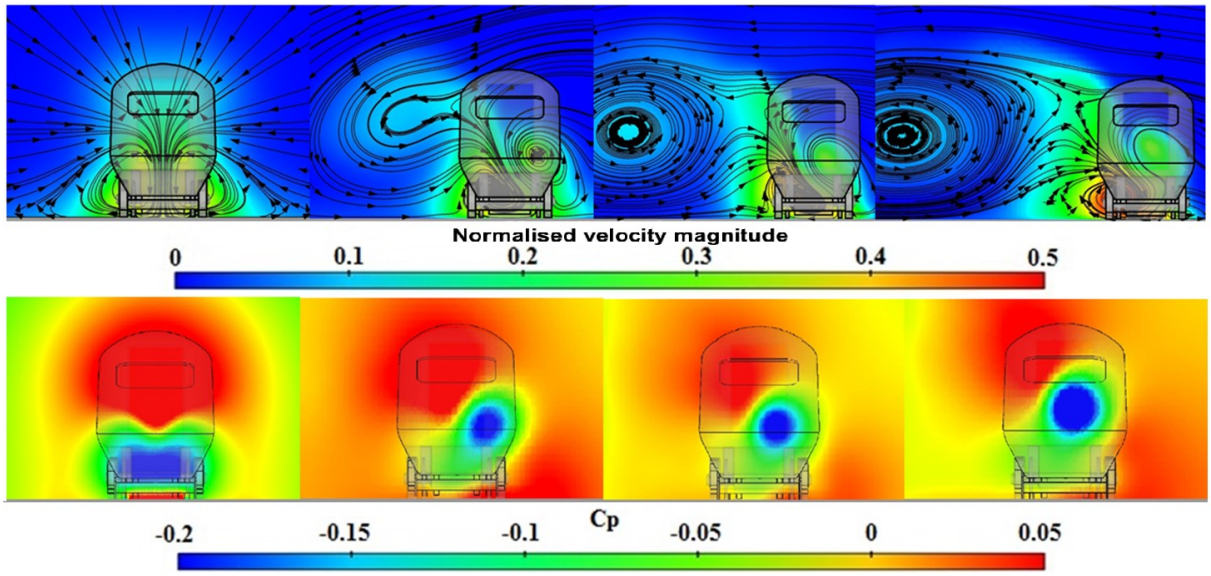

Figure 67: 2D cross-section through computational domain, within the wake region at 85m after trains nose for each of the four yaw angles investigated, colour contoured by normalised velocity (top row) and C_p (bottom row).

Figure 67 show cross sections through the wake of each of the four yaw angle cases at 85m from the trains nose, these cross sections show the pressure and velocity contours along with streamlines showing the directions of flow within this region. As seen in chapter 5 the wake of the no crosswind case features two counter rotating vortices situated close to the ground plane, these vortices cause a region of high velocity and low pressure close to the ground whilst from around half train height and up a high pressure region exists. At a yaw angle of 5^o the leeward side vortex is situated more central to the train. The windward vortex moves from the ground plane up to around half train height at its core, this is due to the crosswind creating a large low velocity recirculation region on the upper leeward side of the train. this draws the windward vortex up whilst pusing the leeeward vortex underneath it. The high velocity region of the wake still remains central to the train despite the movement of these vortices, however the very low pressure region is now situated close to the core location of the windward vortex.

At 10^o the recirculation region seen at 5^o on the upper leeward edge is replaced by the large vortex previously seen in Figure 64 through to Figure 66, the core of this vortex is far from the train so the pressure drop only causes a small effect upon the pressures within the wake. The velocities within the wake at 10^o are simular to that of the 5^o results as are the locations and sizes of the two vortices. At 15^o the flow patterns within the wake of the train are significantly different to those seen at lesser yaw angles, the two main vortices still exist but they are now seperated by two smaller vortices within a region of higher velocity than seen in the 0^o through to 10^o cases. The two vortices between the main vortices rotate counter clockwise to the larger vortex they are nearest to, these votices are produced by the high amount of flow coming in to the wakes centre from both sides and passing down between the two vortices which are now further appart. The complex and higher velocity flow within the wake at 15^o causes the very low pressure region to grow in comparison to the lesser yaw angles.

7.3.5. 2D plane results summary

Results for the two dimensional planes through the geometry show that the largest C_p changes due to yaw angle changes occur around the nose and first car region of the train, this is due to the blunt shape of the train and this region being the first part of the train to encounter the air and crosswind flow. Along the length of the train the windward side remains above atmospheric pressure whilst the 10^o results remain around atmospheric pressure. The 5^o results show a drop in windward pressure as the distance along the train increases. The roof and leeward side of the train show greater variation in pressure magnitudes as they are exposed to regions of flow separation and large vortices upon the leeward side. On the leeward side as yaw angle increases the pressures coefficients can be seen to decrease, this is

due to the main leeward vortex increasing in size. Increases in the distance along the train also lead to a decrease in C_p values due to the vortex moving further from the trains side increasing the size of the low pressure region.

7.4. Measurement line results

Within this sub chapter the effects of crosswinds on the slipstream of a high-speed passenger train are assessed using numerical results from measurement lines within the trains slipstream. These measurement lines are located at 3m from COT and 0.2m and 3m above TOR and situated upon both the windward and leeward side of the train. Comparisons are drawn using both normalised sum velocities (X, Y and Z velocity components) and pressure coefficients which were calculated using the same approach previously mentioned within this thesis.

7.4.1 Windward measurement lines

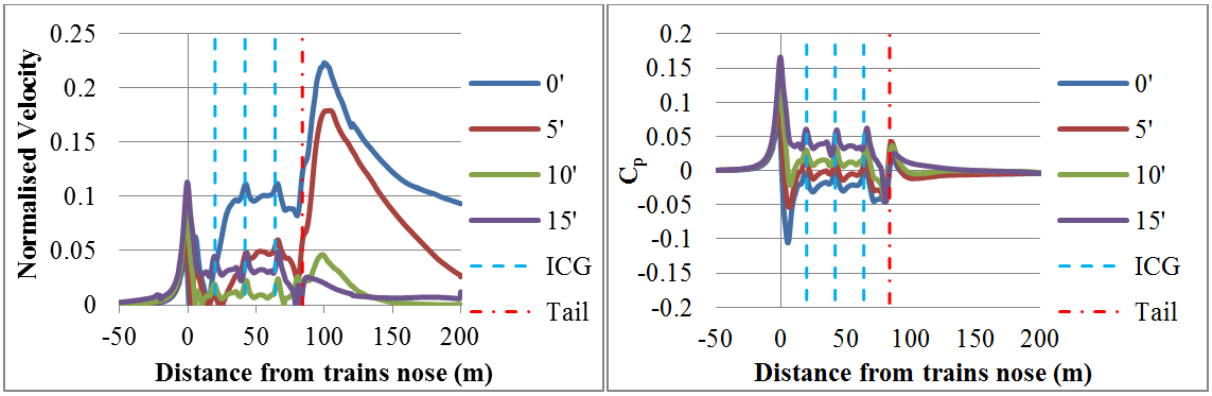

Figure 68: Graphs showing normalised velocity and C_p at 3m from COT by 0.2m above TOR on the windward side of the train for each of the four investigated yaw angles.

Figure 68 shows the normalised velocity and the C_p results for each of the four yaw angles at a measurement location situated 3m from the COT and 0.2m above TOR on the windward side of the train. At this location it can be seen that crosswinds cause a large effect upon the

normalised velocity within the slipstream. The normalised velocity within the no crosswind case peaks at 0.05 in line with the nose (0m) before peaking again to around 0.06 (5m) as flow reverses around the first bogie of the train, over the length of the first and second cars the flow begins to be drawn along by the train as the boundary layer builds up. As yaw angle is increased the velocity spike seen at the nose of the train increases in magnitude, this is due to the high velocity "bubble" moving towards a windward direction as seen in Figure 59.

The secondary flow reversal peak that directly follows the nose spike is significantly more sensitive to crosswind angle, by 5^o the normalised velocity is now half that of the no crosswind case. At 10^o the normalised velocity is now only a quarter of the no crosswind cases value. The results for the 15^o yaw angle show a much larger velocity along the first car as no flow reversal occurs. The results around the flow reversal region at 5m are more sensitive to yaw angle than at the initial spike due to the reduction in flow separating from the windward side of the first bogie as yaw angle is increased. Less flow separates from this region at higher yaw angles for two reasons, firstly the shape of the geometry becomes less blunt to the flow as the flow begins to approach onto the corner as well as the front and side faces. Secondly the increase in yaw angle presses flow into the sides of the bogie region. This effect can be seen in the C_p results of Figure 68 where the C_p rises with yaw angle.

The tail of the train shows the largest variance between the four yaw angle cases for the normalised velocity but shows very little change for the C_p values. The no crosswind case shows a rise in velocity at the tail of the train followed by an additional rise within the wake. This additional rise is due to the formation of vortices which create a large region of accelerated flow that moves through the measurement point. As the yaw angle is increased the region of accelerated flow no longer travels out as far from the trains centre, this causes the wake velocities to significantly decrease. The wake no longer moves out from the underbody

due to the oncoming crosswind flow compressing against it. The pressure remains relatively constant between the different results due to the region being away from the trains body.

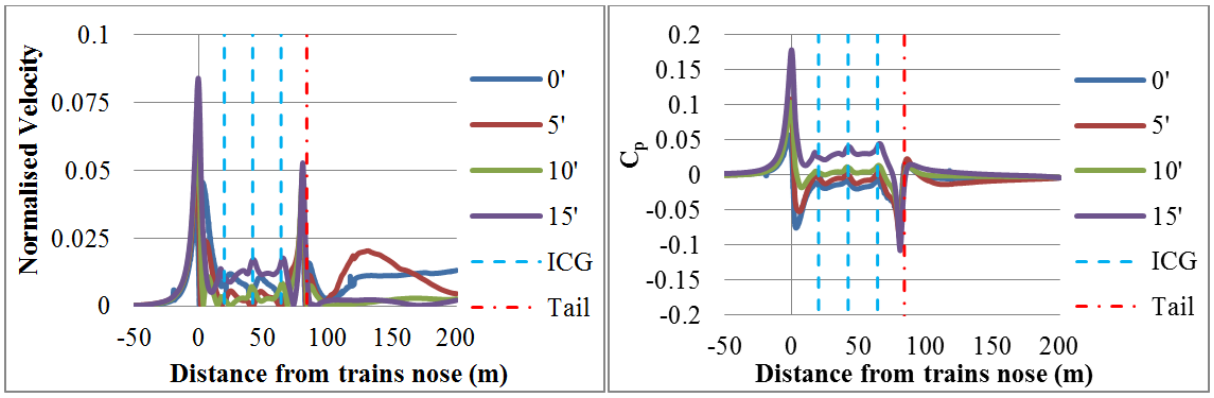

Figure 69: Graphs showing normalised velocity and C_p at 3m from COT by 3m above TOR on the windward side of the train for each of the four investigated yaw angles.

Figure 69 shows the normalised velocity and the C_p results for each of the four yaw angles at a measurement location situated 3m from the COT and 3m above TOR on the windward side of the train. This location is situated close to the roof region which in the results of section 7.3 proved to be highly sensitive to the crosswind yaw angle. On the windward side of this train both the pressure and normalised velocities follow similar profiles with similar effects caused by crosswinds. Both the C_p and normalised velocity show a large spike around the nose of the train, despite the height increase of the measurement location these spikes are around the same magnitude as those seen in Figure 68 which suggest ground proximity may not be important around the nose. For the entirety of the trains length the windward side of the train shows higher pressure coefficients and normalised velocities as yaw angle is increased.

At the tail of the train all four approaches predict similar negative spikes in C_p, the flow at the tail of the train is reversed due to this low pressure. All four yaw angles predict similar normalised velocity spikes within this recirculation region. The results show that the velocity

spike that occurs just after the tail of the train is sensitive to yaw angle. This is due to how the flow accelerates over the top edges of the roof and into the wake, at higher yaw angles this flow curves towards the leeward side of the train and away from the measurement location. The 0^o and 5^o results show a raise in velocity starting at around 100m from the trains nose, this is caused by growth of the wake but also the movement of the windward vortex in the 5^o case.

7.4.2 Leeward measurement lines

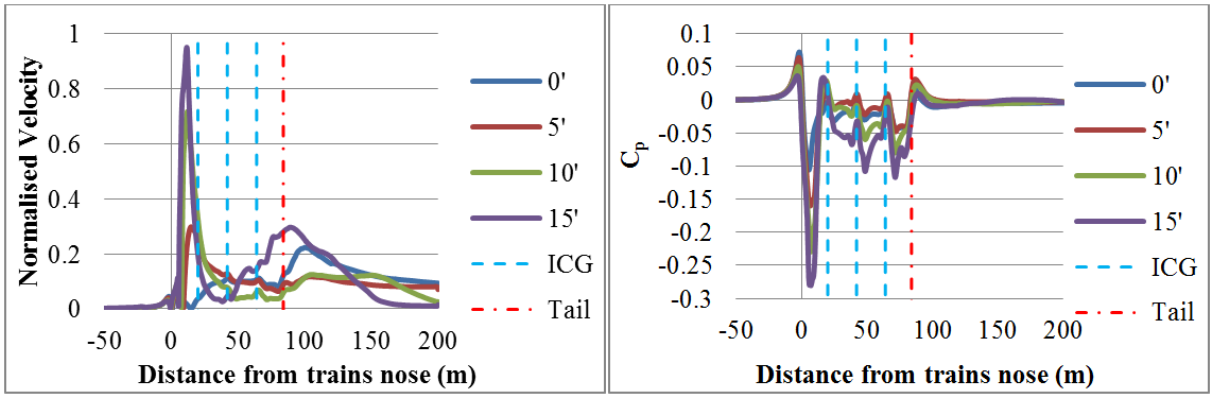

Figure 70: Graphs showing normalised velocity and C_p at 3m from COT by 0.2m above TOR on the leeward side of the train for each of the four investigated yaw angles.

Figure 70 shows the normalised velocity and the C_p results for each of the four yaw angles at a measurement location situated 3m from the COT and 0.2m above TOR on the leeward side of the train. Unlike on the windward side all four yaw angles now show similar velocity spikes around the nose of the train, the range of any variations at this point is overshadowed by the large velocity spike that occurs straight after. This large spike is caused by the acceleration of flow as it separates off of the first bogie of the train, as seen in Figure 60. Between the 0^o and 5^o results there is a difference in the normalised velocity of around 0.3,

from 5^o to 10^o the normalised velocity increases by approximately 0.4 whilst the increase up to 15^o from 10^o is only 0.25. This drop in the rate of velocity increase suggests that the most sensitive angle for this first bogie is between 5^o and 10^o, the results also suggest that if yaw angles above 15^o were tested the rate at which the normalised velocity would increase would continue to decrease.

The large velocity spike around the first bogie also creates a region of very low pressure, at a yaw angle of 15^o the C_p is nearly three times that of the no crosswind case. Along the remainder of the trains length the 5^o and 10^o results continue to show a steady if slightly declining normalised velocity, although not at a very high velocity it is still higher than on the windward side. The 0^o and 5^o results predict a higher normalised velocity than that of the 10^o, this is a result of the increased amount of flow passing to the leeward side of the first bogie at the lower yaw angles. The 15^o results show an increased normalised velocity along the final two cars due to the increased amount of flow passing under the trains cars.

At the 10^o and 15^o yaw angles the leeward side of the train is exposed to lower pressure coefficients than lesser angles, this is due to the large vortex that separates from the trains surface as can be seen in Figure 64 through to Figure 66. Within the wake of the train the variance in pressures is notably smaller in comparison to other pressure features. A difference however can be seen to occur in the velocities where the 5^o and 10^o show no velocity spike whilst the 0^o and 15^o results do. This difference is due to the accelerated regions of the wake at 5^o and 10^o not spreading out as far into the wake due to the location of the vortices.

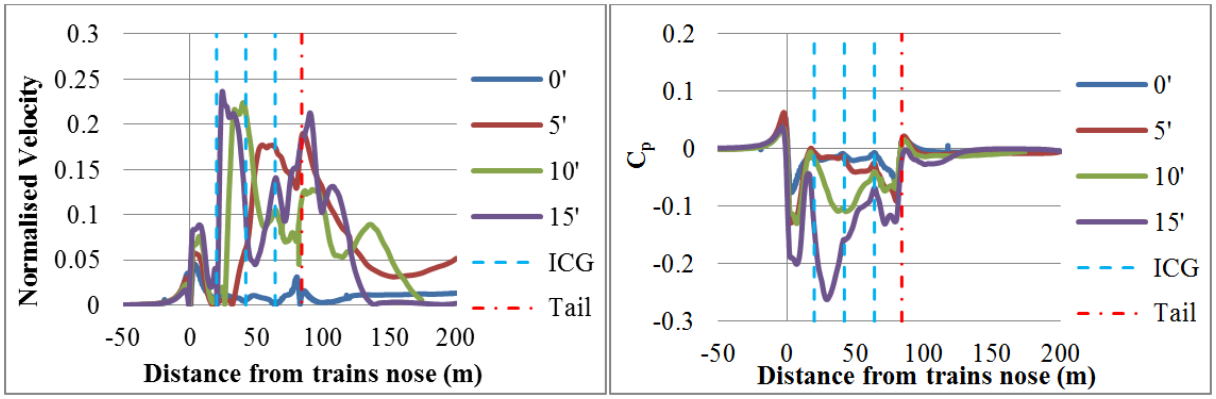

Figure 71: Graphs showing normalised velocity and C_p at 3m from COT by 3m above TOR on the leeward side of the train for each of the four investigated yaw angles.

Figure 71 shows the normalised velocity and the C_p results for each of the four yaw angles at a measurement location situated 3m from the COT and 3m above TOR on the leeward side of the train. Unlike the windward results at this measurement location each yaw angle shows dramatically different normalised velocities. The results show similar rises in the normalised velocity ahead of the nose for each yaw angle. After this rise is a region of recirculating flow, the velocity within the recirculation region is much higher than the nose peak and increases as yaw angle does. After the first ICG large differences occur in the normalised velocities, the 10^o and 15^o results both show the normalised velocity increasing up to the 0.2- 0.25 range as the shed vortex passes through the measurement location. Velocities for both of these yaw angles decrease after this initial spike, this is due to the vortex moving away from the measurement location.

After the second ICG the 15^o results again show a raise in the normalised velocity due to the build-up of a secondary vortex at this location. The 5^o results do not peak until the middle of the third car. At the tail region all three yaw angles show an increase in the normalised velocity whilst the 10^o and 15^o results also show additional increases further within the wake,

these additional increases are caused by the passing of a high velocity wake flow feature through the measurement location. The pressures at this location are less sensitive with the 5^o cases predicting results close to that of the 10^o yaw angle for the first and final cars and close to the no crosswind case for the second car, this occurs impart due to the different curvatures of the two car types. The 10^o and 15^o results show large pressure drops over the second and third cars, this is due to the measurement lines location close to the core of the secondary vortex that is shed from the first ICG at these yaw angles.

7.4.3. Measurement line conclusion

Results from the measurement lines show that the windward side of the train is less sensitive to changes in yaw angle than that of the leeward side, this can most clearly be seen for the results at a measurement height of 3m from COT by 3m Above TOR. At this measurement location all four yaw angles cause not only different velocity magnitudes but also notably different profiles along the trains length, this was due to how the main (initial) leeward roof vortex varied greatly in its size and position at each yaw angle. The leeward results at 0.2m above TOR showed the largest overall velocity spikes created by flow accelerating around the first bogie and launching mechanism, beyond this the results for all but the 15^o yaw angle were comparable, with the 15^o varying due to the increased flow passing under the train. Results for the windward side of the train show pressure coefficients increasing as yaw angle is increased, this is the case for both measurement locations used. The 0.2m height windward location shows a drop in normalised velocity as yaw angle is increased whilst the 3m above TOR location shows an increase in normalised velocity, this is due to the acceleration of flow over the roof region.

7.5. Conclusion on the effect of crosswinds on the slipstream of a HST.

From the results presented within this chapter it is possible to conclude that a class 43 or likely any passenger train with similar key geometric features is highly sensitive to even small changes in yaw angle. The results from the different approaches constantly showed that in key areas such as the nose, wake and leeward side of the roof a yaw angle as low as 5^o can cause large variations in both the time averaged pressure and velocity of the slipstream. Results also showed that above 10^o the windward side boundary layer of the train was significantly reduced in size and velocity whilst pressures on this side of the train increased to above atmospheric pressure. On the leeward side of the train the results again showed a notable difference between 5^o and 10^o. At 15^o a large vortex could be seen to form and separate from the leeward side of the train whilst a further vortex built up upon the leeward edge of the roof. This had large effects upon the pressures upon the leeward side which decreased as yaw angle increased.

The nose region of the train was found to cause the largest rises in C_p whilst the largest drop in C_p was noted on the leeward side of the train just after the first bogie and launching mechanism, this was also the location of the highest normalised velocities, peaking just short of 1 for the 15^o yaw angle. Near the roof region the highest velocities were recorded just after the first ICG for the 10^o and 15^o cases however these were to a much lower value of 0.2 – 0.25. The large effects of the crosswinds on the slipstream seen within this chapter are likely to cause a large effect upon how the train complies with regulations currently in place and therefore will be investigated within a later chapter.

Chapter 8. Effect of Crosswinds upon regulations

8.1. Introduction

From the results shown in chapter 7 it is possible to see that even small yaw angles can produce a large effect upon the pressures and velocities within the slipstream of a passenger train shaped such as the one investigated. The TSI regulations which cover the operation of trains throughout the UK and Europe specify limits for both velocities and pressures within the slipstream of high-speed trains to ensure the safety of personnel and structures both inside and out of the train. The TSI requirements state that crosswinds must be under 2 m/s during testing, therefore the results of this chapter feature little bearing upon the trains compliance to regulation requirements. Instead the results of this chapter aim to provide an insight into how these key safety measurements are affected by crosswinds and as to how lenient they are.

8.2. Effect of crosswinds on Pressure based regulations

In order to ensure safe operation of trains throughout Europe a maximum pressure variation between two peaks of 795 Pa is stipulated within the TSI for class 1 trains running below 250 km/h in open air. In order to evaluate the effect of crosswinds upon this requirement, results from CFD simulations were measured and analysed in accordance with part four, section 5.4.3 of the CEN code. This section of the code defines the requirements when characterising the pressure profile of a trains slipstream at model scale. This section states that measurement locations must be situated 2.5m from COT and at heights above TOR ranging from 1.5m – 3.3m, in 0.3m intervals. These measurement locations were replicated within the CFD work for both the leeward and windward sides of the train. To correct the measured pressures to

full scale velocities (55.88 m/s) from model scale equation 42 below was used, as specified within CEN section 5.4.3.

$$P_f = P_s.\left(\frac{V_f}{V_s}\right)^2 \quad 42$$

The variable P_f corresponds to the full scale pressure value whilst P_s is the measured scale pressures. The variables V_f and V_s correspond to the full scale and model scale velocities of the train. The full scale value was set as 55.88m/s which is the trains maximum velocity, the model scale value was set at the corresponding model train speed which was dependent upon the yaw angle investigated. To comply with the TSI testing procedure a class 1 train must produce a scaled peak to peak pressure of less than 795 Pa, this is including two standard deviations of the multiple tests.

The regulations also state that the tests should be carried out upon a ballasted single track of 0.75m ± 0.25m height and that the recording of data should include one second of data prior to the train passing and ten seconds after the tail passed. Neither the ballast or measurement time requirements were met within this research, the time requirements were not met as using the DDES approach this would require a non feasible amount of time. The results were however still suitable for their purpose of investigating how crosswinds affect this passing average value and provide an insight into the potential implications crosswinds could cause on these regulations should the full test criteria be met. Peak to peak pressure results are calculated using time average pressure results whilst the specified two standard deviations are calculated from transient results from ten non sequential time steps, the use of ten non-consecutive data sets matches the CEN requirement for ten independent data sets.

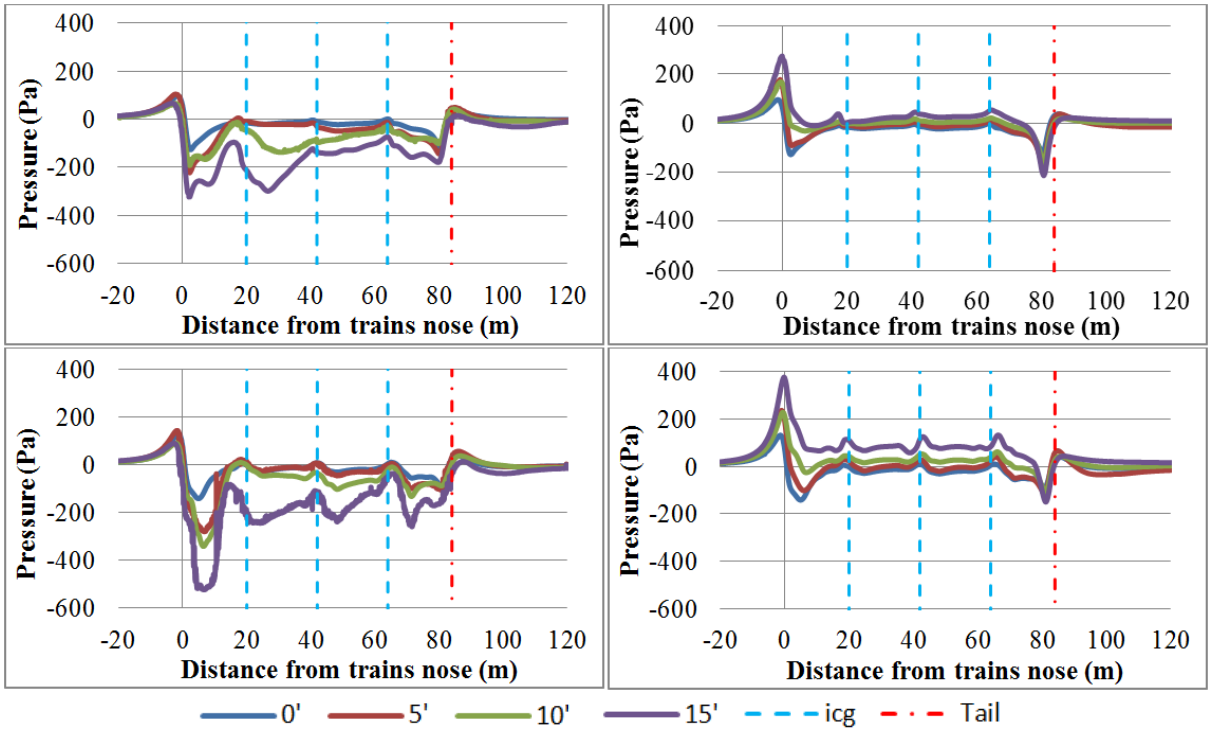

Figure 72: Scaled pressures at measurement locations 2.5m from COT by 3.3m (Top row) and 1.5m (Bottom row) above TOR for both the leeward (Left) and windward (Right) sides.

Figure 72 shows the time averaged pressure results from the measurement heights of 1.5m and 3.3m. The choice to include only the 1.5m and 3.3m measurement height results within this chapter was made due to these two locations producing the extremes of the measured pressure profiles. From the results of Figure 72 it can be seen that both the leeward and windward sides of the train slipstream produce larger pressures peaks around the nose at a height of 1.5m than at 3.3m. The 3.3m windward results show a larger negative pressure peak at the tail of the train than at a height of 1.5m.

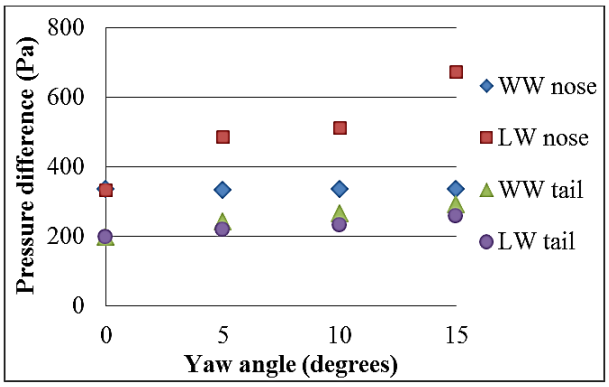

Figure 73: Peak to peak pressure fluctuation values plus 2 SD against yaw angle

Figure 73 shows a graphical visualisation of the maximum peak to peak values upon both the windward and leeward sides of the train for the nose and tail regions at each yaw angle. From the graph it can be seen that the peak to peak variation is always greater at the nose of the train than the tail. Upon the nose the leeward side of the train experiences a considerably high variation than that of the windward side. At the tail the results are much closer but now the windward side results feature a higher variation.

The leeward side of the nose is the only region of the train that shows a high level of sensitivity to yaw angle with the pressure variation doubling between 0^{o} and 15^{o}. The tail results show a small rise as yaw angle is increased. The windward nose results show no significant fluctuation. The largest peak to peak value was recorded around the leeward side of the nose at 1.5m above TOR at a yaw angle of 15^{o}. With the addition of two standard deviations as specified within the TSI the peak to peak value was 673 Pa, this is still significantly below the class 1 maximum allowed of 795 Pa. the tail and windward side measurements do not exceed 50% of this limit at any of the yaw angles.

8.3. Effect of crosswind on velocity based regulations.

In order to ensure the safety of trackside workers as trains pass by, regulations exist for class 1 trains to ensure no slipstream gusts are above what is considered a dangerous level. Within section 4.2.6.2.1 of the TSI, the regulations state that at a location of 0.2m above TOR and 3m from COT the maximum permissible average airspeed plus two standard deviations for the passing of a class 1 train is 20m/s. The regulations state that this limit is to be calculated using the mean recorded air velocity for the passing of a train including one second prior and ten seconds after, on top of this two standard deviations of the data are to be added. Within this thesis this is referred to as the TSI passing average. The TSI regulation defines that the testing must be conducted with ambient wind speeds below 2 m/s. As these requirements do not take in to account the effects of crosswinds and thus could miss potential safety issues during strong crosswind situations it is important to investigate the effect crosswinds cause upon class 1 trains.

As with the pressure tests the regulations state that tests should be conducted upon a ballasted single track of 0.75m ± 0.25m height. Results from chapter 5 show that the inclusion of a ballast shoulder as specified would lead to a decrease in the measured velocities. The TSI regulations also state that the recording of data should include one second of data prior to the train passing and ten seconds after the tail passed, at the speed of the train that is equivalent to 56m ahead and 560m behind the train. This is 444m further than the computational domain extends. Within the wake region the assumption can be made that the wakes velocity would not further increase, this in turn could reduce the TSI passing averages in comparison to the values calculated within this research.

To enable the analysis to be conducted, the velocities from the CFD simulations were first adjusted to correct for the ambient flow moving instead of the train. The velocities were then scaled up to a full train speed of 55.88 m/s through use of equation 43, this equation is a variation upon equation 42.

$$U_f = U_s.\left(\frac{V_f}{V_s}\right)^2 \qquad 43$$

Where U_f equals the full scale slipstream velocity, U_s represents the model scale slipstream velocity, V_f and V_s represent the full scale and model scale train speeds respectively, results within this section use the correct method of averaging plus two SD albeit not including the full trains wake as specified. The averaging and addition of two standard deviations of the transient results relies upon data from ten non-consecutive time steps.

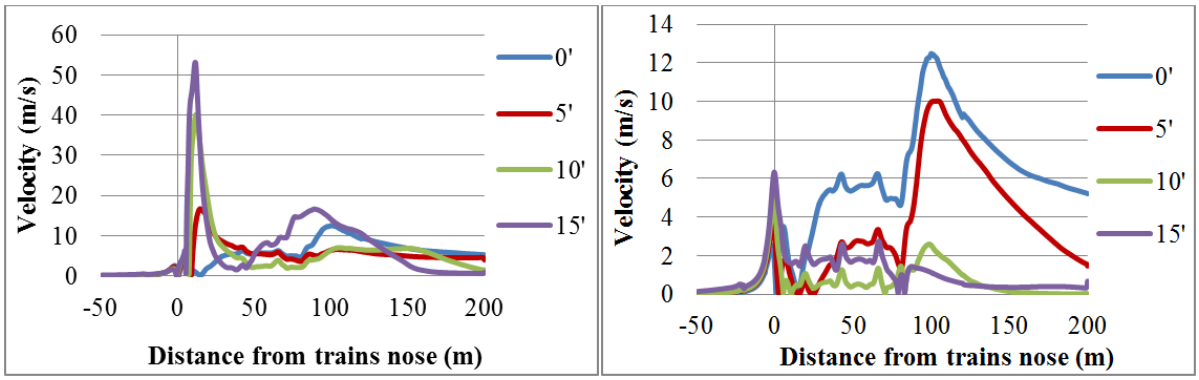

Figure 74: Leeward (left and windward (right) side slipstream velocities for each yaw angle investigated.

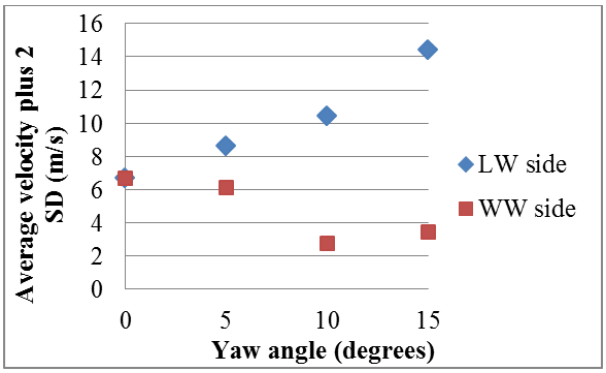

Figure 75: TSI passing average values for windward and leeward sides of the train for each yaw angle investigated.

Figure 74 shows the leeward and windward side velocity profiles for the four yaw angles investigated whilst Figure 75 shows the TSI passing average for each side of the train and yaw angle. On the windward side of the train the highest velocity was recorded in the 0^{o} yaw angle case at 12.3 m/s, the TSI passing average at this yaw angle was 8.1 m/s. This average value is below the requirement of 20m/s which is to be expected due to the train being in operation throughout the UK, however even the peak velocity is over 7m/s below the average which suggests this limit value may be more applicable to freight rather than class 1 passenger trains. As the yaw angle increases both the windward peak and TSI passing average values decrease. At 5^{o} the TSI passing average decreases to just above 6 m/s with a peak at 10m/s. The TSI passing average is 3.5 m/s at a yaw angle of 10^{o} and just 2.8 m/s at a yaw angle of 15^{o} with peaks at 5m/s and 6.5m/s respectively. These findings regarding velocities reducing during crosswinds is to be expected from the findings of chapter 6 which were recorded at the same measurement location.

Upon the leeward side of the train at a yaw angle of 5^o there is a peak velocity of 16 m/s around the trains nose and a TSI passing average of 9 m/s. The results for the 10^o yaw angle peak at a value of 40 m/s around the trains nose with a TSI passing average of 11 m/s. The 15^o yaw angle results peak at a value of 53 m/s for the velocity at the trains nose and 16 m/s at the tail, The TSI passing average is 15 m/s which is only 75% of the TSI limit. These results show that even when two standard deviations are accounted for at a yaw angle of 15^o the resultant average is well below the velocity of the limit.

8.4. Summary of findings.

From the pressure section it can be seen that with no crosswinds the requirement of a peak to peak pressure value below that specified within the TSI is easily achievable for this train geometry and likely any similar. The results show that yaw angles up to 15^o cause little effect upon the peak to peak pressures upon the windward side though do cause the entire nose pressure profile around the nose to offset towards higher values. The leeward side of the train showed larger variation with yaw angle. This larger variation is due to the increase in the magnitude of the low pressure peak at the trains nose. The results show that yaw angle causes only a small effect upon the positive pulse preceding the negative pulse. The results for the leeward side do not exceed the TSI limit though become close at a yaw angle of 15^o. It is likely that the peak to peak difference will increase further with an increase in yaw angle though the rate of increase will likely drop off at higher yaw angles.

Results for the average velocity show that upon the windward side the trains slipstream is less than half that of the specified maximum, as the yaw angle is increased the average decreases. Upon the windward side the key flow feature is the tail velocity spike which only occurs at

smaller yaw angles. The leeward side of the train shows that increases in yaw angle lead to an increase in the average. At a yaw angle of 15^{o} the average is still below the maximum specified but now by only 25%. Though not a requirement specified within the TSI, it is worth noting the initial nose spike is well in excess of the 20 m/s at a value of 53 m/s.

From the results of both the pressure and velocity sections of this chapter a number of assessments can be made of the testing procedures. The pressure study results show that the lower measurement location is the most critical, this is due to the proximity of the ground plane. The requirement for testing to be conducted at ambient wind speeds below 2 m/s seems restrictive as both the pressure and velocity results show that even at a yaw angle of 15^{o} (approx. 15 m/s crosswind) the aerodynamic variables were below the requirement limits. Combining the results of this chapter with that of chapter 5 it is also possible to assume that the requirement for testing to be on a 0.75m ± 0.25m ballast is over restrictive and that any ballast bellow this height would only serve to increase the measured results. Thereby if a train can pass at a lower height it would pass easier at the specified height.

Chapter 9. Crosswind effect upon surface pressures and aerodynamics forces.

9.1. Introduction.

There are three forces and three moments that act upon a train, these are the lift, drag and side forces and the pitch, roll and yaw moments, of these only a few are of any concern. Due to the length and weight of a train the pitch and yaw moments are insignificant. The drag force is not a safety concern in itself but a less aerodynamic train will produce higher pressures and velocities within the slipstream, furthermore it is important for optimising the trains design for efficiency.

The lift force is important as it can reduce the tractive and braking effort the train can produce before the wheels break traction with the rails, however in regards to passenger safety aboard the train the key aerodynamic variable is the roll or as it is commonly referred to the overturning moment. The overturning moment is primarily a concern for freight trains due to their broad sides, but in extreme cases could pose a derailment risk for high-speed passenger trains. The yaw angle range investigated within this work are relatively small so the risk of overturning would not be a concern. It is however beneficial to develop an understanding of how the overturning moment along with the aerodynamic forces vary at each yaw angle as this could influence development of future trains.

Aerodynamic forces are calculated using the forces calculator within OpenFOAM, and are the sum of both the friction and pressure components, the overturning moment acting upon the

leeward rail is also calculated using this in built function with variables measured from the CAD geometry. The aerodynamic forces are then converted to coefficients using Equation 44.

$$C_{force} = Force/((A/2) * \rho * V^2) \quad 44$$

To help provide a clearer understanding of the reasons behind changes in aerodynamic forces with yaw angle, results within this chapter will first focus upon the pressure fields over the trains surface and how they vary with changes in yaw angle. This is achieved by two methods of analysis, the first relying upon comparisons of surface pressure coefficients over loop locations and secondly through visual comparison of surface pressure contours over the whole train.

9.2. Effect of cross winds on train surface pressures.

Surface pressures acting upon the surface of the train are important as they are key contributors to the aerodynamic forces, they also account for noise and pressure levels experienced by passengers within the cabins, specified limits exist for both of these within the TSI. Results for surface pressure are compared for the four yaw angles investigated at five measurement loop locations, the first three of these measurement loops are situated upon the first car of the train. The choice to focus on the first car was made due to the results of chapter 7 which showed this to be the area with the greatest range of pressures.

The final two measurement locations encompass the whole trains length with additional figures focusing on the leading car. All of the measurement locations match those used in chapter 4, Figure 26. The zero point of the graphs for loops one to three represents TDC of the trains roof, The negative x axis represents the leeward side of the train whilst the positive x

values represent the windward side. On each of the graphs the roof and floor edges are marked for reference. The abbreviations of these edge names and there location can be seen below in Figure 76.

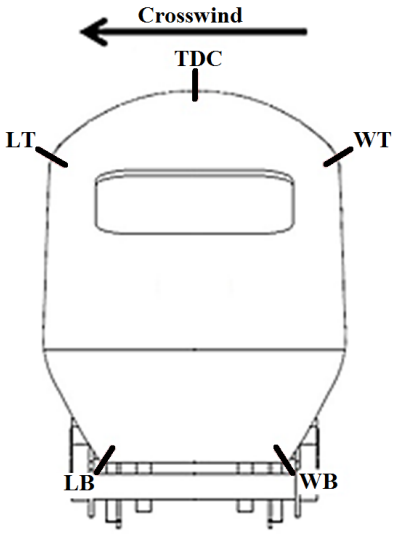

Figure 76: Edge locations and abbreviations

For loops four and five the zero point represents front dead centre (FDC). As in loops one to three the negative x axis represents the leeward side of the train and the positive x axis represents the windward side. In loops four and five the ICG's are marked for reference.

9.2.1. Loops one, two and three

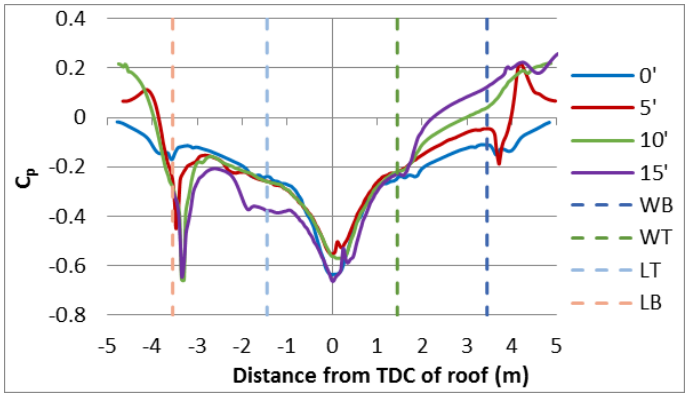

Figure 77: Surface Cp values around loop location 1 (2.75m from front of train).

Figure 77 shows the C_p results for loop location one, this loop is situated at 2.75m from the front of the train. The results at this location show a variation in the sensitivity of the surface pressures to changes in yaw angle depending upon the location around the train. In the work conducted in chapter 4 where CFD results at 0^o yaw were compared to wind tunnel data this location showed large spikes in pressure, particularly over the roof region.

The crosswind results over the roof region show a comparably small sensitivity to yaw angle when compared to the trains sides. At the negative pressure peak the 5^o yaw angle case features the smallest negative C_p at a value of -0.55 whilst the C_p for the 15^o case is 20% lower at -0.66, this is only slightly larger than that of the no crosswind case. The 5^o and 10^o crosswind cases predict lesser surface pressures than that of the no crosswind case in this region due to the movement of the low pressure causing vortices from the centre of the train as seen in Figure 63. The C_p in the 15^o yaw angle case is a larger negative value than the no crosswind case due to the additional low pressure created by flow separating over the windward edge of the train.

The windward side of the trains roof shows little variance between C_p values for each of the yaw angle cases. The pressures upon the windward side of the train all decrease at similar rates as height above ground is increased (towards 0m), however as the side of the train begins to curve into the roof region the pressures drop increases at an increased rate as yaw angle increases. Upon the side of the train it can be seen that the C_p value increases with yaw angle. This corresponds to the results of Chapter 7 which showed slipstream pressures increased with yaw angle.

The leeward portion of the roof and the trains leeward side show little variation between C_p values for the 0^o to 10^o results whilst the 15^o results show large levels of variation. This variation is due to flow separating prior to the mid-point of the roof in the 15^o results. Along the leeward side of the train the C_p values converge at around mid-train height where the flow at higher yaw angles reattaches after separating over the roof region. At the lower leeward edge of the train a large pressure drop occurs for the three yaw angle cases, this is created by flow from the underbody region separating around the sharp edge.

Within the underbody region all but the 5^o case show a gradual rise in pressure towards the centre of the train. The 5^o case also shows a raise in pressure towards the centre however the 5^o results spike sharply either side of the centre. These spikes are likely caused by a flow features from the first bogie that misses the measurement location in all but the 5^o results.

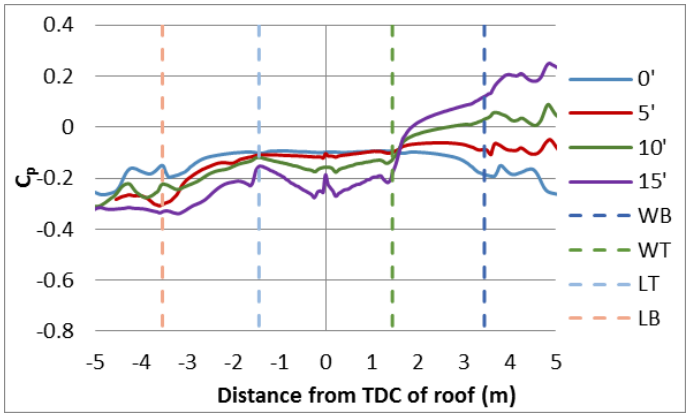

Figure 78: Surface Cp values around loop location 2 (4.125.m from front of train).

Loop two is situated 4.125m back from the nose of the train, the results of the C_p at this loop can be seen in Figure 78. This loop location is situated away from the low pressure roof spike seen in loop one (Figure 77). At this location the difference between all four yaw angles can easily be identified with each yaw angle resulting in notably different C_p values all over the train. All four yaw angles show a rise in C_p as height up the trains leeward side is increased, though the 15^o yaw angle shows a drop just prior to the roofs leeward edge. This drop is closely followed by an increase signifying a small region of separation of the flow.

Over the roof of the train both the 0^o and 5^o cases predict similar C_p values of around -0.1. The 5^o case however shows a small rise in C_p at the roof centre. The 10^o case predicts a near symmetrical profile over the roof and shows a gradual drop towards the roof centre line before spiking back up at the trains centre. The 15^o case shows a much larger spike over the roof centre line with an increase followed by a sharp drop on the leeward side. These rises in pressure over the roof occur due to the roof curve levelling off towards the centre, the sharp drop off seen in the 15^o results is then caused by flow separating at the location the roof begins to curve again.

Upon the windward side of the train the C_p values increase with yaw angle, the increase in C_p is near linear between each 5° increment. Only the 10° and 15° yaw angles feature positive C_p values for the lower half of the trains side. Upon the windward side of the underbody the C_p values fluctuate around a constant for each of the yaw angles. The difference between the no crosswind and 15° yaw angle cases is at its largest in this underbody region of the loop. The no crosswind case features an average C_p of around -0.2 whilst average C_p for the 15° yaw angle is 0.2, this variation will likely cause significant variation of the lift forces experienced by the train.

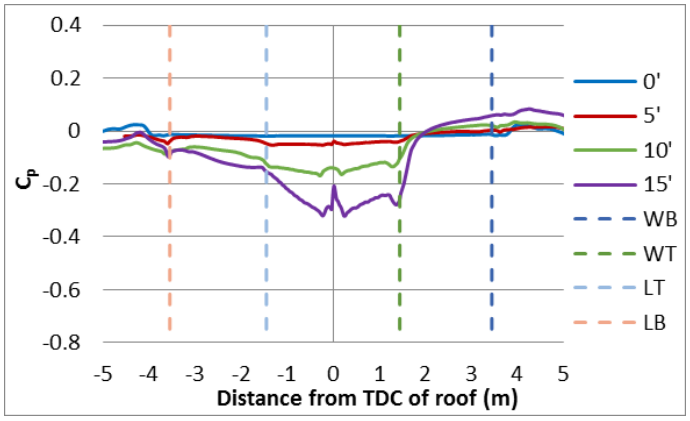

Figure 79: Surface Cp values around loop location 3 (13.125m from front of train).

Figure 79 shows the C_p around loop three. Loop location three is situated near the end of the leading car (13.125m from trains nose). Along this loop the variation in C_p between different yaw angles is smaller than at loops one and two. The 0° yaw angle case shows little variation over the trains sides and roof with the pressure coefficient remaining at a value of around -0.02. Over the sides of the train the 5° results show a small variation compared to the no crosswind case, with the C_p on the windward side of the train being slightly higher and the leeward side C_p being slightly lower. On the leeward side there is a large drop in C_p between

the 5^o and 10^o results and a smaller drop between the 10^o and 15^o results, the larger drop between the 5^o and 10^o results signifies this is a transitional yaw angle for this region where flow beings to separate.

Over the roof of the train the 5^o results differ from the 0^o results with a lower C_p. This is due to the additional velocity of the cross flow over the roof curve. The 10^o results are near symmetrical in profile over the roof but feature slightly lower C_p values on the leeward half due to the flow beginning to separate due to the geometry. The 15^o results show lower C_p values on the upper windward side edge, this is caused by the acceleration of flow over the edge and onto the roof. The windward side of the train and underbody region shows C_p values of around 0 for the 0^o to 10^o yaw angle results. The C_p for the 15^o results are higher at around 0.1 near the lower part of the train. The lower C_p values around this loop in comparison to loop two are due to the larger boundary layer that exists resulting in accelerated flow there by creating lower pressures.

9.2.2. Comparison of loops one, two and three.

The comparison of results from loops one through to three shows a number of trends. Over the roof of the train the C_p values for each of the yaw angles become further apart as distance from the nose increases. At the peak pressure drop over the nose the difference between the different yaw angles is very small, this is due to this area being dominated by flow coming up and over the front of the train. As the distance along the train increases the dominant flow component becomes the crosswind component, this causes large variations in the amount of flow separation which is dependent upon yaw angle.

Along the windward side of the train the variation in C_p at different yaw angles remains relatively constant for the first two loops but greatly decreases at the third. This is due to the rate of boundary layer build-up and the higher pressures upon the windward side of the nose at larger yaw angles taking longer to reduce. The leeward side of the train shows roughly similar surface C_p differences for the 0^o and 15^o results at each loop. At loop one the 10^o results are nearer to the 0^o results but move towards the centre at loop two and by loop three are nearer the 15^o results, this signifies that at 10^o the low pressure region to the trains leeward side is not only smaller but takes longer to form than at 15^o. For loops one and two the 5^o results predict a larger difference from the 0^o results than at loop three, this is due to the separation region around the nose.

9.2.3. Loops four and five

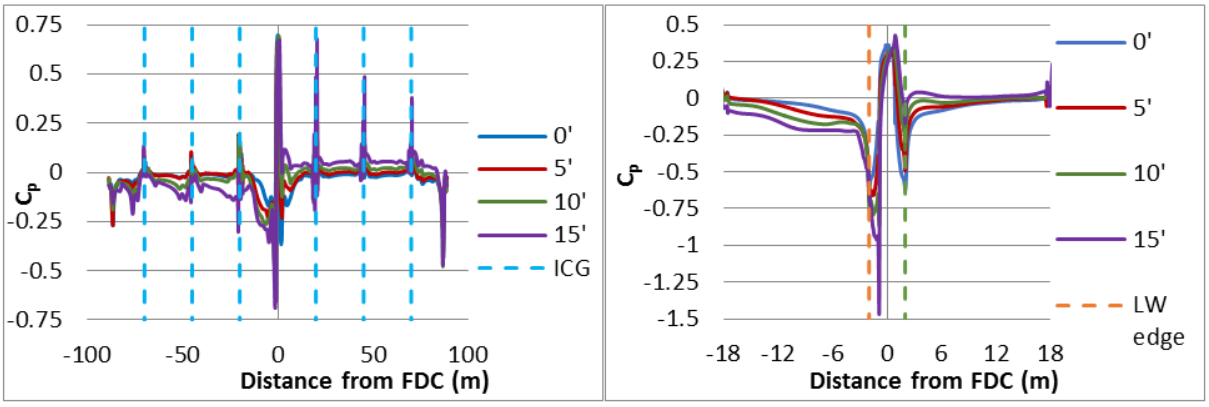

Figure 80: (left) Surface C_p values around loop location 4 for whole train (1.6875m above TOR). (Right) Surface C_p values around loop location 4 for first car (1.6875m above TOR).

Figure 80 shows the C_p around loop location four for the whole train and a close up of the first car. The results for the whole train show that as the yaw angle is increased the windward side of the train will generally experience a higher pressure whilst the leeward side will

generally experience lower pressures, this is as to be expected and remains true at all but the tail region.

On the windward side it can be seen that large spikes in the C_p value occur at the trailing edge of each of the ICG's for the 10^o and 15^o yaw angles, with those of the 15^o yaw angle being over twice the magnitude of the 10^o spikes. Along the side of the second through to fourth cars the C_p values remain relatively constant for each of the yaw angles.

Excluding the first car, the leeward side of the train for the 0^o and 5^o results are indistinguishable from each other. At the first ICG (19m) the three lesser yaw angles all predict near identical C_p profiles and values, the 15^o case predicts a similar profile but at a lower C_p average due to the lower pressures towards the end of the first car. Along the second car the C_p rises for the 15^o case to values much closer to the other approaches, the second ICG causes a further pressure drop which again increases along the third car. The 10^o results also show a drop in C_p after the second ICG, and then once again C_p increases along the third car though at a slower rate than in the 15^o case. This results in all four approaches predicting similar pressure C_p values within the third ICG. Along the fourth car all results show a drop in C_p values, This is due to separation at the leading edge of the trailing car and is caused by the increased size of the trailing car in comparison to the passenger cars.

At the front of the train (Figure 80 right) all four yaw angles investigated predicted similar peak C_p values of 0.65 though as the yaw angle is increased this peak moves slightly nearer to the windward side. As the distance to train edges decreases on either side of this peak there is a sharp drop in the C_p values. On the windward edge the 0^o case predicts the lowest C_p at -0.35 whilst the highest C_p prediction is 0 by the 15^o yaw angle. On the leeward side the 0^o case predicts the highest C_p at -0.35 whilst the 15^o case predicts the lowest C_p at -0.65

mirroring the positive peak magnitude. After this pressure drop the C_p rises up for the four yaw angles as separated flow from the leeward edge reattaches. After the flow reattachment all four approaches predict further drops in C_p by the end of the first car.

On the windward side of the leading car the 0^o case predicts a rise in the C_p after the leading edge flow reattaches (5.3m). The 5^o yaw angle gives a similar prediction of the profile though the C_p drops to a smaller value, this results in a higher pressure as the flow reattaches at -2.6m. Along the side of the car the C_p prediction is only marginally higher than that of the head on case. The 10^o yaw angle predicts a drop in C_p from a positive value down to a negative value around the same corner of the train, by mid-way along the trains side the C_p is again positive. At a yaw angle of 15^o the pressure remains positive along the whole train length.

At the tail end of the train on the windward side the C_p drops for all four investigated yaw angles. Both the 0^o and 5^o results drop to a value of -0.25 whilst the 10^o and 15^o results drop to a value of -0.45. On the leeward side of the train the magnitude of the C_p drop reduces with yaw angle with the 15^o case having the smallest C_p drop whilst the 0^o and 5^o cases drop equal amounts, over twice that of the 15^o case. The variations with yaw angle on the windward sides are due to flow accelerating and separating around the trailing edge of the train to different extents, this is a result of the different angles of incidence for the flow. The leeward side variations are due to the location and structure of the wake within the tail.

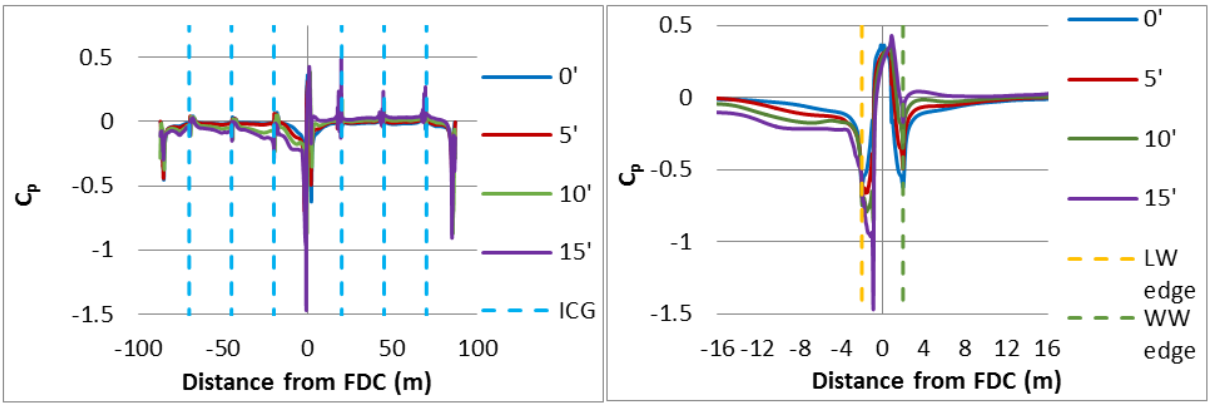

Figure 81: (Left) Surface Cp values around loop location 5 for whole train (2.625m above TOR). (Right) Surface Cp values around loop location 5 for first car (2.625m above TOR).

Loop location five is situated at 2.625m above the top of rail, Figure 81 shows the loop for the whole train and a crop focusing just on the leading car. As with the results for loop four the results at loop five feature a general trend for the C_p to increase with yaw angle on the windward side whilst decreasing with yaw angle on the leeward side. On the windward side of the train the C_p spikes at each of the ICG's are now smaller than in loop four, this is due to the decreased slipstream velocity at this height above TOR. Along the side of the trains passenger cars all four yaw angles predict C_p values around 0 with 0^o and 5^o being just below and the 10^o and 15^o cases situated just above.

Around the nose of the train the 5^o through to 15^o yaw angle results all predict a similar offset of the peak pressure point to the windward side by 0.04m. This effect was not seen to the same extent at loop location four as that region is still highly influenced by a high pressure bubble that forms between the lower part of the train's nose and the ground surface. On the windward side edge of the front of the train the pressure drop is around twice that seen in loop four. On the leeward side of the train the pressure drop around the side edge is around two and a half times higher than that of the C_p in this location at loop four. This significant decrease in the surface pressures drop around the edges is due to the smaller curve radius higher up at the

front of the train promoting flow separation. On the leeward side of the leading car the four investigated yaw angles produce similar C_p profiles though offset, these values increase along the cars length to around a value of 0.

The C_p profiles on the leeward side of the train are also considerably smaller than those of loop four. Here all four yaw predict similar profiles after the second ICG with just a small offset between the C_p values. After the first ICG both the 10^o and 15^o results show a pressure drop before rising back to just below zero before the third ICG. At the tail of the train the pressure drops on both the leeward and windward sides are now twice the values recorded at loop four, this matches with the larger nose pressure spikes seen at this loop height.

9.2.4. Surface pressure summary

From the results of loops one through to five it can be seen that the most sensitive area to changes in yaw angle is the nose region. Upon the lead car it is the leading edges of the sides that are most sensitive whilst the roof edge shows little variation with yaw angle. These side edges become more sensitive as the height up them increases due to the tightening radius. By the end of the first car little variation exists between the C_p's of the windward side for the different yaw angles. As yaw angle increases the ICG's create larger positive pressure spikes upon the windward side of the train, though these only remain for short period before the surface pressures reduce back down. Upon the leeward side the ICG's create smaller negative pressure spikes, as yaw angle increases it takes increasingly longer for the pressures upon the leeward side of the train to increase back up. Like the nose it is the trailing edges of the tail cars sides that are most sensitive to the changes in yaw angle, though the low pressure spike created within this region is smaller than at the nose.

9.3. Visualisation of surface pressures.

To further investigate the effects of crosswinds upon the surface pressures of the train results for the four investigated yaw angles are visually compared using time averaged surface pressure contours over the whole train. Comparisons are conducted using views of the windward and leeward sides of the train model with the trains front facing out of the paper, and with a view of the trains tail. The pressure contour range used can be seen at the bottom of the figures, the choice to use a range which does not include peak values was made based upon the findings of section 9.2. This range was chosen to produce a balance between showing pressure high points whilst showing the finer details at lower yaw angles and along the sides of the train. By comparing the pressure contours it is possible to see what causes pressure features noted earlier. Furthermore, by viewing pressures over the whole train it shows regions that were not covered by the measurement loops.

9.3.1. Windward side.

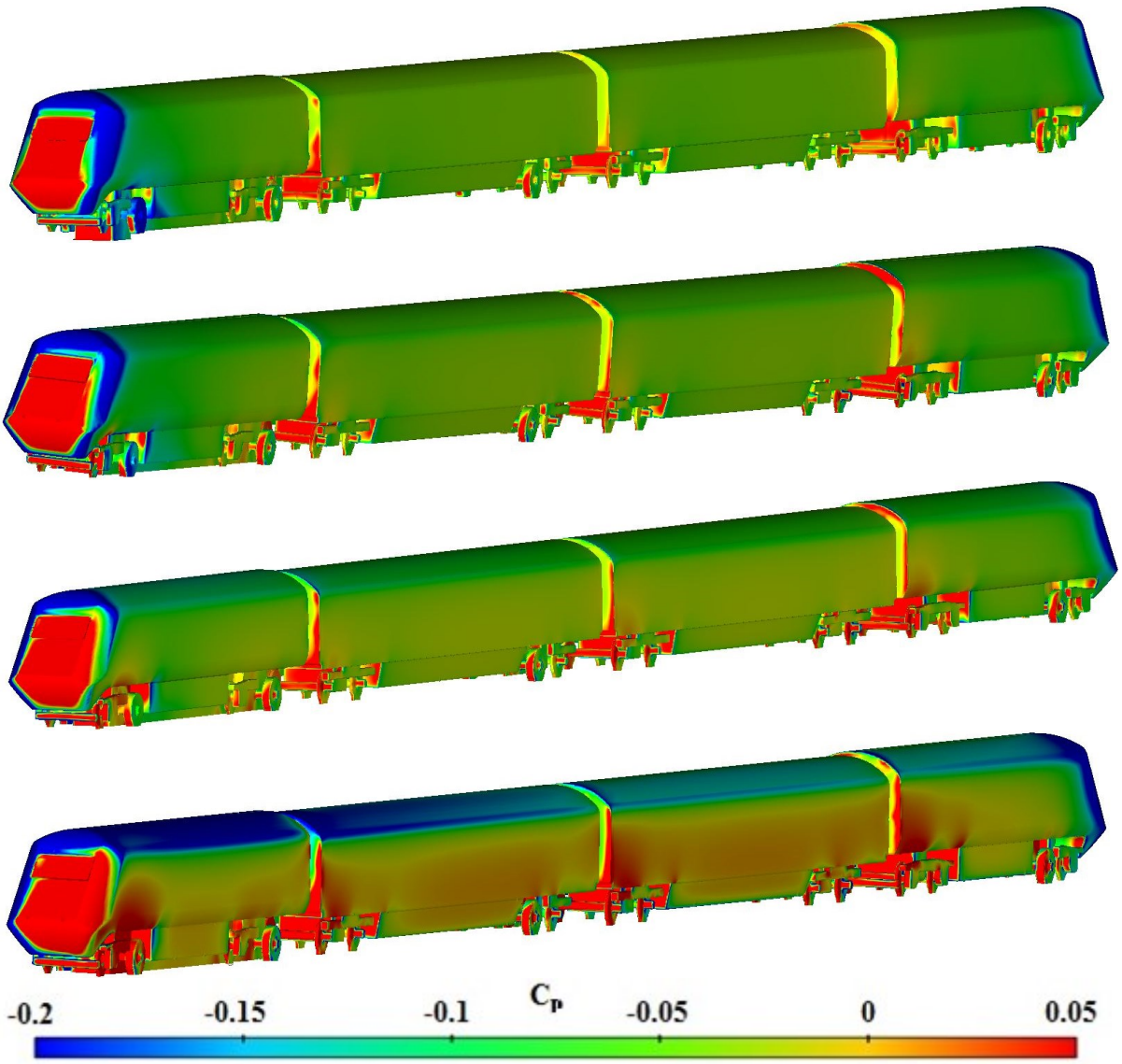

Figure 82: Surface C_p contours for windward side at four investigated yaw angles. Top to bottom = 0^o, 5^o, 10^o and 15^o respectively. Crosswind flow from right to left.

Figure 82 shows the surface pressure contours for the windward side of the train at each yaw angle. On this side of the train the contours show for the most Part pressures are close to or above atmospheric pressure. In the 0^o yaw angle case it can be seen that the front of the train is characterised by a positive pressure region that turns to a negative region at the side and roof leading edges. Each bogie and wheel combo along the trains length features a high

pressure upon its forward face and a pressure of around atmospheric on the sides of all but the first bogie. The sides and wheels of the first bogie show low pressure upon the outside surfaces which causes small low pressure regions on the trains surface above and just after them. At each ICG high pressure regions can be seen at the front face of the next car, this pressure is primarily at the lower corners and is in part be caused by the leading bogie of each car.

At a yaw angle of 5^o the high pressure region moves slightly around the front of the train to the windward side. The low pressure region on the side corner of the train is now decreased in its size, Particularly at the height of the trains nose point and around the windscreen. The low pressure region on the side of the first bogie is also decreased in size. At each ICG the high pressure region now extends higher up the train and can be seen to cause an increase in pressure on the side of the car after it. The tail of the train now shows a considerably larger region of high pressure around the top side of the train, this region exists as the tail car is larger in both height and width than the two preceding passenger cars.

The high pressure region at the front of the train at a yaw angle of 10^o now extends half way around the front corner, the low pressure region on the side of the train only extends from the mid height of the train and up. The front bogie of the train no longer features a low pressure region upon its sides and now causes a higher pressure region to occur on the side of the train above it. The pressures at the front of each car after the ICG are now at a higher pressure with the highest pressure regions now extending higher and further into the ICG. Due to the higher pressures in the ICG and around the bogie region each towed car now shows a high pressure region above its first bogie with the tail car showing the largest of these regions. The two passenger cars now feature a visually higher pressure over their whole windward side.

The 15^{o} yaw angle shows the largest pressure variation as to be expected. The high pressure region at the front of the train now covers a large portion of the front windward corner, especially for the lower half of the train. The low pressure region seen on this corner at smaller yaw angles now only exists in a small region by the roof. The high pressure regions created by each of the first bogies for each of the cars now extends up over half train height. The side of the train now also shows a high pressure region that extends up to near to roof edge. Over the roof of the train there is a significant drop in pressure when compared to the 10^{o} yaw angle. The power cars roof along with the first half of the second car is almost entirely at the minimum pressure visualisation value. The remainder of the roof region shows pressures below atmospheric with the leading and windward side edges near the minimum value visualised.

9.3.2. Leeward side.

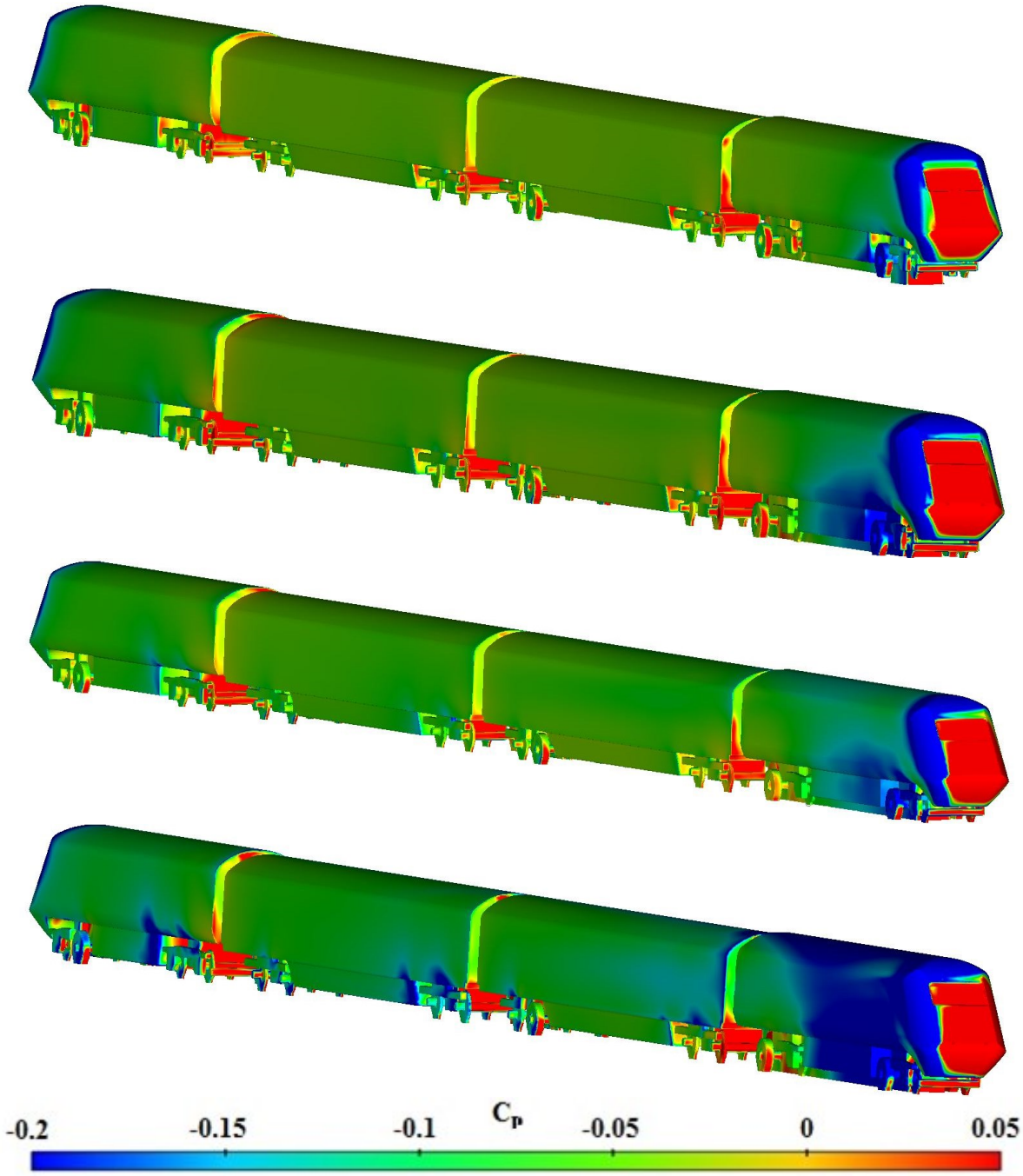

Figure 83: Surface C_p contours for leeward side at four investigated yaw angles. Top to bottom = 0^o, 5^o, 10^o and 15^o respectively. Crosswind flow from right to left.

Figure 83 shows the surface C_p values for the leeward side of the train for the four investigated yaw angles. The pressure contours on the leeward side of the train at 0^o yaw

angle matches that of the windward side as there is no crosswind, so no further comments will be made upon it. At a yaw angle of 5^o the low pressure region on the front corner of the trains side moves in a windward direction so that it is in line with the windscreen edge, the low pressure region also extends further down the corner than at a yaw angle of 0^o. The front lower half of the leeward side of the train is now covered by a low pressure due to the separation that occurs around the sides front edge. Along the second and third cars of the train the pressures are consistent with those seen in the 0^o case. At the tail of the train the final wheel shows a notably lower pressure on its top half.

The 10^o case is similar to that of the 5^o case around the nose of the train, the low pressure region created by separation around the front edge increases in its height with a small region of just below atmospheric pressure extending up to a similar pressure region on the leeward roof edge. Each of the bogie wheels now shows a lower pressure on the upper half when compared to the smaller yaw angles. The start of the undercarriage component geometries for the third and fourth cars (boxes after each cars leading bogie) now show a small low pressure region on the leading edge, on the fourth car this region extends a small distance up onto the side of the train.

As with the windward side it is the 15^o yaw angle that shows the greatest change in predicted surface pressures compared to lesser yaw angles. Around the nose of the train the low pressure region extends further towards the trains centre with the low pressure above the leeward side of the windscreen moving down the train to the wind screens edge. The low pressure region created by recirculation seen in smaller yaw angle results now covers over two thirds of the trains side, this is in part due to the low pressure region that now covers the majority of the leeward side of the roof extending down the trains side. This low pressure region from the roof is created by the large leeward side vortex that separates from the trains

leading roof edge. It is worth remembering that the windward side of the roof was also covered in a low pressure region, confirming that in crosswind situations it is the first car that experiences the largest surface pressure changes.

At the start of the second car just after the first ICG a low pressure region extends up the side edge and around the roofs edge, this low pressure region is created by a second vortex and extends a short distance back along the side and roof of the car. Each of the bogies now creates a small region of low pressure above it whilst pressures on the side of the bogies are decreased with some now at negative values. The side of the three towed cars are all similar pressure to those of the lower yaw angles except for a region extending half way down the second car at mid height, this region is the remains of the low pressure created at the ICG. The smaller low pressure regions noted at 10^{o} at the start of the third and fourth car underbody component geometries are greatly increased in their size extending higher and further along the side of the train.

9.3.3. Tail

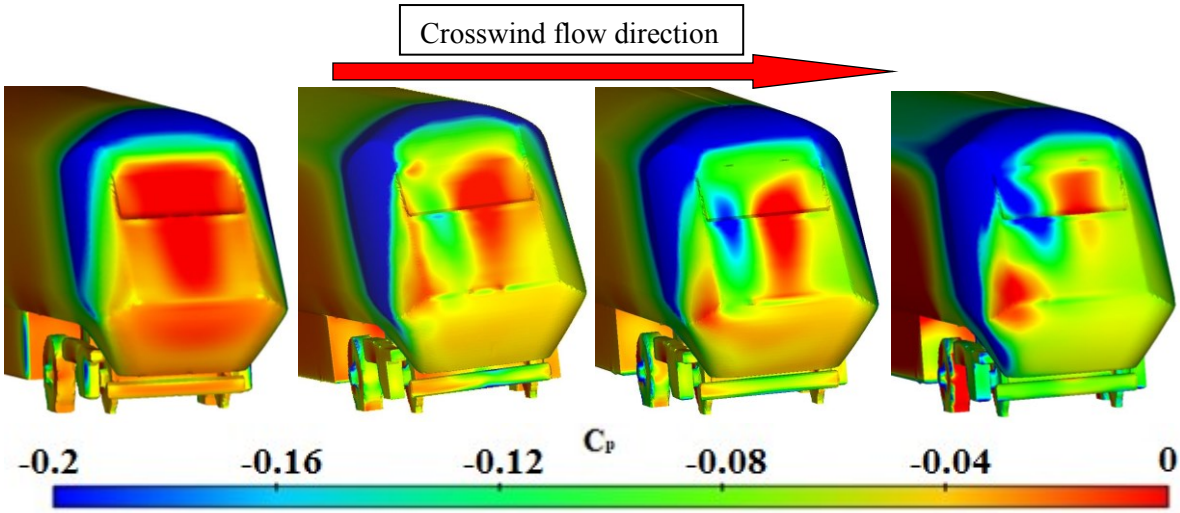

Figure 84: Surface C_p results for the trains tail, 0^{o} – 15^{o} left to right. Crosswind flow from left to right.

Figure 84 shows the surface pressure contours for the tail of the train, the C_p range at this location differs from that of Figure 82 and Figure 83 to improve the visualisation of the lower pressure range. In the no crosswind case the low pressure regions over the side and roof edges can be clearly seen, this is where flow separation occurs as seen in Figure 80 and Figure 81. The majority of the trains tail is just below atmospheric pressure though a central region of just above atmospheric pressure exists, this reasonably high pressure is due to the large amount of flow reattaching to the surfaces after separating around the tail edges. Despite the low pressure seen at 0^o in Figure 67 caused by tail vortices the lower portion of the tail does not show its effects.

At a yaw angle of 5^o the lower portions of the leeward side edge begin to show a lower pressure, the low pressure on the windward side edge, now extends further down and around onto the tail. Pressures upon the tail are considerably lower for the upper half but only slightly lower for the lower half, this is due to the geometry of the tail accelerating flow on the upper half of the train whilst a portion of the flow approaching from the lower section passes through the bogie gap. A low pressure region also begins to form upon the windward side of the windscreen. The leeward side of the tail still features a higher pressure section due to the reattachment of flow that separated off of the windward edges.

At 10^o the tail face shows a larger region of very low pressure at the same location as the small pressure drop at 5^o, this is due to a vortex released from the upper windward edge that travels down towards the main wake vortex seen in Figure 67. The higher pressure region to the leeward side of the tails centre is now more concentrated as is the high pressure region at the mid height on the windward side edge. At 15^o the low pressure regions on the roof and windward side edges grow in size and move around onto the tail face, the region joins with the low pressure region upon the windscreen. The leeward side high pressure region reduces

again in size now only situated upon the windscreen, this suggest less of the flow which separates around the windward edges reattaches back onto the train. The increase in pressure upon the windward corner is linked to increased flow reattachment from the windward edge just prior, this region reduces in size compared to smaller yaw angles but is now at a higher pressure suggesting the reattachment of flow in this region is now more concentrated.

9.4. Surface pressure summary.

Comparison of surface pressures over measurement loops showed that cross wind angles of up to 15^o had a minimal effect on peak C_p values. The largest effect of yaw angle changes was seen on the leeward sides of the train cars. Results also showed that on the windward side of the train there were large pressure spikes measured at each ICG, with the first ICG producing a spike of roughly the same magnitude as the nose region. At the tail of the train a low pressure spike occurs at around two thirds the magnitude of the positive peak pressure of the nose.

Visualisation of surface pressures over the train shows that the most sensitive regions to yaw angles are the leading side edges of the trains nose and the bogie regions. The low pressure region created upon the leeward side of the train becomes a dominant feature at yaw angles as low as 5^o due to the formation of a leeward side vortex. The pressure changes in the bogie region can be seen to cause changes to the pressures within the ICG and also upon the trains side. The roof region of the train remains a reasonably consistent pressure until the 15^o yaw angle results where a large portion of the windward side experiences a below atmospheric pressure, this occurs due to flow separating over the windward edges, the first car experiences the lowest roof pressures with both sides being in the lowest visualised range.

Surface pressures upon the tail of the train show the differences in flow reattachment that occur at each of the yaw angles, as the yaw angles increases less flow can be seen to reattach. The pressures upon the tail of the train generally show little correlation to the wake results shown in Figure 67. Though the low pressure region seen around the windscreen at 10^o and 15^o correlates well with the wake vortex core. The lack of correlation between the surface pressures and wake pressures shows that large pressure changes within this region occur over a very short distance.

9.5. Aerodynamic forces and coefficients

The remainder of this chapter will focus upon the aerodynamic forces and moments of the train. From the analysis of surface pressure results it can be seen that the leading car of the train is the most sensitive to yaw angle changes, therefore it is likely that the first car will also experience the largest changes in aerodynamic forces.

Table 8 shows the drag coefficient and the full scale drag values for each of the trains individual cars plus the combined train, these are shown for each of the four yaw angles investigated. Results obtained from wind tunnel tests of a $1/20^{th}$ scale three car Korean high-speed train in the work of Kwon et al. (2001) show the measured C_d to be around 0.42. This matches well with the results in Table 8 though it suggests that the DDES results are under predicting as it would be expected the C_d of a HST would be higher due to its less aerodynamic shape.

From the results it can be seen that in the no crosswind case both the lead and tail cars of the train produce the highest drag values.

The drag at the leading car is created primarily by the high pressure region ahead of the train whilst the tail of the train produces high levels of drag due to the low pressure region just after it. Of the two passenger cars the first car produces a higher level of drag than the first, this is due to the first passenger car sheltering the second. As yaw angle is increases the combined drag of the train can be seen to increase, this increase is only small between 0^o to 5^o but becomes larger at each incremental step. Due to how the frontal area remains relatively constant with the addition of cars the full train C_d value is the sum of the individual car values. Due to this the addition of extra passenger cars to the train will lead to an increase in the trains C_d value.

The results around the leading car show that yaw angle only causes a comparably small effect upon it. The 10^o yaw angle shows a drop in the drag force for the leading car, this is most likely due to a number of factors including the smaller high pressure region ahead of the train and the first bogie wheel blocking some flow from encountering the launching mechanism. The first passenger car features the lowest drag at a yaw angle of $5^{o,}$ above which the drag increases at an increasing rate. One of the reasons the second, third and fourth cars of the train experience an increase in drag with yaw angle is due to the increased amount of flow that enters the ICG's and encounters the leading faces of following car.

The tail car of the train is responsible for the largest percentage of the combined drag force for the three crosswind cases. This is due to the large very low pressure region upon the rear faces of the train (Figure 84) caused by the accelerated flow around the trailing edges and the leeward side vortex. The high drag levels are also due to the large wake that is drawn along behind the train which increases in width with yaw angle

Table 8: Drag coefficients and full scale drag forces for each car and whole train at each yaw angle.

C_d	Lead car	Passenger 1	Passenger 2	Tail car	Full train
0	0.16	0.08	0.04	0.16	0.41
5	0.16	0.07	0.06	0.19	0.45
10	0.14	0.10	0.12	0.23	0.54
15	0.18	0.23	0.21	0.41	0.93
Drag (KN)	**Lead car**	**Passenger 1**	**Passenger 2**	**Tail car**	**Full train**
0	3.31	1.30	0.71	3.31	8.63
5	3.43	1.06	0.95	3.90	9.33
10	2.95	1.65	2.01	4.73	11.34
15	3.66	3.78	3.43	8.51	19.38

Table 9 shows the full scale lift values for each of the trains individual cars plus the combined lift for the four yaw angles investigated, results for each individual car is calculated using that cars frontal areas. The results within this table appear reasonable and indeed match well at the yaw angles of 0^o and 5^o with the results shown in Cheli et al. (2010), These results were collected during wind tunnel tests conducted upon a $1/10^{th}$ scale two car EMUV250 train where only the lead car was mounted upon a load sensor. At 10^o and 15^o the results in Cheli et al. are larger than those in Table 9, this may in part be due to the more aerodynamic nose shape of the EMUV250 producing more lift.

From the results it can be seen that as yaw angle is increased the lift value increase. From 0^o to 10^o the changes in C_l are relatively small however at 15^o the C_l value is over 2.5 times the magnitude of the 10^o results and four times the magnitude of the 5^o results. Due to the top surface area increasing with the addition of each car the C_l is not a sum total like the C_d but instead is an area weighted average. Due to this the addition of extra passenger cars to the train will likely lead to a decrease in the C_l value, this is assuming that each additional car is similar in forces to that of the second passenger car.

When looking at each individual car for the no crosswind case, the C_l values show that the first three cars are relatively neutral whilst the tail car C_l value is four times greater than that of the nose. This is primarily caused by the low pressure region created over the trailing edges and face of the car which can be seen in Figure 84. The C_l of the tail car increase by only small increments with yaw angle until the 15^o case where the C_l is nearly three times the magnitude of the 10^o results. The large increase in C_l for the 15^o results is due to the acceleration of flow over the roof near the end of the car. This acceleration is caused by the low pressure to the rear and leeward sides of the car, which can be seen in Figure 84.

The results of Table 9 show that the lead car is the largest contributor to the overall lift force when the train experiences a crosswind. For the smaller yaw angles this is due to the low pressure region situated around the leading edges of the train and the high pressure region below the train and in front of the firing mechanism. At a yaw angle of 15^o the lift force increases significantly due to the large region of low pressure over the trains roof as can be seen in Figure 82 and Figure 83. The first of the passenger cars also shows a significant increase in the lift force at a yaw angle of 15^o, this is due to the low pressure from the first car continuing back on to the windward side of the first passenger cars roof as seen in Figure 82. The second passenger car shows a small increase with C_l as yaw angle is increased, the car however is the only to produce a negative lift value in the no crosswind case.

Table 9: Lift coefficients and full scale lift forces for each car and whole train at each yaw angle.

C_l	Lead car	Passenger 1	Passenger 2	Tail car	Full train
0	0.01	0.00	-0.01	0.04	0.01
5	0.06	0.03	0.02	0.05	0.04
10	0.10	0.07	0.03	0.06	0.06
15	0.27	0.17	0.04	0.17	0.16
Lift (KN)	**Lead car**	**Passenger 1**	**Passenger 2**	**Tail car**	**Full train**
0	1.18	0.00	-0.95	3.90	4.14
5	5.67	3.90	1.89	4.49	15.95
10	9.69	8.39	3.19	5.44	26.71
15	25.52	19.38	4.84	15.95	65.70

Table 10 shows the side forces and corresponding coefficients (C_s) for the whole train and each of the cars individually. The results compare well to data collected by Diedrichs (2003) who conducted crosswind CFD simulations upon an ICE2 train at yaw angles of 15^o. Diedrichs results calculated side force coefficients in the range of 0.16 – 0.2 and 0.075 – 0.1 for the first and second cars respectively.

The side forces for the whole train show a large sensitivity to yaw angle changes, with the largest change occurring between 5^o to 10^o. The side forces for each individual car show that the most critical region is the nose. The first car is the most sensitive due to the initial high pressure region ahead of the train as seen in chapter 7, the high pressure region created to the side and on any nearby surfaces of the first bogie (Figure 82), the large separation region that occurs on the lower leeward side around the first bogie and the leeward side roof vortex that forms at higher yaw angles (Figure 59). The first and second passenger cars show similar results to each other at the 5^o and 15^o results but differ quite significantly from each other at

10^{o}. This is due to the formation of a vortex released from the third car at this yaw angle, this leads to the leeward side pressure difference seen in Figure 81.

The tail of the train shows negative (towards windward) sideways forces for both the 5^{o} and 15^{o} yaw angles, this is due to the low pressure that occurs around the windward side trailing edge of the car. The 10^{o} results show a positive sideways force, this occurs due to an imbalance between the lack of growth of the low pressure region on the leeward trailing edges of the train, the growth in the low pressure region on the leeward side of the train and high pressure regions to the windward side.

Table 10: Force coefficients and full scale forces for each car and whole train at each yaw angle.

C_s	Lead car	Passenger 1	Passenger 2	Tail car	Full train
0	0.00	0.00	0.00	0.00	0.00
5	0.06	0.00	0.00	-0.01	0.01
10	0.11	0.02	0.04	0.02	0.05
15	0.18	0.06	0.07	-0.10	0.05
Side (KN)	**Lead car**	**Passenger 1**	**Passenger 2**	**Tail car**	**Full train**
0	0.00	0.00	0.00	0.00	0.00
5	7.86	0.27	0.09	-1.13	6.9
10	15.83	4.26	7.56	2.48	30.1
15	24.84	11.08	11.35	-14.56	32.7

Table 11 shows the overturning moment and the corresponding coefficient for the whole train and each individual car at each of the four investigated yaw angles. The overturning moment is measured as the force acting upon the leeward rail and is calculated using the equation:

$$C_{lee} = C_m - \frac{d_g}{l} C_l \quad (45)$$

Where:

C_m = Coefficient of roll Moment about the COT position.

l = train reference length

d_g = Track gauge

The results for the whole train show that as yaw angle is increased the overturning moment increases. The initial increase between 0^o and 5^o is considerably larger than that of the increase between 5^o and 10^o, this is primarily due to the tail of the train which switches from a positive over turning moment (rolling to the leeward side) to a negative roll moment (rolling towards windward). This change in the roll moment direction is a result of the increase in the size and magnitude of the low pressure regions to the upper windward side of the tail car that exceed the increase in negative pressure on the leeward side. This effect continues between 10^o and 15^o yaw angles where the overturning moment increases by nearly 600%. The overturning moment results for the first and second passenger cars show that with each 5^o increase in yaw angle above 5^o the moment doubles.

The second passenger car experiences a smaller overturning moment than that of the first due to the lower pressure around the start of the first passenger car on the leeward side, this low

pressure can be clearly seen in the 15° yaw angle results of Figure 83. The lead car of the train shows the largest independent over turning moment for the 10° and 15° yaw angles. This is due to the large high pressure region that moves to the windward side of the train, the increase in the low pressure regions size and magnitude on the lower leeward side and the formation of a low pressure vortex at the upper leeward side of the train.

Table 11: Full scale overturning force and overturning coefficient values for each car and whole train measured upon the leeward rail at each yaw angle.

Overturn coefficient	Lead car	Passenger 1	Passenger 2	Tail car	Full train
0	-0.003	0.003	0.002	0.005	-0.002
5	0.036	0.016	0.015	0.052	0.028
10	0.140	0.032	0.027	-0.032	0.040
15	0.399	0.065	0.047	-0.212	0.067
Overturn force (KN)	Lead car	Passenger 1	Passenger 2	Tail car	Full train
0	-0.2	0.2	0.1	0.4	-0.8
5	5.6	3.2	2.8	7.6	19.3
10	20.4	6.5	5.0	-3.9	27.7
15	57.9	13.4	8.7	-28.0	50.7

9.6. Conclusion

The results for the surface pressures showed that the lead car of the train is the most sensitive to changes in yaw angle, this sensitivity is primarily due to the leeward side vortex that forms near the roof and the lower recirculation region that occurs from the first bogie. The windward side of the first car only sees high pressures occur upon the leading edge and around the first bogie with the remainder of the cars side at around atmospheric pressure. The pressure over roof of the train decreases as yaw angle is increased, by 15° the entirety of the

roofs surface is below atmospheric pressure with the large majority below a coefficient value of -0.2.

For the remainder of the train the leeward side experiences larger variations in the surface pressures with changes in yaw angle. The windward side of the train is less sensitive with only smaller pressure increases with yaw. Each ICG causes an increase in surface pressure upon the car directly after. Pressures upon the forward facing surfaces of the bogies are above atmospheric and do not vary significantly with yaw angle. Both the windward and leeward sides of the bogies remain just below atmospheric pressure at all four yaw angles investigated.

The results from the aerodynamic forces study shows that as yaw angle is increased all aerodynamic forces increase. The drag force increases gradually up until the 15^{o} yaw angle where the drag near doubles in magnitude over the 10^{o} results. The lift forces are more sensitive to changes in yaw angle than drag. The side force upon the train shows a high rate of increase up to the 10^{o} yaw angle after which the rate of increase drops. Unlike the side force the rate at which the overturning moment increases at raises with yaw angle, this is due to the Centre of Pressure (CoP) height increasing with yaw angle.

Results for each car showed that the two passenger cars are the smallest contributors to aerodynamic forces and vary the least with yaw angle. As yaw angle increases the tail car becomes responsible for a larger percentage of the sum drag. The lead car is responsible for the largest percentage of the lift, side and overturning moments. The side force and overturning moments for the tail of the train are to the windward direction whilst the rest of the train is to the leeward direction, this was attributed to the low pressure region on the windward trailing edges of the train caused by the acceleration of flow around them.

Chapter 10. Comments and recommendations on TSI and CEN requirements.

10.1. Introduction.

The main aim of this research was to investigate the effects of crosswinds on a high-speed passenger trains slipstream. To achieve this it was first necessary to conduct test cases in an attempt to optimizing the final case setup. During these test cases some of the relevant TSI and CEN requirements in place for the investigation of external flow around high-speed passenger trains were also investigated. The findings of these test cases, along with the findings from the crosswind research enabled the following comments and recommendations to be made on current regulations.

10.2. Testing methods.

- Chapter 5.3.4 of the CEN specifies the computational domain requirements for conducting CFD simulations. The regulations state a STBR setup must be used with a ballast height of 0.825m, although this setup was not tested a similar ballast height of 0.75m was. Simulations were also conducted using a lower ballast height of 0.3m and a flat ground case to analyse the effect of ballast height. Results showed that as the ballast height was decreased the slipstream of the train propagated further away from the train resulting in higher velocities at measurement locations. From these findings it is would recommend that model scale and CFD testing should be conducted on the worst case scenario of a flat ground to ensure accurate slipstream characteristic maximums are recorded.

- Section 4.2.6.2.1 of the TSI provides regulations for the testing setup and maximum values acceptable for aerodynamic loads on track workers at the lineside. The regulations state that tests to check the conformity of a train to the maximum permissible trackside air speed and pressure changes must be conducted with ambient wind speeds of less than 2 m/s. Results from chapter 8 show that for the train shape investigated results from crosswind cases up to 15^{o} (15 m/s winds at a perpendicular angle to train) still comply with the regulation limits. Due to this it is the authors' recommendation that as long as measurements are conducted upon the leeward side of the train the requirements for ambient wind speeds of less than 2 m/s should be relaxed, this would allow train testing to be conducted without the need to wait for a day with little to no wind.

- Section 4.2.6.2.3 of the TSI provides regulations for the testing setup and the maximum values acceptable for pressure load in open air. The regulation states that in order to check the conformity of a train to the maximum permissible trackside air speed and pressure changes the tests are to be conducted upon a ballasted track of height 0.75m ± 0.25m. Results from chapter 5 show that a larger ballast height allows the strongest part of the slipstream to pass below the measurement points, though this may not be the case for trains where the nose geometry does not act to direct the initial flow downward. The use of a flat ground setup during model scale and CFD tests and a smaller ballast height during full scale test would help negate this effect, potentially making the testing procedure fairer and leading to overall safer train designs.

- Section 4.2.6.2.3 of the TSI also states measurements to check the conformity of a train to the maximum permissible pressure changes should be conducted at heights of 1.5 – 3.3m above TOR at 0.3m increments. This along with the requirement for data to

be collected from over ten runs or ten spaced out measurement locations is potentially inefficient. Results from chapters 7 and 8 show that as height above the rail increases the pressures produced at the nose of the train decrease, this may not be the case for entirely different geometries such as a freight train but is likely to be the case for all aerodynamically shaped geometries. It is therefore possible that tests could instead be conducted using only one to three measurement heights with 1.5m being the most important for passenger trains.

10.3. CFD turbulence modelling.

- Chapter 5.3.6 of the CEN standards specifies the turbulence modelling requirements for CFD simulations. The regulations state that only two equation or greater turbulence models should be used. Research conducted investigating the most common one equation turbulence model. the S-A turbulence model. Results for surface pressures and aerodynamic forces agreed that this turbulence model is indeed not suitable for application to external flows around trains due to its lack of accuracy.

- Chapter 5.3.6 of the CEN also states that k-ε based turbulence models are not suitable due to the need to use wall functions to achieve a natural wall normal behaviour. Results presented within chapter 4 confirm that k-ε based turbulence models are not ideal, even with the use of wall functions. Their accuracy for both surface pressures and aerodynamic forces is not much higher than that of the S-A turbulence model and notably less than the SST k-ω turbulence model.

- Chapter 5.3.6 of the CEN also states that DES based approaches are suitable assuming validation is provided. Research conducted shows that a DES based approach is constantly more accurate than a RANS approach with any of the investigated turbulence models. Results show that the DDES approach is able to produce a further improvement in obtainable accuracy over the standard DES approach. Therefore the additional requirement for validation with this approach is not appropriate. Furthermore any simulation planned to be conducted with the DES approach should use the DDES approach if it is available within the software, this approach was shown to lead to an increase in accuracy with no discernible increase in computational time.

10.4. Potential additions to CEN

From the findings of chapter 7 the following recommendations can be made as potential additions section 5.2.3 of part 6 of the CEN (2010). This part of the CEN specifies requirements for simulations by CFD to assess crosswind stability of vehicles.

- From the results in chapter 5.3 it can be determined train length should be at least four cars to enable the slipstream to stabilise prior to the tail car. As the slipstream is stabilised by the third car there is the potential that any additional cars would also produce the same aerodynamic forces. If this is the case then the aerodynamic forces from the third car could be used for additional cars, this would enable approximations to be made on the aerodynamic forces acting upon longer train lengths. This would require further testing of at least three, five and six car lengths and test for additional geometries to ensure this theory is correct. Testing along these lines was conducted in

Muld et al. (2012) where two, three and four car length trains were investigated, the results did show some variation in the slipstream thickness.

- Overturning moments and forces should be considered for at least both the lead and tail cars. This is based off of the findings in chapter 7 where the tail car of the train had a large overturning moment that was opposite to that of the nose. Whilst the passenger cars had only smaller overturning moments.

Chapter 11. Conclusions and recommendations on future work.

11.1. Conclusions

This chapter evaluates whether the aim of the research was achieved by examining if the research objectives were met. The aim of the research within this thesis was to provide an improved understanding of the aerodynamic characterisation of a high-speed passenger train and how these characteristics are affected by crosswinds at yaw angles of up to 15^{o}.

Objective 1:

Investigate the effect different steady state RANS turbulence models and DES based approaches produce upon surface pressure predictions of a high-speed passenger train at a scale of $1/25^{th}$ without crosswind, and to compare the results with wind tunnel data for the equivalent case to determine which approach best describe the flow around trains.

- Aerodynamic drag predictions from seven different CFD approaches were compared to experimental drag results. Results showed that the DDES approach best matched the experimental results with the DES and SST k-ω models also producing close predictions.

- Aerodynamic lift predictions from the same seven CFD approaches proved to be less accurate. The DES approach produced the closest results, followed by the DDES approach and the SST k-ω turbulence model.

- Visual comparison of seven CFD approaches to experimental results showed the DDES approach best replicated pressure peaks.

- Comparisons of surface pressures via three methods of assessment showed the DDES approach to produce the highest level of accuracy when compared to experimental measured pressures.

Objective 2:

By comparing to experimental data, determine the accuracy of the DDES approach for predicting velocity and pressures profiles within the train's slipstream at varying ballast heights of 0m (flat ground), 0.3m and 0.75m.

- Pressures and velocities were compared along a measurement location within the trains slipstream, these comparisons were conducted for all three ballast heights. Results showed that pressures within the slipstream remained at a constant level of accuracy as ballast height increased

- Results showed the velocity accuracy decreased as ballast height increased, primarily around the second car. Overall results showed good correlation at all three ballast configurations.

Objective 3:

Determine the effect of ballast shoulder height on the velocities and pressures around a high-speed passenger train, using the DDES approach. Comparing the three ballast shoulder heights investigated of 0m (flat ground), 0.3m and 0.75m to each other.

- Pressure comparisons conducted along four measurement locations within the slipstream showed ballast height had no discernible effect upon measured values.

- Velocity comparisons concluded along the same four measurement locations showed that as ballast height was increased the velocities within the slipstream decreased. Initial velocity peaks caused by the nose were unaffected

- Visual analysis of the slipstream upon the ballast side of the train showed two vortices are formed, one being situated along the ground plane and the second high up on the trains side. As ballast height is increased the location of the upper vortex does not vary with ballast height. The lower vortex moves down the ballast side due to the Coandă effect, in turn passing below the measurement locations.

Objective 4:

By comparing to experimental data, determine the accuracy of the DDES approach at predicting surface pressures at yaw angles ranging from 5 ^{o} to 15^{o} when compared to experimental results.

- Comparisons of the aerodynamic drag forces between CFD and wind tunnel (RWDI) tests show good correlation at the yaw angles of 5^{o} and 15^{o} where the CFD results are within 10% of the experimental results. The results at 0^{o} showed a large over prediction of the drag force, this was attributed to the addition of the firing mechanism geometry. The 10^{o} results show a large variation but this time under predict the drag force by nearly 20%. This variation was attributed to the leading parts of the bogie geometry in the CFD simulation providing shelter for other parts of the bogie at this yaw angle.

- Comparisons of the aerodynamic lift forces between CFD and wind tunnel (RWDI) tests show more consistent results between the two approaches at angles up to 10^{o}. At 15^{o} the CFD results show a considerably larger lift force. This was attributed to variations in the roof pressures between the two approaches and a lack of measurement taps within the underbody of the experimental model.

- Comparisons of surface pressures over loops around the train showed good correlation between the two approaches at all but regions where large peaks and/or rapidly changing pressures occurred.

Objective 5:

Investigate the pressure, velocity and flow feature changes that occur within the slipstream of a high-speed passenger train as the yaw angle increases from 0^{o} to 15^{o} in 5^{o} increments.

Pressure:

- As yaw angle increases the region of low pressure around the leeward side of the nose increases in both size and magnitude. The windward side of the nose sees a reduction in the size of the low pressure region as yaw angle is increased.

- Over the roof of the first car a negative pressure region begins to form between 5^{o} and 10^{o}. This is due to flow separating over the roofs leading edge. At 15^{o} this region joins a low pressure region which covers the windward half of the roof for the entirety of the train's length. This additional low pressure region is created by flow accelerating over the windward edge.

- At 10^o a separated leeward side vortex forms, this vortex's core is within the C_p visualisation threshold of -0.075. At 15^o the volume of this region increases in size significantly with a pressure coefficient at the core of below -0.2.

- At the tail of the train the low pressure region created by accelerated flow moves to the windward side as yaw angle is increased.

- Within the wake the low pressure region moves upward and in a windward direction as yaw angle is increased from 0^o to 5^o. The position of this vortex remains constant at 10^o but moves nearer to the centre and higher at 15^o.

Velocity

- Ahead of the trains nose a high velocity region exists due to air being pushed forward. As the yaw angle is increased this region moves to the windward side of the train.

- As yaw angle increases the region of the slipstream upon the windward side of the train with a normalised velocity above the visualisation value of 0.25 decreases in size, this effect is most prominent on the flow released from the underbody region.

- The region of the slipstream upon the leeward side of the train with a normalised velocity above 0.25 grows in size as yaw angle is increased. Again this effect is most prominent on the flow released from the underbody region.

- Upon the leeward side roof edge of the train a region of higher velocity flow forms at 5^o. At 10^o and 15^o this region of high velocity is at the core of a vortex.

- Within the wake, yaw angle does not cause a significant effect upon velocities until 10^{o}. As yaw angle is increased the high velocity region increases in height on the leeward side of the train.

- As yaw angle is increased the velocity within the lower leeward side of the wake increases and the whole wake is moved towards the leeward side.

Flow features.

- As yaw angle in increased the amount of flow that separates from the leeward edge of the roof increases. At 0^{o} a small vortex exists around this location, as the yaw angle increases the vortex increases in size and begins to separate earlier from the train's surface.

- The windward side of the train features a vortex along the roofs edge in the no crosswind case. However at yaw angles of 5^{o} and above this vortex no longer forms.

- Along the ground plane a vortex is created upon each side of the train by the underbody geometry. Upon the leeward side at yaw angles above 5^{o} this vortex dissipates by the second car. Upon the windward side this vortex exists within the 5^{o} yaw angle case until the mid-point of the third car. At higher yaw angles it dissipates by the end of the first car.

- Within the wake the two counter rotating vortices that occur at 0^{o} yaw angle are significantly affected by increases in yaw angle. As yaw angle increases the windward vortex moves higher up, whilst the leeward vortex moves across towards the trains centre and slightly under the windward vortex.

Objective 6:

Investigate the surface pressure and aerodynamic force changes that occur upon a high-speed passenger train as the yaw angle increases from 0^o to 15^o in 5^o increments.

Surface pressures.

- Increases in yaw angle lead to generally higher surface pressures upon the windward side and lower upon the leeward side.
- The roof peak pressure drop over the nose shows little variation between the no crosswind and 15^o yaw angle cases.
- As yaw angle increases a large low pressure peak forms at the lower leeward edge of each car. This peak increases in magnitude between 5^o and 10^o but does not increase between 10^o and 15^o.
- As yaw angle increases the inter carriage gaps cause increasingly larger spikes in surface pressure upon the windward side of the train. Upon the leeward side they cause comparably smaller low pressure spikes.
- The largest low pressure peak occurs upon the leading leeward edge of the lead car. the size of the pressure drop increase with height up the cars side due to the tighter radius.

Aerodynamic forces.

- The results showed that as the yaw angle increased between 0^o and 10^o there was only a small increase in the measured drag, but between 10^o and 15^o this value nearly doubles.

- At all yaw angles the tail car is responsible for more drag than the leading car, as yaw angle increases the difference between the two becomes larger. At 0^o the tail car of the train produces the same amount of drag as the trains leading car. At 5^o the tail car produces 20% more drag than the lead car and by 15^o this difference increases up to 150%.

- Lift results showed that the train is nearly aerodynamically neutral at 0^o, as yaw angle increases so does the trains lift. Between 10^o and 15^o there is a large jump in the lift force due to the low pressure over the roofs of the cars.

- The lead car of the train is the main producer of lift with the second car being the second largest producer. this is due to the lower pressures over the roof of these two cars due to flow separating over the roofs leading edge.

- The side force increases with yaw angle, the largest increase occurs between 5^o and 10^o due to the formation of a leeward vortex.

- The lead car of the train is the most affected by yaw angle, the second and third cars do not show significant sensitivity until 10^o.

- The side force at the tail of the train fluctuates between positive and negative as yaw angle increases due to varying imbalances in flow structures within this region.

- The overturning moment increases with increases in yaw angle, the lead car is the most sensitive to changes in yaw angle.

- At 10^o and 15^o yaw angles the tail car shows a negative overturning moment, this is due to high velocities around the upper windward trailing edge creating low pressures.

Objective 7:

Make comments and recommendations on TSI and CEN requirements.

- CFD simulations were conducted to investigate if crosswinds cause the slipstream velocity to exceed limits, results showed that even at a yaw angle of 15^{o} slipstream velocities did not exceed limits for this train type.

- CFD simulations were conducted to investigate if crosswinds cause the peak to peak slipstream pressures to exceed limits, results showed that at a yaw angle of 15^{o} the value was close but did not exceed limits for this train type.

- A total of nine points are raised in regards to regulations. The most important of which were:

The need for prior validation prior to using the DES based CFD approach is unfounded as in all comparisons it proved more accurate than any of the tested RANS approaches.

The need for a train to be comprised of at least four cars when testing crosswinds, this is to enable the slipstream to fully develop prior to the tail car.

Testing for velocities within the slipstream should be conducted upon the smallest ballast possible to ensure the slipstream does not pass under the measurement location.

11.2. Recommendations for future work

As with all research a target end point must be set that is feasible within the time constraints. However, if more time was available or a new research project was to be based off of the findings presented within this work there are a number of different research topics that would be beneficial to the overall aim of this research. These are listed below;

- Effects of ballast height on crosswind results.

Research conducted within chapter 5 showed that ballast height had an effect upon the slipstream of a high-speed passenger train when no crosswinds were present. Ballast height could potentially cause an even more significant effect when crosswinds are included. Additional research could investigate the effects on the train slipstream when ballasts of different height are placed upon either the windward, leeward or both sides of the train. Due to the large number of possible combinations between yaw angle and ballast configuration it would be necessary to implement a design of experiments approach or similar, though the chosen approach would likely need validation.

- Effects of train length on slipstream growth during crosswinds.

The majority of the results in chapters 7 and 9 show that by the third car of the train, the time averaged slipstream begins to stabilise. The assumption was proposed that this will likely continue for any additional cars assuming their geometry is consistent. This is important as the third car of the train causes the smallest force coefficient values, if additional cars produce similar force values the overturning and lift force coefficients for a full train will decrease with train's length. As with the previous point there are multiple combinations of train length and crosswind angle that would need to be tested. The findings of this would not only be

important for CFD simulations but also model scale tests where the length of the train can be limited by factors such as wind tunnel size.

- The use of LES instead of DDES.

Accuracy of the results obtained when compared to experimental work could potentially be improved through the use of a pure LES approach. This could potentially increase the accuracy as all but the smallest flow scales would be resolved. This is unlike the DDES approach where a less accurate RANS modelling approach was used for the near wall regions. The LES approach however requires considerably higher computational requirements than that of the DDES approach. Therefore, it would not be feasible to produce the presented work within time frame available. A LES simulation could be run to see if an increase in accuracy is obtainable, after this the choice as to which cases to study would need to be based upon their perceived importance.

- Investigation of yaw angles above 15^{o}.

Further research could look at crosswind yaw angles greater than 15 degrees to further investigate how the flow fields around the train change as the yaw angle increases. It is expected that the leeward vortices mentioned within this research will be released earlier from the trains surface, this will likely create larger regions of low pressure on the leeward side of the train which will also increase the overturning moment acting upon the train. To investigate these larger yaw angles new meshes would likely be required to ensure all key flow features are within the regions of higher mesh density.

- Effect of a turbulent inlet condition on the accuracy of the results.

Chapter 6 compares the accuracy of surface pressures calculated through the use of CFD to experimental results collected during wind tunnel and moving model tests. Though the exact accuracy of these results was hard to determine due to geometric differences and limited datum points, the application of a mapped turbulent inlet condition could potential increase the accuracy of the CFD simulations further due to the effects of turbulence on flow separation. To implement a mapped inlet turbulent condition would require an extensive amount of work. Firstly the data must be mapped from the crosswind generator for multiple seconds at a spread of measurement locations. Secondly the mapped inlet condition will need programing into the OpenFOAM software before being validated against additional experimental measurement points.

References

ASHFORD, G. A. 1996. An unstructured grid generation and adaptive solution technique for high-Reynolds-number compressible flows [Online]. Accessed 01/05/2016. Available: http://books.google.com/books?id=OcUeAQAAMAAJ.

AXERIO-CILIES, J. & IACCARINO, G. 2012. An aerodynamic investigation of an isolated rotating Formula 1 wheel assembly. *Journal of Fluids Engineering*, 134, 121101.

BAKER, C.J, 1985. The determination of topographical exposure factors for railway embankments. *Journal of Wind Engineering and Industrial Aerodynamics*, 21, 89-99.

BAKER, C.J, 2010. The flow around high-speed trains. *Journal of Wind Engineering and Industrial Aerodynamics*, 98, 277-298.

BAKER, C.J, DALLEY, S., JOHNSON, T., QUINN, A. & WRIGHT, N. 2001. The slipstream and wake of a high-speed train. *Proceedings of the Institution of Mechanical Engineers, Part F: Journal of Rail and Rapid Transit*, 215, 83-99.

BAKER, C.J, & HUMPHREYS, N. 1996. Assessment of the adequacy of various wind tunnel techniques to obtain aerodynamic data for ground vehicles in cross winds. *Journal of Wind Engineering and Industrial Aerodynamics*, 60, 49-68.

Baker, C.J., Quinn, A., Sima, M., Hoefener, L. and Licciardello, R., 2014. Full-scale measurement and analysis of train slipstreams and wakes. Part 1: Ensemble averages. *Proceedings of the Institution of Mechanical Engineers, Part F: Journal of Rail and Rapid Transit*, *228*(5), pp.451-467.

BAKER, C.J, STERLING, M., JOHNSON, T., FIGURA-HARDY, G. & POPE, C. The effect of crosswinds on train slipstreams. *International Conference on Wind Engineering*, Cairns, Australia, 2007.

BELL, J., BURTON, D., THOMPSON, M., HERBST, A. & SHERIDAN, J. 2014. Wind tunnel analysis of the slipstream and wake of a high-speed train. *Journal of Wind Engineering and Industrial Aerodynamics*, 134, 122-138.

BOCCIOLONE, M., CHELI, F., CORRADI, R., MUGGIASCA, S. & TOMASINI, G. 2008. Crosswind action on rail vehicles: wind tunnel experimental analyses. *Journal of Wind Engineering and Industrial Aerodynamics*, 96, 584-610.

BROCKIE, N. & BAKER, C. 1990. The aerodynamic drag of high-speed trains. *Journal of Wind Engineering and Industrial Aerodynamics*, 34, 273-290.

BUCCOLIERI, R. & SABATINO, S. D. 2011. MUST experiment simulations using CFD and integral models. *International Journal of Environment and Pollution*, 44, 376-384.

CEN 2010. Part 6: Requirements and test procedures for cross wind assessment.

CEN 2011. Railway applications - Aerodynamics - Part 4: Requirements and test procedures for aerodynamics on open track.

CHELI, F., RIPAMONTI, F., ROCCHI, D. & TOMASINI, G. 2010. Aerodynamic behaviour investigation of the new EMUV250 train to cross wind. *Journal of Wind Engineering and Industrial Aerodynamics*, 98, 189-201.

CHIU, T. & SQUIRE, L. 1992. An experimental study of the flow over a train in a crosswind at large yaw angles up to 90. *Journal of Wind Engineering and Industrial Aerodynamics*, 45, 47-74.

COURANT, R., FRIEDRICHS, K. & LEWY, H. 1928. Über die partiellen Differenzengleichungen der mathematischen Physik. Mathematische annalen, 100, 32-74.

COX, W.M. and TIKVART, J.A., 1986. Assessing the performance level of air quality models. In *Air Pollution Modeling and Its Application V* (pp. 425-440). Springer US.

DIEDRICHS, B. 2003. On computational fluid dynamics modelling of crosswind effects for high-speed rolling stock. *Proceedings of the Institution of Mechanical Engineers, Part F: Journal of Rail and Rapid Transit*, 217, 203-226.

DIEDRICHS, B. 2010. Aerodynamic crosswind stability of a regional train model. *Proceedings of the Institution of Mechanical Engineers, Part F: Journal of Rail and Rapid Transit*, 224, 580-591.

FLYNN, D., HEMIDA, H., SOPER, D. & BAKER, C. 2014. Detached-eddy simulation of the slipstream of an operational freight train. *Journal of Wind Engineering and Industrial Aerodynamics*, 132, 1-12.

FLYNN, DOMINIC. 2015. A numerical investigation of the effect of crosswinds on the slipstream of a model-scale freight train and associated effects. Ph.D. thesis, University of Birmingham.

GUILMINEAU, E., DENG, G. & WACKERS, J. 2011. Numerical simulation with a DES approach for automotive flows. *Journal of Fluids and Structures*, 27, 807-816.

HEMIDA, H., BAKER, C. & GAO, G. 2012. The calculation of train slipstreams using large-eddy simulation. *Proceedings of the Institution of Mechanical Engineers, Part F: Journal of Rail and Rapid Transit*, 0954409712460982.

HEMIDA, H., BAKER, C. & GAO, G. 2012. The calculation of train slipstreams using large-eddy simulation. *Proceedings of the Institution of Mechanical Engineers, Part F: Journal of Rail and Rapid Transit*, 0954409712460982.

HEMIDA, H. & KRAJNOVIC, S. 2009. Exploring flow structures around a simplified ICE2 train subjected to a 30 degree side wind using LES. *Journal of Engineering Applications of Computational Fluid Dynamics*.

HERTWIG, D., EFTHIMIOU, G. C., BARTZIS, J. G. & LEITL, B. 2012. CFD-RANS model validation of turbulent flow in a semi-idealized urban canopy. *Journal of Wind Engineering and Industrial Aerodynamics*, 111, 61-72.

HUANG, S., HEMIDA, H. & YANG, M. 2016. Numerical calculation of the slipstream generated by a CRH2 high-speed train. *Proceedings of the Institution of Mechanical Engineers, Part F: Journal of Rail and Rapid Transit*, 230, 103-116.

HUNT, G. B. & ROSS, D. L. 1988. Comparison of effects of three anesthetic agents on induction of ventricular tachycardia in a canine model of myocardial infarction. Circulation, 78, 221-226.

IM, H.-S. & ZHA, G.-C. 2011. Delayed detached eddy simulation of a stall flow over NACA0012 airfoil using high order schemes. AIAA Paper, 1297, 2011.

ISSA, R. I. 1986. Solution of the implicitly discretised fluid flow equations by operator-splitting. *Journal of Computer Physics*, 62, 40-65.

JOHNSON, T. 2006. Aerodynamic influences of vehicle design on wheel/rail contamination. RRSB. Derby.

JONES, W. P. & LAUNDER, B. E. 1972. The prediction of laminarization with a two-equation model of turbulence. *International Journal of Heat and Mass Transfer*, 15, 301-314.

JÖNSSON, M. 2010. Numerical investigation of the flow underneath a train and the effect of design changes. Luleå University of Technology.

KHIER, W., BREUER, M. & DURST, F. 2000. Flow structure around trains under side wind conditions: a numerical study. *Computers & Fluids*, 29, 179-195.

KOLMOGOROV, A. N. The local structure of turbulence in incompressible viscous fluid for very large Reynolds numbers. Dokl. Akad. Nauk SSSR, 1941. JSTOR, 301-305.

KRAJNOVIĆ, S., RINGQVIST, P., NAKADE, K. & BASARA, B. 2012. Large eddy simulation of the flow around a simplified train moving through a crosswind flow. *Journal of Wind Engineering and Industrial Aerodynamics*, 110, 86-99.

KWON, H. & PARK, C. An experimental study on the relationship between ballast flying phenomenon and strong wind under high-speed train. *Proceedings of the World Congress on Rail Research*, Montreal, Canada, 2006.

KWON, H.-B., PARK, Y.-W., LEE, D.-H. & KIM, M.-S. 2001. Wind tunnel experiments on Korean high-speed trains using various ground simulation techniques. *Journal of Wind Engineering and Industrial Aerodynamics*, 89, 1179-1195.

LAUNDER, B. E. & SPALDING, D. 1974. The numerical computation of turbulent flows. *Computer methods in applied mechanics and engineering*, 3, 269-289.

LeVeque, R.J., 2002. *Finite volume methods for hyperbolic problems* (Vol. 31). Cambridge university press.

LI, T., ZHANG, J.-Y. & ZHANG, W.-H. 2013. A numerical approach to the interaction between airflow and a high-speed train subjected to crosswind. Journal of Zhejiang University SCIENCE A, 14, 482-493.

MADDOX, S., SQUIRES, K., WURTZLER, K. & FORSYTHE, J. 2004. Detached-Eddy Simulation of the Ground Transportation System. In: MCCALLEN, R., BROWAND, F. & ROSS, J. (eds.) The Aerodynamics of Heavy Vehicles: Trucks, Buses, and Trains. Springer Berlin Heidelberg.

MENTER, F. & ESCH, T. Elements of industrial heat transfer predictions. 16th Brazilian Congress of Mechanical Engineering (COBEM), 2001. 26-30.

MENTER, F. & KUNTZ, M. 2004. Adaptation of eddy-viscosity turbulence models to unsteady separated flow behind vehicles. The aerodynamics of heavy vehicles: trucks, buses, and trains. Springer.

MENTER, F. R. 1993. Zonal two equation k-turbulence models for aerodynamic flows. AIAA Paper, 2906, 1993.

MORDEN, J. A., HEMIDA, H. & BAKER, C. J. 2015. Comparison of RANS and Detached Eddy Simulation Results to Wind-Tunnel Data for the Surface Pressures Upon a Class 43 High-Speed Train. *Journal of Fluids Engineering*, 137, 041108.

MORTON, S. A., STEENMAN, M. B., CUMMINGS, R. M. & FORSYTHE, J. R. 2003. DES grid resolution issues for vortical flows on a delta wing and an F-18C. AIAA Paper, 1103, 2003.

MULD, T. W., EFRAIMSSON, G. & HENNINGSON, D. S. 2012. Flow structures around a high-speed train extracted using Proper Orthogonal Decomposition and Dynamic Mode Decomposition. *Computers & Fluids*, 57, 87-97.

OpenCFD Ltd. *OpenFOAM 2.1.0.* Accessed 12/07/2016. http://openfoam.com

OpenFOAM, 2014; *Online: http://openfoam.com (last visited 05/01/2017)*

Orszag, S.A., 1970. Analytical theories of turbulence. *Journal of Fluid Mechanics*, *41*(02), pp.363-386.

P, S. & S, A. 1992. A one-equation turbulence model for aerodynamic flows. 30th Aerospace Sciences Meeting and Exhibit. American Institute of Aeronautics and Astronautics.

PATANKAR, S. V. & SPALDING, D. B. 1972. A calculation procedure for heat, mass and momentum transfer in three-dimensional parabolic flows. *International Journal of Heat and Mass Transfer*, 15, 1787-1806.

QUINN, A. & HAYWARD, M. 2008. Full-scale aerodynamic measurements underneath a high-speed train. *Proceedings of the BBAA VI*, Milano, Italy.

RenSMART. *NOABL wind map at 10 meters (2010).* Accessed 21/04/2016. http://www.rensmart.com/Weather/BERR

RSSB. 2007. Effective management of risk from slipstream at trackside and on platforms (T425 report)

RWDI-INC. 2012. Structual Wind Tunnel Assessments - High-speed Train. In: KILPATRICK, J. (ed.). RWDI, Bedfordshire.

SANZ-ANDRÉS, A. & SANTIAGO-PROWALD, J. 2002. Train-induced pressure on pedestrians. *Journal of Wind Engineering and Industrial Aerodynamics*, 90, 1007-1015.

SCHATZMANN, M. & LEITL, B. Validation of urban flow and dispersion cfd models. The Fifth International Symposium on Computational Wind Engineering (CWE2010) Chapel Hill, North Carolina, USA, 2010.

SCHOBER, M., WEISE, M., ORELLANO, A., DEEG, P. & WETZEL, W. 2010. Wind tunnel investigation of an ICE 3 endcar on three standard ground scenarios. *Journal of Wind Engineering and Industrial Aerodynamics*, 98, 345-352.

SCHULTE-WERNING, B., HEINE, C. & MATSCHKE, G. 2003. Unsteady Wake Flow Characteristics of High-Speed Trains. PAMM, 2, 332-333.

SHIH, T.-H., LIOU, W. W., SHABBIR, A., YANG, Z. & ZHU, J. 1995. A new k-ϵ eddy viscosity model for high reynolds number turbulent flows. *Computers & Fluids*, 24, 227-238.

SMAGORINSKY, J. 1963. General circulation experiments with the primitive equations: I. the basic experiment*. Monthly weather review, 91, 99-164.

SOPER, DAVID. 2014. The aerodynamics of a container freight train. Ph.D. thesis, University of Birmingham.

SOPER, D., GALLAGHER, M., BAKER, C. & QUINN, A. 2016. A model-scale study to assess the influence of ground geometries on aerodynamic flow development around a train. *Proceedings of the Institution of Mechanical Engineers, Part F: Journal of Rail and Rapid Transit*, 0954409716648719.

SPALART, P., JOU, W., STRELETS, M. & ALLMARAS, S. 1997. Comments on the feasibility of LES for wings, and on a hybrid RANS/LES approach. Advances in DNS/LES, 1, 4-8.

SPALART, P. R., DECK, S., SHUR, M., SQUIRES, K., STRELETS, M. K. & TRAVIN, A. 2006. A new version of detached-eddy simulation, resistant to ambiguous grid densities. *Theoretical and computational fluid dynamics*, 20, 181-195.

SPALDING, D. B., 1961. A single formula for the "Law of the Wall". *Journal of Applied mechanics*, 28, 3, 455 - 488.

STERLING, M., BAKER, C., JORDAN, S. & JOHNSON, T. 2008. A study of the slipstreams of high-speed passenger trains and freight trains. *Proceedings of the Institution of Mechanical Engineers, Part F: Journal of Rail and Rapid Transit*, 222, 177-193.

SWEBY, P. 1984. High Resolution Schemes Using Flux Limiters for Hyperbolic Conservation Laws. SIAM Journal on Numerical Analysis, 21, 995-1011.

TEMPLE, J. and T. JOHNSON. 2008. Effective management of risk from slipstream effects at trackside and on platforms. Technical report, A report produced for Rail Safety and Standards Board.

TORO, E.F., 2013. *Riemann solvers and numerical methods for fluid dynamics: a practical introduction*. Springer Science & Business Media.

TSI 2008. Relating to the 'Rolling Stock' Sub-System of the Trans-European High-Speed Rail System, 2008/232/CE. *Official Journal of The European Union*.

VDI, 2005, Environmental Meteorology - Prognostic microscale wind field models – Evaluation for flow around buildings and obstacles. VDI 3738, Part 9. Beuth Verlag , Berlin.

WILCOX, D.C. 1998. Re-assessment of the scale-determining equation for advanced turbulence models. AIAA journal, vol. 26, no. 11, pp. 1299-1310

WU, D. 2004. Predictive prospects of unsteady detached-eddy simulations in industrial external aerodynamic flow simulations. Final Thesis. Lehrstuhl für Strömungslehre und Aerodynamisches Institute Aachen. Matriculation number, 219949.

YAKHOT, V. & SMITH, L. M. 1992. The renormalization group, the ε-expansion and derivation of turbulence models. *Journal of scientific computing*, 7, 35-61.